THE GENERATION, SHAPING AND MEASUREMENT OF COHERENT TERAHERTZ RADIATION

A Thesis
Submitted to the Faculty

of

Purdue University

by

Sang-Gyu Park

In Partial Fulfillment of the
Requirements for the Degree

of

Doctor of Philosophy

December 1998

ACKNOWLEDGMENTS

I would like to thank my thesis advisor, Prof. Andrew M. Weiner, for his guidance and encouragement in this research. I discovered this exciting area of ultrafast optics through him and his guidance have made it possible to achieve many things.

I am grateful to Prof. Michael R. Melloch who provided all the semiconductor samples used in this research along with his semiconductor expertise. I also thank Prof. Daniel S. Elliott and Prof. Anant K. Ramdas for their service as my Ph.D. thesis committee members.

I would like to thank Prof. Kwang Seok Seo at Seoul National University who was my master's thesis advisor. I began my research under his guidance, and I learned many valuable lessons in research from him.

I thank Dr. Yongqian Liu with whom I collaborated for the THz pulse-shaping and saturation avoidance using multiple pulse excitation of dipole PC antennas.

High power THz generation experiments using optical amplifier system were performed in collaboration with Dr. Tony Taylor's group at Los Alamos National Laboratory. I thank Dr. Tony Taylor for her giving me a chance to spend a summer in her lab. Also I would like to acknowledge valuable contributions of Dr. Tony Taylor, Dr. Craig Siders and Dr. Jennifer Siders to this work.

I would like to thank current and past members of the ultrafast optics and optical fiber communications laboratory for their making my research life more enjoyable.

I would like to thank my parents. With their unconditional love and support, I have become what I am today.

Most of all, I would like to thank my wife Haejeong for her endurance, understanding and love through the years of my graduate study. And finally I would like to mention my daughter Ina who calls me Daddy.

TABLE OF CONTENTS

Page

LIST OF FIGURES vi

LIST OF TABLES xiii

ABSTRACT xiv

1. INTRODUCTION 1

2. ANALYSIS OF THZ WAVEFORMS MEASURED BY ELECTRO-OPTIC AND PHOTOCONDUCTIVE SAMPLING 5

2.1 Introduction 5
2.2 Theory of FS-EOS and PC-sampling 6
2.2.1 FS-EOS 6
2.2.2 PC-sampling 8
2.3 Characterization of LT-GaAs photoconductors 14
2.4 Results 23
2.4.1 Comparison of FS-EOS and PC-sampled waveforms 23
2.4.2 Effect of carrier lifetime on PC-sampled waveforms 31
2.4.3 The effect of hyper-hemispherical lens on the PC-sampled waveform 32
2.4.4 Comparison of FS-EOS and PC-sampled waveforms with optical doublet excitation 34
2.4.5 Near-field effect in the wide-band THz measurement 34
2.5 Conclusion 45

3. THZ PULSE-SHAPING USING A FEMTOSECOND OPTICAL PULSE-SHAPER 48

3.1 Introduction 48
3.2 Femtosecond optical pulse-shaping 50
3.2.1 Liquid crystal modulator 52
3.3 The theory of THz pulse-shaping 57
3.4 Experimental setup 60
3.5 Results 62

Page

3.5.1 Terahertz internal phase modulation 62
3.5.2 THz amplitude modulation 64
3.5.3 Tunable narrow-band THz radiation 67
3.6 THz pulse-shaping using difference frequency mixing 71
3.6.1 Motivation 71
3.6.2 Theory of THz pulse-shaping employing emitter using difference frequency generation 74
3.6.3 Preliminary results 76
3.7 Conclusion 81

4. SATURATION AVOIDANCE AND THE HIGH-POWER NARROW-BAND THZ GENERATION USING MULTIPLE-PULSE OPTICAL EXCITATION OF PHOTOCONDUCTIVE ANTENNAS 82

4.1 Introduction 82
4.2 The theory of the saturation of PC-antennas 84
4.2.1 The saturation theory 84
4.2.2 Power and amplitude scaling relations of the THz radiation excited multiple-pulse sequence 87
4.3 The avoidance of saturation of small dipole antenna using multiple pulse sequence excitation 89
4.4 Design of the large-aperture PC-antenna for high power narrow-band THz generation 95
4.4.1 Some design considerations in developing the large-aperture antenna for use with multiple-pulse excitation 95
4.4.2 Simulation of THz radiation from large-aperture PC-antenna subject to saturation 95
4.5 Experimental results of high-power narrow-band THz generation using large-aperture PC-antenna 98
4.5.1 Experimental Setup 98
4.5.2 Single Pulse Excitation 101
4.5.3 Two-pulse experiment 105
4.5.4 Narrow-band THz generation using multiple-pulse excitation . 109
4.6 Conclusion 118

5. CONCLUSION 120

5.1 Summary 120
5.2 Future works 121

LIST OF REFERENCES 122

Page

APPENDIX 132

VITA 134

LIST OF FIGURES

Figure Page

2.1 Setup for free space electro-optic sampling of THz in back-to-back configuration, (BS: beam splitter, PD: photo-diode, PBS: polarization beam splitter, $\lambda/4$: quarter wave plate) 7

2.2 Setup for photoconductive sampling of THz in back-to-back configuration 9

2.3 An equivalent circuit diagram of a PC-antenna receiver. Z_0:transmission line impedance Z_A: antenna impedance, V_{oc}: induced open circuit voltage 11

2.4 Experimental setup for pump and probe measurements in reflection geometry. L1, L2, L3: lenses, BB: beam block 16

2.5 Differential reflection of LT-GaAs layers measured by optical pump and probe experiments. Pump and probe wavelength is 855 nm. The LT-GaAs samples were annealed at (a) 575°C (b) 600°C (c) 625°C. The dashed lines are exponential fit to the measured data using lifetimes of (a) 0.4 ps (b) 0.7 ps (c) 1.0 ps 17

2.6 Differential reflection of LT-GaAs layers measured by optical pump and probe experiments. Pump and probe wavelength is 810 nm. The LT-GaAs samples were annealed at (a) 575°C (b) 600°C (c) 625°C. The dashed lines are exponential fit to the measured data using lifetimes of (a) 0.4 ps (b) 1.1 ps (c) 1.6 ps. 18

2.7 The experimental setup for double sliding contact electrical lifetime measurement. The delay between the excitation beam and the sampling beam is delayed by computer controlled translation stage. The exciting and the sampling beam were chopped at different frequencies and the current was measured by a lock-in amplifier at the sum frequency. 20

Figure Page

2.8 Results of electrical carrier lifetime measurements using sliding contacts. (a) excitation wavelength is 810 nm. Two beam spot separation are I (solid line):1 mm, II (dashed line):2 mm (b) excitation wavelength is 850 nm. Two beam spot separation are I (solid line):1.3 mm, II (dashed line):1.9 mm. In (a) and (b), III (dotted lines) represent the fit to corresponding I's using carrier lifetime of $\tau_r = 1.2$ ps. 22

2.9 Measured and calculated THz waveforms: (a),(b),(c): FS-EOS measured waveforms; (d),(e),(f): PC-sampled waveforms (measurement: solid line, calculation: dotted line) The PC-receiver was a short dipole fabricated on LT-GaAs annealed at 575°C. No substrate lens was used in the PC-sampling. 25

2.10 THz waveforms from ZnTe emitter of thickness 150 μm [(a)] and 1 mm [(b) and (c)] measured by another ZnTe sensor of thickness 150 μm [(a) and (b)] and 1 mm [(c)]. 26

2.11 Normalized THz waveforms from the biased S.I. GaAs emitter measured by 150 μm (solid line) or 1 mm (dashed line) thickness E-O sensor crystal 27

2.12 Power spectra of THz waveforms from LT-GaAs emitter measured by FS-EOS (solid line) and PC-sampling (dashed line). The PC-sampling was performed without Si lens. 29

2.13 Measured and simulated THz waveforms by PC-detectors fabricated on the materials of different carrier lifetime. (a) measurement (b) simulation using input THz waveform shown in inset. 30

2.14 THz waveforms from PC-sampling with silicon lens [(a),(b), and (c)]. (d)$\sim$(i) are repetition of Fig. 2.9 for the ease of comparison. The reflection feature from the FS-EOS measured waveform was numerically eliminated before used in the calculation. (measurement: solid line, calculation: dotted line) 33

2.15 Optical cross correlations of the optical doublets generated by femtosecond optical pulse-shaper 35

2.16 FS-EOS and PC-sampled THz waveforms excited by optical doublet. The emitter was a LT-GaAs large-aperture biased photoconductor and the PC-antenna was used with a hyper-hemispherical silicon lens. (a),(b),(c): EO-sampled waveforms; (d),(e),(f): PC-sampled waveforms (measurement: solid-line calculation: dotted line) 36

Figure Page

2.17 THz waveforms measured at several distances from emitter. Detector: PC-detector without silicon lens. (a) SI-GaAs large-aperture photoconductive emitter (b) LT-GaAs large-aperture photoconductive emitter . . 38

2.18 THz waveforms measured at several distances from emitter. Detector: PC-detector with a silicon lens. Emitter: large-aperture emitter on LT-GaAs annealed at 575°C. 39

2.19 Diagram showing the symbols used in the calculation of electric field E at $\mathbf{r}$ from the current distribution in the xy-plane around the origin. A is the diameter of the emitter. This figure represents the case where the polar angle of the measurement point $\phi = 0$. 40

2.20 Peak THz signal measured by PC-antenna with Si lens versus the emitter-detector separation. (dashed line : fit to $1/r$ dependence) 43

2.21 THz waveforms measured by PC-sampling with large separations between the emitter and detector. The biased emitters have 3 mm aperture while the emitters used for Fig. 2.18 and 2.17 have 1 mm aperture. A silicon lens was used with the PC-dipole detector. (a) Biased S.I. GaAs emitter (b) Biased LT-GaAs emitter (c) ZnTe emitter. The LT-GaAs epitaxial layer used here is 1 μm thickness. 44

2.22 THz waveform measured by EO-sampling with emitter-detector separations between 10~28 cm with the same emitters used for Fig. 2.21. Detector :ZnTe crystal of 1 mm thickness. (a) Biased S.I. GaAs emitter (b) Biased LT-GaAs emitter (c) ZnTe emitter. The LT-GaAs epitaxial layer used here is 1 μm thickness. 46

3.1 Grating-Lens programmable pulse-shaper 51

3.2 Liquid crystal spatial modulator array 53

3.3 Schematic of programmable pulse-shaping mask. The mask consists of two LCM with LCM aligned at ±45° from the x-axis and modulator pair is sandwiched by two polarizers aligned along the x-axis. 53

3.4 Phase versus applied bias of a single LCM array 55

3.5 Three pulse sequences with varying separations between pulses. 56

Figure Page

3.6 The schematic of the setup for THz pulse-shaping employing femtosecond optical pulse-shaper and PC-antennas. 61

3.7 Typical characteristic THz system response with single-pulse optical excitation. The inset shows the optical cross-correlation of unshaped pump pulses with pulses directly from the laser as the reference. 63

3.8 Optical cross-correlation of six-pulse sequences and the corresponding THz radiations demonstrating the phase modulation of THz radiation (a) measured optical cross-correlation of two designed six-pulse sequences: (I) equally time-spaced (II) an extra time delay at the fourth pulse. (b) measured THz radiation from the two pulse sequences. (c) calculated THz radiation using the measured characteristic THz system response and cross-correlation data 65

3.9 Terahertz time-domain multiplexing of two 4-bit words. (a) measured optical cross-correlation of input pulses. (b) measured THz radiation as a result of the two encoded sequences. (c) calculated THz radiation of the two 4-bit words based on THz system response using measured characteristic THz system response and cross-correlation data. 66

3.10 Fourier transform of measured intensity cross correlation of single and multiple optical pulses 69

3.11 Measured (solid lines) and calculated (dashed lines) THz radiation with fixed periodic M-sequence phase mask: (a) Δx=0.878 mm, (b) Δx=0.717 mm, (c) Δx=0.625 mm 70

3.12 FFT field spectral amplitude showing the tuning of narrow-band frequencies through changes of the spatial period: (a) Single-pulse, (b) Δx=0.878 mm, (c) Δx=0.717 mm, (d) Δx=0.625 mm. 72

3.13 Tuning range of the narrow-band THz radiation with current apparatus: (a) First-harmonic (b) Second harmonic 73

3.14 The diagram showing the difference frequency generation in <110> ZnTe crystal. E_v,E_h: electric field at fundamental frequency, P_v,P_h: polarization at the difference frequency 75

3.15 THz waveform obtained from ZnTe emitter by varying the crystal orientation while fixing the polarization of the excitation pulse. 77

Figure Page

3.16 Peak amplitude of the THz waveform obtained from a ZnTe emitter by varying the crystal orientation while fixing the polarization of the excitation pulse. 78

3.17 The schematic of the setup for THz pulse-shaping using difference frequency generation. Pump 1 was vertically polarized and pump 2 was horizontally polarized. PBS: polarization beam splitter, $\lambda/2$: half-wave plate 78

3.18 THz radiation generated by difference frequency generation in ZnTe crystal. (a) both vertical and horizontal polarization excitation beams present (b) only vertical polarization excitation beam present (c) only horizontal polarization excitation beam present. 80

4.1 The photoconductive biased emitter. E_b: biased electric field. V_b: applied voltage, J_s: induced current, and $E_{r,1}$, $H_{r,1}$: radiated electric and magnetic field into the semiconductor. $E_{r,2}$, $H_{r,2}$: radiated electric and magnetic field into the free space. 85

4.2 Intensity cross-correlation measurement of the input optical excitation pulse: (a) single pulse, (b) multiple pulses, and time-domain waveforms for the THz radiation using (c) single-optical pulse and (d) multiple-optical-pulse excitation 90

4.3 Fourier transformed power spectrums of the THz radiations from broad-band single pulse excitation and narrow-band multiple pulse excitation at an average power of (a) $P \sim 11\,\mathrm{mW}$, and (b) $P \sim 44\,\mathrm{mW}$ showing the enhancement of radiation by multiple pulse excitation at high powers. . 92

4.4 Spectral amplitude of the THz radiation as a function of the average excitation powers for the (a) single- and (b) multiple-optical pulse excitations. Filled symbols represent peak spectral amplitudes obtained directly from FFT's. Open symbols represent peak amplitudes in the time domain scaled to the spectral amplitudes at fundamental frequency ν_0 by multiplication by the appropriate scale factors. Also shown are typical error bars. 93

4.5 The schematic of the setup for multiple-pulse excitation experimental. . 99

Figure Page

4.6 The hyper-Michelson interferometric pulseshaper used in this experiment. The version shown here and used in the experiments can generate pulse sequences of maximum 8 pulse. TFP: thin-film polarizer, #1~6 are pair of mirrors mounted on the micrometer translational stages. 99

4.7 Cross correlation in a 500 μm KDP crystal of the 8-pulse optical pulse output from the hyper-Michelson interferometer with a single optical gate pulse. 100

4.8 THz radiation waveforms from LT- and SI-GaAs emitters with the excitation by low optical fluence single pulses. The solid-lines represent the measured waveforms and the dashed lines represent the calculated waveforms. Emitter material: (a) LT-GaAs annealed at 575°C (b) LT-GaAs annealed at 600°C (c) LT-GaAs annealed at 625°C (d) SI-GaAs 102

4.9 THz radiation waveforms from (a),(b) a LT-GaAs emitter (annealed at 600°C) and (b),(d) a SI-GaAs emitter. The LT-GaAs was annealed at 600°C. The emitters were excited by (a),(c) low fluence (0.7 μJ) or (b),(d) high fluence (70 μJ) excitation. The solid lines represent the measured waveforms and the dashed lines represent the calculated waveforms. . . . 103

4.10 Results of two-pulse THz emission experiments where the peak amplitude of the second emitted THz pulse is plotted versus inter-pulse separation for (a) a LT-GaAs emitter annealed at 600°C and (b) a SI-GaAs emitter 106

4.11 Optical pump / THz probe experiments on several LT-GaAs samples. (a) 1 μm thick LT-GaAs with substrate (15μJ pump energy) (b) 1 μm thick LT-GaAs with substrate removed (70μJ pump energy) (c) 2.8 μm thick LT-GaAs with substrate with pump energy indicated in the figure. . . . 108

4.12 Simulated results of two-pulse THz emission experiment where the peak amplitude of the second emitted THz pulse is plotted versus inter-pulse separation for a SI-GaAs emitter and LT-GaAs emitter. (a) LT-GaAs layer on SI-GaAs substrate: $\tau_{r,LT}$=0.7 ps, $\tau_{r,SI}$=100 ps.(b) SI-GaAs: τ_r=100 ps. 110

4.13 Measured and Calculated THz radiation waveforms from LT- and SI-GaAs emitters excited by 8-pulse sequences. The LT-GaAs was annealed at 600°C. (a),(b): LT-GaAs emitter. (c),(d): SI-GaAs emitter; (a),(c): excitation fluence of 2 μJ, (b),(d): excitation fluence of 70 μJ. 111

Figure | Page

4.14 Power spectral density of THz radiation excited by a single pulse and 8-pulse sequence. (a),(b): LT-GaAs emitter (annealed at 600°C) (c),(d): SI-GaAs emitter; (a),(c): Low integrated excitation fluence (2 μJ) (b),(d): high integrated excitation fluence (70 μJ). 112

4.15 Power spectral density of THz radiation at the fundamental frequency of 0.3 THz versus optical fluence. (a) SI-GaAs emitter (b) LT-GaAs emitter (600°C annealed) 114

4.16 Calculated power spectral density of THz radiation at the fundamental frequency of 0.3 THz versus optical fluence. (a) SI-GaAs emitter (b) LT-GaAs emitter (0.7 ps carrier lifetime) 115

4.17 Power spectral density of THz radiation at the fundamental frequency of 0.3 THz versus optical fluence. (a) single pulse excitation (b) 8-pulse sequence excitation 117

LIST OF TABLES

Table Page

2.1 Carrier lifetimes of LT-GaAs measured by optical pump and probe measurements and electrical lifetime measurement using sliding contact. . . . 21

ABSTRACT

Park, Sang-Gyu, Ph.D., Purdue University, December 1998. The generation, shaping and measurement of coherent terahertz radiation. Major Professor: Andrew M. Weiner

Coherent terahertz (THz) radiation has been studied extensively recently. It has seen great success in spectroscopy, and more applications are being developed. In this research, we studied various aspects of THz radiation technology which cover the generation, shaping and detection of coherent THz radiation. Firstly, we compared the THz waveforms measured by electro-optic (E-O) and photoconductive (PC) sampling techniques. For the the first time, by quantitative comparison of the waveforms measured by E-O and PC sampling, we found out that the relation between those can be expressed by a simple formalism. And, by using E-O sampled waveforms as references, we could determine the response of the dipole antenna system used in the PC-sampling. This is to our knowledge the first verification of the antenna response function based on the direct measurement of electric field. Also, we demonstrated near-field effects in the THz waveforms and observed the evolution of the THz radiation from the near-field into the far-field regime. Secondly, for the first time, we demonstrated THz pulse shaping using femtosecond optical pulse-shaping. By engineering the temporal profile of the optical pulses exciting PC-emitters using a optical pulse-shaper, we could generate a number of THz waveforms including binary bit streams, and tunable narrow-band radiation. For many applications, high power THz radiation is desired. Usually PC-antennas generate strongest THz radiation below the 2~3 THz region, but they suffer from saturation effects when excited by high fluence optical pulses. We were able to generate high power narrow-band THz radiation avoiding saturation effects by employing multiple pulse excitation on PC-antennas fabricated on fast carrier lifetime LT-GaAs. This was demonstrated using a dipole emitter and then extended to large aperture emitters with amplified excitation pulses. We could obtain more than a factor of 7 improvement in the peak

spectral power density. Also our research clearly demonstrates the near-field nature of the saturation dynamics of large-aperture PC-emitters.

1. INTRODUCTION

Terahertz (THz) radiation is a part of the electromagnetic radiation spectrum. In terms of wavelength, $1\,\text{THz} = 10^{12}\,\text{Hz} = 1000\,\text{GHz}$ corresponds to 0.3 mm in free space. Or the photon energy corresponding to 1 THz is 4.1 meV. In general, the term THz radiation refers to far-infrared or submillimeter radiation. This THz frequency range had been difficult to reach prior to the application of femtosecond lasers for generation of coherent THz radiation. THz frequencies are too high to be directly approached from microwave engineering, but too low to be directly generated by any laser. Only incoherent thermal sources were available, which lack brightness especially below the several THz frequency range. But with the advent of femtosecond lasers, researchers began generating coherent THz radiation and since the 1980s, coherent terahertz (THz) radiation has been of much interest in the ultrafast optics community [1, 2, 3, 4, 5, 6, 7, 8]. Following are some of the important accomplishments in THz generation and detection technology.

The first generation and detection of THz signal was achieved using photoconductive (PC) emitters and detectors. In 1984, Auston *et al* developed a Hertzian dipole system and using this system they could generate and detect propagating THz radiation [1]. Here, they used two identical Hertzian dipoles fabricated on thin radiation damaged silicon as an emitter and a detector. The biased PC-emitter generated subpicosecond duration pulses when illuminated by short optical pulses, and the THz pulse which propagated through the substrate was measured by another PC-detector which was optically gated. In 1988, Smith *et al* extended this technology so that they could detect THz radiation freely propagating through the free space between the antennas which faced each other [2].

In 1989~90, Grischkowsky *et al* developed a THz system which has become a standard technology [9, 8, 10, 11, 6, 12]. In their system, THz radiation from the emitter was collimated by a paraboloidal mirror, traveled for a quite long distance and was collected by another paraboloidal mirror. They also introduced the use of a substrate lens attached to the PC-antenna chip. With this system, they demonstrated

excellent coupling between the source and the detector and high bandwidths reaching 5 THz.

THz radiation was also generated by illuminating a semiconductor surface which does not have any electrodes. After Mourou *et al*'s work in 1981 where they generated electrical pulses of tens of picoseconds of duration [13], Zhang *et al* reported the generation of the THz radiation from semiconductor surfaces [3]. There have been several mechanisms proposed to be responsible for the THz generation from semiconductor surface, which includes current surges in the surface depletion region, and optical rectification. Zhang *et al* also reported the generation of THz radiation through an E-O effect from electro-optic crystals [14, 15]. Until now the fastest coherent THz radiation has been generated using E-O effect. Up to 37 THz oscillation has been measured [16].

Traditionally, the radiation at mid- or far-IR wavelength has been measured using bolometers kept at low temperature. This bolometric detection is a thermal detection method. Therefore, it can only measure integrated energy of the radiation; it cannot time-resolve the waveforms. When the bolometric detection is used to measure the waveforms of coherent radiation, an interferometric approach is used, where the measured waveform is the electric field auto-correlation of the THz radiation. Although bolometric detection has been used quite successfully, it has poor performance at low frequency due to the low sensitivity of available bolometers.

The development of PC-antennas solved much of this problem. It has exceptionally good signal-to-noise ratio below 2∼3 THz region and we do not have to resort to interferometric detection to measure waveforms. (However, we still use the sampling technique where we scan the relative delay between the THz radiation and the probing optical pulse.) By mid-1990's, almost all the detection of coherent THz radiation was performed by PC-antennas. But in a series of papers in 1996, Wu and Zhang demonstrated the measurement of coherent THz radiation using electro-optic (E-O) effect in Zinc-Blend crystals [17, 18, 19, 20, 20, 21]. The major advantage of the E-O sampling is the large bandwidth which comes from the fast E-O effect in the Zinc Blend semiconductor crystal. Due to the simplicity in implementation and high bandwidth, it has become very popular.

Now we examine some applications of this THz technology. The most important accomplishments were achieved in the spectroscopy. Using the THz system described above, Grischkowsky *et al* performed THz time-domain spectroscopy (THz-TDS) on various system [22, 23, 24, 25, 26, 27, 28, 29, 30, 31]. They could identify spectral

lines in water vapor [22, 31], and flames [27] and they studied the carrier dynamics in semiconductors and dielectrics [25, 23, 24, 29, 30]. THz-TDS has been applied by other groups to measure the conductivity and the band-gap of superconducting thin film [32, 33, 34, 35]. Also, optical pump and THz probe experiments have also been performed to study the intraband carrier dynamics in semiconductor [36].

Another potentially important application of THz technology is the imaging developed by Nuss *et al* [37, 38]. By scanning the focal spot position of THz, they could get 2-dimensional images from a number of targets. Usually the images are from the inhomogeneous absorption of THz in the target. For example, since THz frequency range has strong absorption from water molecules, the THz imaging could be used to detect water content variations in biological objects.

Finally, THz impulse ranging was demonstrated by Cheville *et al* [27, 39, 31].

In my Ph.D. thesis research, we studied various aspects of THz radiation technology, such as generation, shaping and detection. Firstly, we analyzed the THz waveforms measured by E-O and PC-sampling techniques. Although the waveforms measured by E-O and PC sampling were quite different, we found out that the relation between those can be expressed by simple formalism. This also helped us to understand the response of the dipole antenna used in the photo-conductive sampling. Secondly, for the first time, we demonstrated the THz pulse shaping via femtosecond optical pulse-shaping. By engineering the temporal intensity profile of the optical pulses exciting photoconductive emitters using a optical pulse-shaper, we could generate a number of THz waveforms including binary bit streams, and tunable narrow-band radiation. For many applications, high power THz radiation is desired. Usually PC-antennas generate the strongest THz radiation, but they suffer from saturation effects when excited by very high fluence optical pulses. In the final part of my research, we could generate the high power narrow-band THz radiation avoiding saturation effects by employing multiple pulse excitation on the PC-antenna fabricated on fast carrier lifetime LT-GaAs photoconductors.

We first demonstrated this saturation avoidance using small dipole PC-emitter with unamplified excitation pulses. Then, we extended this technology by using large aperture emitter with amplified excitation to get real high power THz radiation. We could obtain more than a factor of 7 improvement in the peak spectral power density.

This thesis is organized as follows. In chapter 2, the analysis of THz waveforms measured by E-O and PC-sampling will be presented. In chapter 3, the THz pulse-shaping via optical pulse shaping will be presented. In chapter 4, the generation

of high-power narrow-band THz radiation using multiple pulse excitation will be presented. And finally chapter 5 will conclude this thesis.

2. ANALYSIS OF THZ WAVEFORMS MEASURED BY ELECTRO-OPTIC AND PHOTOCONDUCTIVE SAMPLING

2.1 Introduction

When one deals with THz phenomena, waveform measurement is as important as the generation of the phenomena. For the measurement of THz radiation, photoconductive (PC) sampling and free-space electro-optic sampling (FS-EOS) are two currently widely used techniques. PC-sampling has played an important role in the development of THz technology itself. Because of exceptionally good signal-to-noise ratio and reasonable bandwidth, it has enabled many applications, including spectroscopy [25, 32, 40], imaging [41, 38], and ranging [27].

On the other hand, E-O sampling of freely propagating THz radiation is relatively young. Although the E-O effect itself has been known for a long time, and E-O sampling of guided THz propagation was demonstrated some time ago [42], it was not until recently that E-O sampling of freely propagating THz was demonstrated. Q. Wu and X.-C. Zhang [43, 17, 18, 19, 20, 20, 21], and T. Heinz *et al* [44, 45] developed Free Space Electro-Optic Sampling (FS-EOS) in mid 1990s. Once the FS-EOS technique was developed, it became very popular, mainly due to its simple implementation and large bandwidth.

In this chapter, we analyze and compare the PC and FS-EOS sampling techniques [46, 47]. We will emphasize the relation between the waveforms measured by these techniques. Although these methods are widely used to measure coherent THz radiation, there are not many works comparing these two methods. The comparison has focused mainly on the bandwidth and the signal-to-noise ratio [17, 48]. But detailed comparison of the detected waveforms has been missing. Here, we quantitatively compare the THz waveforms measured by FS-EOS and PC-sampling and showed that the waveforms measured by FS-EOS and PC-sampling could be related by a simple formalism. Also, we present a detailed theoretical analysis which explains the observed PC-antenna response (which in turn can lead to important differences in

the waveforms measured via these two techniques). The effect of the carrier lifetime on the PC-sampled THz waveform is also demonstrated experimentally and compared to theory. Finally, we discuss experiments demonstrating near-field effects and the transition from the near-field to the far-field region for wide-band THz radiation.

2.2 Theory of FS-EOS and PC-sampling

2.2.1 FS-EOS

In FS-EOS, we detect the polarization change of the probe beam induced by the THz electric field through the electro-optic (E-O) effect in the sensor crystal. The typical FS-EOS experimental arrangement used in this research is shown in Fig. 2.1. The THz beam and the optical probe beam co-propagate in the E-O sensor crystal. The optical probe beam path is provided by a thin pellicle beam splitter, which has a negligible effect on the THz beam. The linearly polarized probe beam experiences a polarization change in the sensor crystal due to the birefringence induced by THz electric field. Usually the sensor crystal is a $\langle 1\bar{1}0 \rangle$ oriented Zinc Blend crystal which possesses $\bar{4}3$m symmetry. When the $[1\bar{1}0]$ edge of the crystal is oriented parallel to the polarizations of the incoming THz beam and optical probe beam, the differential phase change Γ of the two probe beam polarization components due to the induced birefringence can be expressed by Eq. 2.1 [49].

$$\Gamma(\omega) = \frac{n^3 r_{41} E_{THz}(\omega)\omega L}{c} , \tag{2.1}$$

where n, r_{41}, and L are the refractive index, electro-optic coefficient, and thickness of the sensor crystal, respectively. $E_{THz}(\omega)$ is the amplitude of THz electric field, ω is the angular frequency of the optical probe beam, and c is the speed of light. The modulated probe beam is analyzed by a setup which consists of a quarter-wave plate, a polarization beam splitter and a pair of balanced photo-diodes. The detected differential current signal can be expressed by Eq. 2.2.

$$\Delta I = I_0 \sin(\Gamma), \tag{2.2}$$

where I_0 is the current which would flow in a diode when all the optical probe power is directed to a single diode. For a moderate modulation depth, the phase change is converted linearly to the differential current. (The typical modulation depth is $10^{-3} \sim 10^{-4}$.)

There are several factors which can affect EO-sampled waveforms. These include group velocity mismatch (GVM) in the sensor crystal, phonon-polariton coupling, and

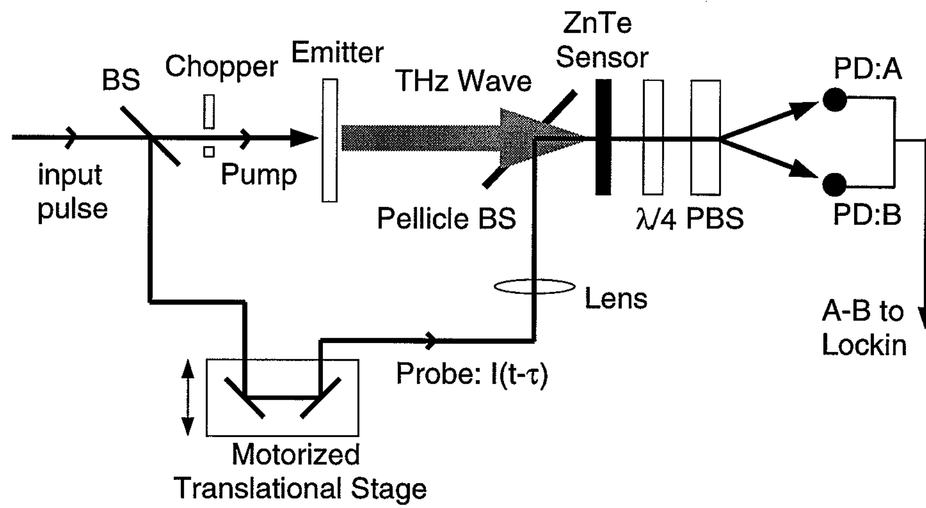

Fig. 2.1. Setup for free space electro-optic sampling of THz in back-to-back configuration, (BS: beam splitter, PD: photo-diode, PBS: polarization beam splitter, $\lambda/4$: quarter wave plate)

finite optical pulsewidth [21]. The GVM arises from the different propagation speeds of the THz and optical waves in the sensor crystal; this leads to the broadening of the measured waveform. The amount of GVM depends on the wavelength of the probe beam and the type of sensor crystal but it can be as large as several picoseconds per millimeter of sensor crystal length [17]. The phonon-polariton coupling describes the phenomenon in which the propagating THz wave leaves behind phonon oscillations, which in turn act as a source of THz radiation. The phonon-polariton coupling usually manifests itself as an oscillatory tail accompanying the main THz features [50]. These two effects — GVM and phonon-polariton coupling — can be minimized by using thin sensor crystals at the expense of reduced signal strength. The finite probe beam pulsewidth is another source of THz waveform broadening, which can be significant for very short THz waveforms. However, in our experiments with 100 fs probe pulses, THz radiation with spectrum under 2~3 THz, and a thin (150 μm) ZnTe E-O sensor crystal, distortion of the terahertz waveforms by all these effects is minimal. Therefore, we consider the measured waveforms to be directly proportional to the incoming THz electric field amplitude. In the context of our comparison with PC-sampling, the ability to independently measure the incoming THz field via FS-EOS isolates the role of the antenna frequency response in the PC-sampling measurement.

2.2.2 PC-sampling

In PC-sampling the measured quantity is the current which flows in the photoconductor excited by delayed optical gate pulses. A typical PC-sampling setup is shown in Fig. 2.2. Electron-hole pairs are generated when an optical gate pulse illuminates the photoconductor in the gap of a dipole antenna. These carriers are driven by the THz electric field, producing a current, whose magnitude is proportional to the THz field and the carrier concentration, and whose direction is determined by the polarity of the THz field. Since the basic operation principle of a PC-antenna is the same as that of an electronic boxcar, a rapid recovery of the electron-hole population is essential in order to get good time resolution. Usually radiation-damaged silicon-on-sapphire (RD-SOS) [51] or low-temperature-grown GaAs (LT-GaAs) [52, 53, 54] are used as the photoconductor material. The average photocurrent I_{pc} as a function of delay τ of the gating pulse can be expressed by the convolution of Eq. 2.3.

$$I_{pc}(\tau) \equiv \frac{Q(\tau)}{T} = \int dt\, v_g(t)\, g(t-\tau), \qquad (2.3)$$

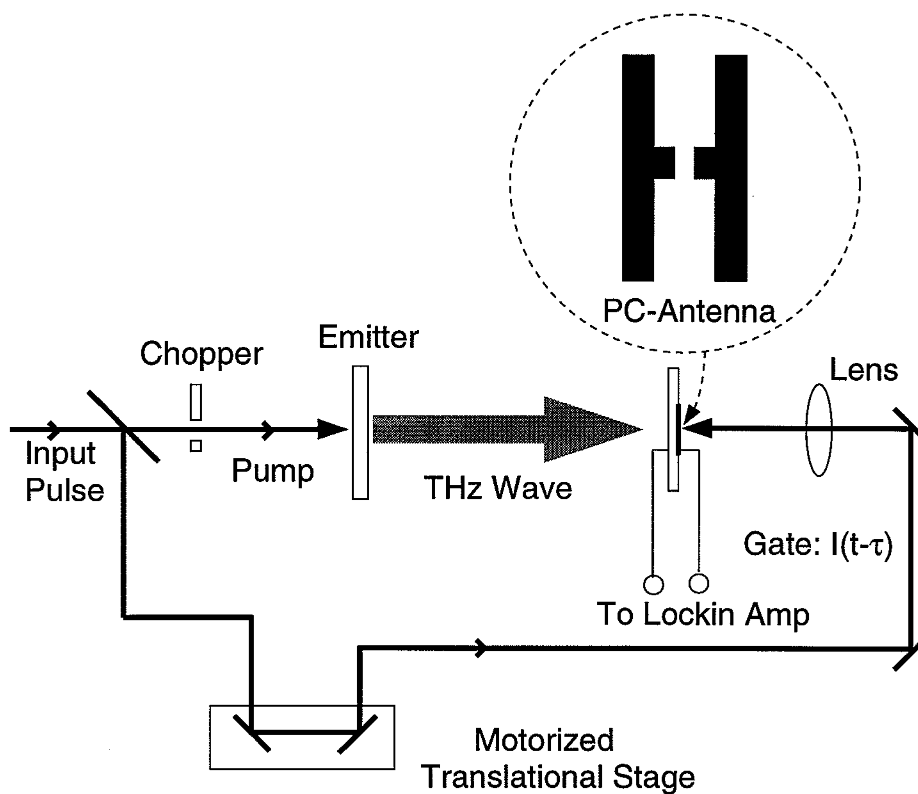

Fig. 2.2. Setup for photoconductive sampling of THz in back-to-back configuration

where $Q(\tau)$ is the collected charge for each gate pulse, $1/T$ is the repetition rate of the laser and the induced bias voltage across the photoconductive gap $v_g(t)$ is

$$v_g(t) \sim \int d\omega\, K(\omega)\, E_{THz}(\omega)\, e^{i\omega t}. \tag{2.4}$$

The time dependent conductance $g(t)$ is given by

$$g(t) = \int^t dt'\, I_g(t')\, (1 - e^{-(t-t')/\tau_C})\, e^{-(t-t')/\tau_R}. \tag{2.5}$$

Here, $I_g(t)$ is the temporal intensity profile of the gating pulse and $E_{THz}(\omega)$ is the Fourier transform of the incoming THz electric field $e_{THz}(t)$. The finite photo-current rise time and the current recovery time are represented by τ_C and τ_R, respectively [55]. The response function $K(\omega)$ represents the frequency dependent ratio of the voltage induced at the sampling gap to the incident THz electric field spectral amplitude $E_{THz}(\omega)$, where $e_{THz}(t)$ and $E_{THz}(\omega)$ are assumed to approximate a plane wave at the receiver. $K(\omega)$ depends on the coupling of the incident wave onto the antenna as well as the impedance matching conditions between the antenna and the transmission line in which it is embedded; both of these factors may be frequency dependent.

The frequency response can be understood with the simple circuit diagram shown in Fig. 2.3 where the receiving antenna is represented by an equivalent open-circuit voltage source $V_{oc}(\omega)$ and a series impedance $Z_A(\omega)$ connected to an external circuit with impedance $Z_0(\omega)$ [56]. From the reciprocity theorem, $Z_A(\omega)$ is identical to the antenna impedance calculated when the same antenna is used as a transmitter [57]. The induced open circuit voltage of the antenna, $V_{oc}(\omega)$, can be calculated from the reciprocity theorem of the antenna as in Eq. 2.6 [58].

$$V_{oc}(\omega) = -\frac{1}{I_m} \int i_T(\omega, s) \boldsymbol{E_{THz}}(\omega, s) \cdot \boldsymbol{ds} \;, \tag{2.6}$$

where $i_T(\omega, s)$ is the current that would flow in the antenna at s if it were used as a transmitter, $\boldsymbol{E_{THz}}(\omega, s)$ is the electric field of the incoming THz wave at s. s is the vector represent the antenna surface and the integral is over the antenna surface. I_m is a normalization factor which represents the maximum of i_T. It should be noted that this $\boldsymbol{E_{THz}}(\omega, s)$ is the field which would exist at s when the receiver is not present. In order words, $\boldsymbol{E_{THz}}(\omega, s)$ represents the incident field without taking into account any perturbations due to the presence of the receiver. When the overall size of the dipole is much less than the beam size of THz radiation, the electric field $\boldsymbol{E_{THz}}(\omega, s)$ can be approximated as $\boldsymbol{E_{THz}}(\omega)$ (for any given ω) because $\boldsymbol{E_{THz}}(\omega, s)$ is

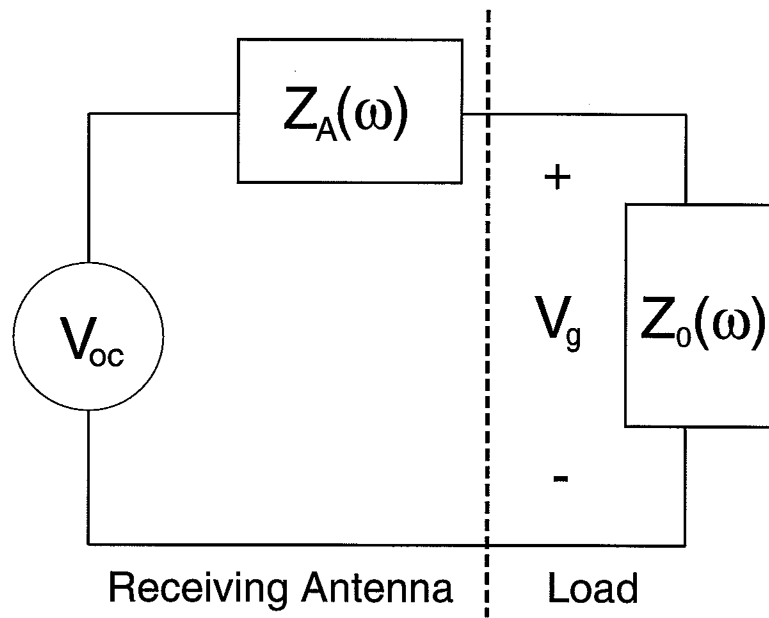

Fig. 2.3. An equivalent circuit diagram of a PC-antenna receiver. Z_0:transmission line impedance Z_A: antenna impedance, V_{oc}: induced open circuit voltage

spatially uniform across the antenna. This will be true when the antenna dimensions are small compared to the THz wavelength of interest, or less restrictively, when the transmitter-receiver pair satisfy the far-field criterion. Specializing now to the dipole antennas studied in our experiments, when the dipole length is much shorter than the wavelength of the THz, $i_T(\omega, s)$ is also frequency independent. For example, i_T has a triangular profile for a short center-fed dipole [57]. In this case, V_{oc} can be approximated by $E_{THz}(\omega)$ multiplied by a frequency independent normalization factor, C, as

$$V_{oc}(\omega) = CE_{THz}(\omega). \tag{2.7}$$

The actual voltage across the gap, V_g, when there is a transmission line feed connected to the antenna, can be calculated from the following voltage divider expression

$$V_g(\omega) = V_{oc}(\omega)\frac{Z_0(\omega)}{Z_0(\omega) + Z_A(\omega)}, \tag{2.8}$$

where $Z_0(\omega)$ and $Z_A(\omega)$ are the impedances of the transmission line (plus load if any) and the antenna, respectively. The radiation impedance of our short dipole is small in the frequency region of interest between tens of GHz and 2 THz [57]. (At very low frequency, the antenna reactance becomes large [59] and this leads to a zero dc response.) On the other hand, when Z_A is small compared to Z_0, V_g can be approximated by V_{oc}. Therefore, if the measurement is limited to the THz range where the wavelength is much longer than the antenna length, both the open circuit voltage and the voltage divider effect are nearly frequency independent. As a result, we have

$$K(\omega) = 1. \tag{2.9}$$

When an antenna is longer, the impedance of antenna and transmission line can be matched at a certain frequency. This kind of resonance characteristic was reported by Smith *et al* [2]. Our formalism is valid under the assumption that the resistance of the gap region upon illumination remains large compared to Z_A. Otherwise, the time dependent gap resistance induced through the sampling action perturbs the voltage divider relation in a way that is not included in Eq. 2.8. Although this assumption may be only partially correct under our experimental conditions, nevertheless, based on our results in Sec. 2.4, which show good agreement between theory and experiment, it appears that our formalism still accounts for impedance matching satisfactorily.

The frequency independent open-circuit voltage relationship of Eq. 2.7 can be derived in an alternative way, also using the reciprocity theorem, as follows. By

definition, $V_{oc}(\omega)$ is independent of the external circuit connected to the antenna. Therefore, when we calculate V_{oc}, we can use any load at our convenience. When the antenna is connected to a load which satisfies the impedance matching condition between the load and the antenna, $Z_A(\omega) = Z_0^*(\omega)$, for a particular frequency ω of interest, the power W_r delivered to the load from the transmitter can be represented by [56]

$$W_r = \frac{\lambda^2 g_{dr} g_{dt}}{(4\pi r)^2} W_t, \tag{2.10}$$

where W_t is the transmitted power, r is the distance between the transmitter and receiver, and g_{dr} and g_{dt} are the directional gains of the receiver and transmitter, respectively. In Eq. 2.10, $W_t(g_{dt}/4\pi r^2)$ can be identified as the incident THz intensity at frequency ω, $I_{inc}(\omega) = |E_{THz}(\omega)|^2/(2\eta)$, at the detector, where η is the impedance of free-space. Then Eq. 2.10 can be rewritten as

$$W_r = \frac{\lambda^2 g_{dr}}{4\pi} \frac{|E_{THz}(\omega)|^2}{2\eta}. \tag{2.11}$$

On the other hand, the average power delivered to the matched load can be expressed in terms of V_{oc} as

$$W_r = \frac{1}{8} \frac{|V_{oc}|^2}{R_r}, \tag{2.12}$$

where R_r = Real (Z_A) is the radiation resistance of the receiving antenna (which is the same as the radiation resistance of the same antenna used as a transmitter). By equating Eq. 2.12 and Eq. 2.11, we obtain

$$|V_{oc}|^2 = \frac{2\lambda^2}{\pi} g_{dr} R_r \frac{|E_{THz}(\omega)|^2}{2\eta}. \tag{2.13}$$

If we know the directional gain $g_{dr}(\omega)$ and radiation resistance $R_r(\omega)$ of the receiver, we can get the response function which relates the open-circuit voltage V_{oc} to the incoming THz electric field E_{THz}. For a short dipole, $g_{dr} = 3/2$ and $R_r = 10\pi^2(l/\lambda)^2$, where l is the length of the dipole [57]. By substituting these expressions into Eq. 2.13, we obtain Eq. 2.14.

$$|V_{oc}(\omega)|^2 = \frac{30\pi l^2}{\eta} |E_{THz}(\omega)|^2 \tag{2.14}$$

We find the open-circuit voltage $V_{oc}(\omega)$ is proportional to the length of the antenna and to the incident electric field spectral amplitude $E_{THz}(\omega)$ with a frequency independent multiplication factor. In the real experiments, the external circuit is not a matched load as in this thought experiment; therefore the actual voltage coupled

across the gap $V_g(\omega)$ still depends on $V_{oc}(\omega)$ through the impedance matching condition of Eq. 2.8.

As reported in the following, our experiments on a short dipole antenna without a substrate lens confirm the flat frequency response shown above [$K(\omega) = 1$]; i.e., $v_g(t)$ is directly proportional to the incoming electric field profile. This is in marked contrast to the well-known $j\omega$ frequency dependence of a short dipole transmitting antenna.

When antennas are used with other coupling elements, the response function of the antenna reflecting those elements should be used. An example of such a coupling element for microwave frequencies is the paraboloidal antenna. In that system, the electromagnetic wave is collected by a large aperture paraboloid and delivered to the active sensing unit which is located at the focal point of the paraboloid. The PC-dipole THz antenna is often used with a hyper-hemispherical substrate lens. In this case the aperture of the entire THz system, consisting of the lens-dipole combination, is not shorter than the THz wavelength and may not be shorter than the THz beam size; the assumptions of the previous paragraphs used to derive the frequency independent response function $K(\omega) = 1$ may not be valid. In fact, we find that a short dipole receiver with a substrate lens does give rise to a frequency dependent response $K(\omega) \sim j\omega$ in the specific optical system and frequency range of our experiments. This will be covered in detail in Sec. 2.4.3.

2.3 Characterization of LT-GaAs photoconductors

In this section, we discuss the characterization of the LT-GaAs photoconductors which we used to fabricate PC dipole detectors and large aperture emitters. The LT-GaAs was grown and subsequently annealed by Prof. Melloch using molecular beam epitaxy (MBE) and rapid thermal annealing (RTA). The characterization studies were performed on samples consisting of $0.5\,mu$m thick normal GaAs buffer layer grown at 600°C and 2.8μm thick LT-GaAs layer grown at 280°C. After the MBE growth, the sample wafer was cut into pieces and annealed at 575, 600, and 625°C, respectively, for 30 seconds. With similar growing conditions, the growth of LT-GaAs with excess arsenic of 0.3~0.9% has been reported [60].

The emphasis of this characterization was the measurement of the recombination/trap lifetime of the photo-generated carriers in the LT-GaAs annealed at different temperatures. The lifetime of the photo-carrier is a very important parameter

of photoconductors, since it governs the resolution of the PC-antenna detection and the THz generation mechanism. The lifetime of photo-carrier in LT-GaAs has been investigated quite extensively [52, 61, 60, 62, 63, 64, 65, 36, 66, 67].

In this research, we performed optical pump and probe differential reflection experiments and the electrical lifetime measurement using sliding contact [7]. Because of the unavailability of the substrate-removed transmission sample, the optical pump and probe measurement was limited to the reflection geometry.

The experimental setup for optical pump and probe measurements are shown in Fig. 2.4. The pump and probe power were ~25 mW and ~2.5 mW, respectively. In the optical pump and probe in reflection geometry, we measure the change of the refractive index due to the photo-generated carriers. We performed optical pump and probe experiments at two wavelengths (855 nm and 810 nm). Theses two wavelengths have importance in that one is very close to the absorption band-edge (855 nm case) and the other is the wavelength at which actual THz generation detection experiments were performed (810 nm case).

Fig. 2.5 shows the result of the optical pump and probe experiments. The pump and probe beam wavelength was 855 nm and the pulsewidth was ~150 fs. The wavelength of 855 nm is just 28 meV above the bandgap of the GaAs. Therefore, we expect recombination/trapping effects, not the carrier cooling [68], dominates the signal. In the Fig. 2.5, we can clearly identify shorter carrier lifetime of the LT-GaAs annealed at lower temperature. The bumps which appear in Fig. 2.5 (b) and (c) seem to be from coherent artifact. When we fit the data with single exponential decay, we get carrier lifetimes of (a) 0.4 ps (575°C) (b) 0.7 ps (600°C) (c) 1.0 ps (625°C). (Lochtefeld *et al* measured 1.5 ps carrier lifetime in the pump and probe differential transmission measurements on LT-GaAs sample which contains 0.52% excess arsenic and annealed at 600°C [65].)

We repeated the pump and probe experiments at 810 nm. The reason was because our THz experiments were performed at 810 nm, the characteristic we measured at 855 nm might be different from the one we observed at 810 nm. Fig. 2.6 shows the result of the optical pump and probe experiments performed at the wavelength of 810 nm. The pulsewidth was ~100 fs. The lifetimes extracted from linear fits are (a) 0.4 ps (575°C) (b) 1.1 ps (600°C) (c) 1.6 ps (625°C). Surprisingly, the lifetimes measured at 810 nm for LT-GaAs annealed at 600°C and 625°C are much longer than the corresponding ones measured at 855 nm. Originally, we expected shorter lifetime from the measurement at 810 nm, on the basis that at 810 nm we would

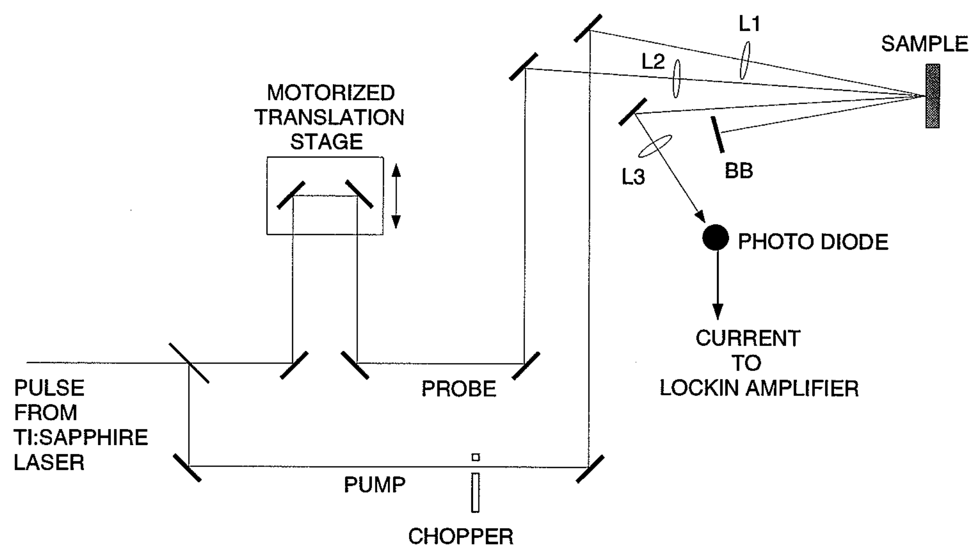

Fig. 2.4. Experimental setup for pump and probe measurements in reflection geometry. L1, L2, L3: lenses, BB: beam block

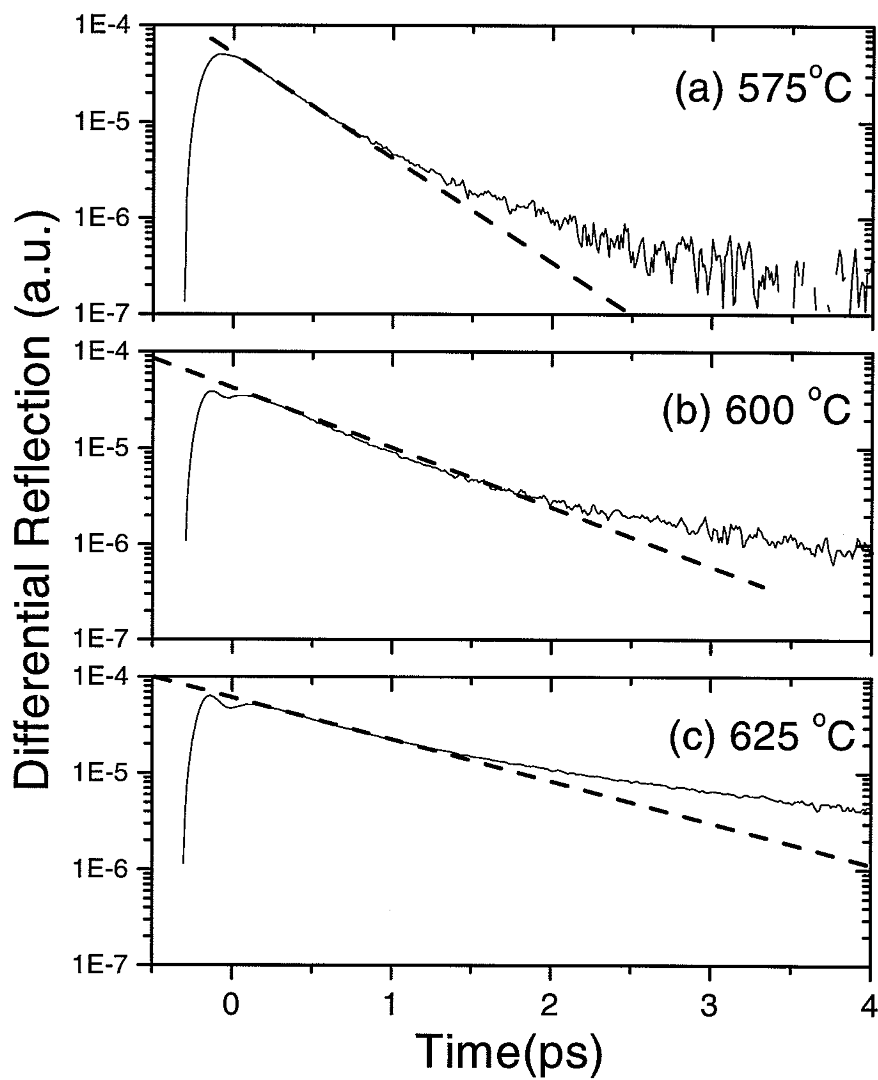

Fig. 2.5. Differential reflection of LT-GaAs layers measured by optical pump and probe experiments. Pump and probe wavelength is 855 nm. The LT-GaAs samples were annealed at (a) 575°C (b) 600°C (c) 625°C. The dashed lines are exponential fit to the measured data using lifetimes of (a) 0.4 ps (b) 0.7 ps (c) 1.0 ps

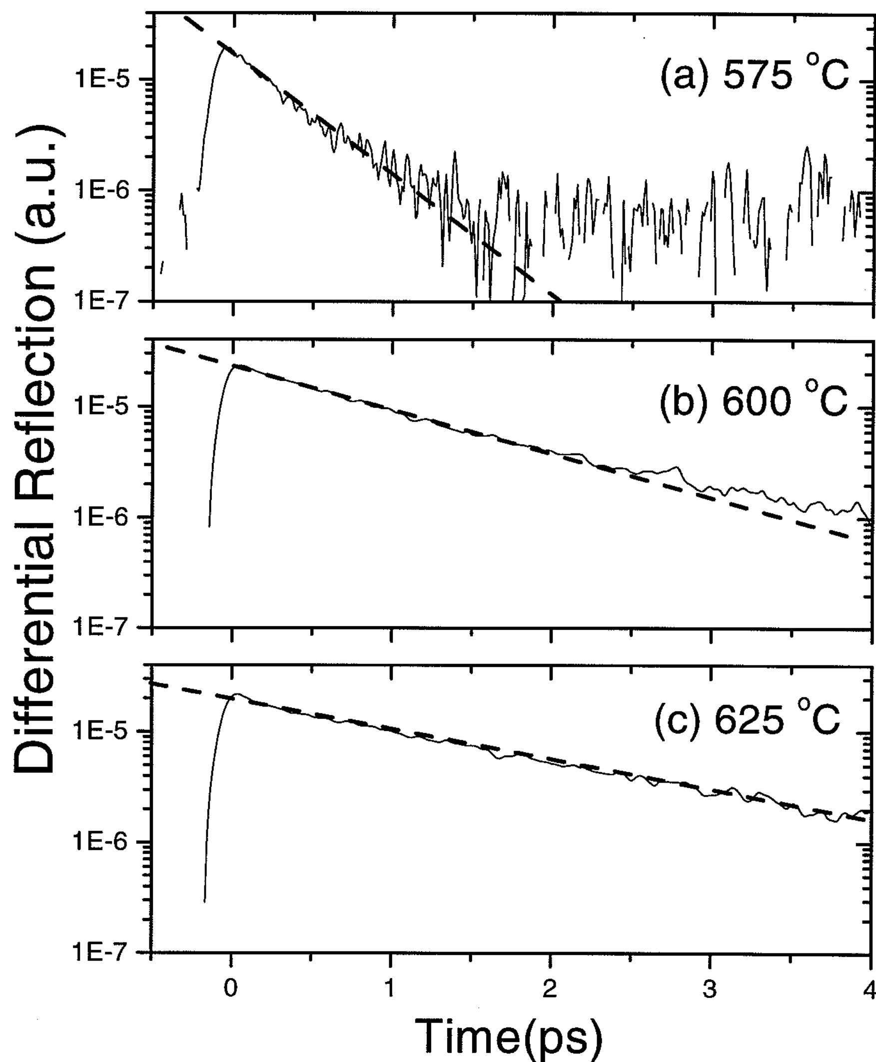

Fig. 2.6. Differential reflection of LT-GaAs layers measured by optical pump and probe experiments. Pump and probe wavelength is 810 nm. The LT-GaAs samples were annealed at (a) 575°C (b) 600°C (c) 625°C. The dashed lines are exponential fit to the measured data using lifetimes of (a) 0.4 ps (b) 1.1 ps (c) 1.6 ps.

observe carrier cooling effect which usually occurs in a much shorter time scale than the carrier recombination and trapping.

After we observed this surprising result, we decided to perform electrical lifetime measurement originally developed by Grischkowsky *et al* [69, 7, 9]. The experimental arrangement is shown in Fig. 2.7. We used the coplanar transmission line which was fabricated as a part of our PC-antenna. The transmission line consists of two parallel 25 μm width Ti/Au lines separated by 50 μm. Because this was fabricated as a PC-antenna, there was a small gap in the middle. However, we expect this does not affect the experiment because all the experiments were performed away from this spot and within the time range the pulse does not propagate to this gap. The delay between the excitation and sampling beam was scanned by computer controlled translation stage. The exciting and the sampling beam were chopped at different frequencies and the current was measured by a lock-in amplifier at the sum frequency. It has been shown that the generation and detection using sliding contact does not suffer from the capacitance [7]. In that case, when we excite the transmission line, a electrical pulse which is directly proportional to the transient conductance is generated [7] and the pulse propagates along the transmission line. When the sampling pulse excites a spot, it generates its own transient conductance. If the electrical pulse generated by the excitation beam arrives when the sampling spot is shorted by the transient conductance from the sampling beam, there is current flowing in the circuit. There is background current even when the electrical pulse and the sampling conductance do not overlap due to the biased nature of the circuit. But we can block these components from being observed by chopping the excitation and sampling beam at different frequencies and lock to the sum frequency. Since the signal is determined by electrical conductivity, we can get carrier lifetime which is directly associated with the current generation mechanism. On the other hand, in the optical pump and probe measurement, the measured quantity is related with the transient refractive index and band filling.

We modeled the transient conductance as the convolution of the sharp rising due to the short excitation pulsewidth and the exponential decay from the carrier recombination or trapping and it is given as

$$g(\tau) = \int dt\, I_{exc}(t)\, e^{-(t-\tau)/\tau_r}, \qquad (2.15)$$

where $I_{exc}(t)$ is the temporal intensity profile of the excitation pulse and τ_r is the carrier lifetime. Since we used same excitation and sampling beam, the transient

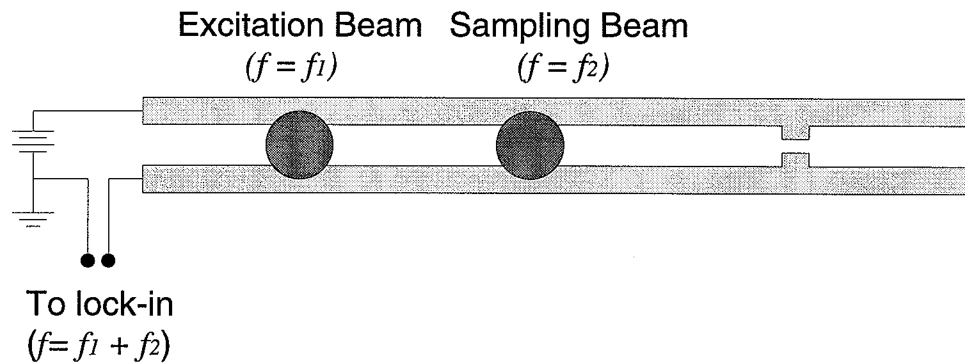

Fig. 2.7. The experimental setup for double sliding contact electrical lifetime measurement. The delay between the excitation beam and the sampling beam is delayed by computer controlled translation stage. The exciting and the sampling beam were chopped at different frequencies and the current was measured by a lock-in amplifier at the sum frequency.

Annealing Temp.(°C)	Pump/probe at 855 nm	Pump/probe at 810 nm	sliding contacts	Melloch Ref. [65]
575	0.4 ps	0.4 ps	—	—
600	0.7 ps	1.1 ps	1.2 ps	1.5 ps
625	1.0 ps	1.6 ps	—	—

Table 2.1 Carrier lifetimes of LT-GaAs measured by optical pump and probe measurements and electrical lifetime measurement using sliding contact.

conductivity from these beams are the same. Then the actually detected signal is given by the auto-correlation of the transient conductivity as given in Eq. 2.16.

$$f(\tau) = \int dt\, g(t)\, g(t-\tau) \tag{2.16}$$

Usually, the temporal pulsewidth of excitation (and sampling) beam is much smaller than the carrier lifetime τ_r. Therefore, the signal $f(\tau)$ is determined predominantly by τ_r.

Fig. 2.8 shows the results of electrical lifetime measurements on LT-GaAs annealed at 600°C. We performed the measurements at 810 nm [Fig. 2.8 (a)] and at 850 nm [Fig. 2.8 (b)]. The solid and the dashed lines represent the measured signal obtained with two distances between the excitation and sampling beam position. The waveforms are individually normalized. We can observe almost the same characteristic from Fig. 2.8 (a) and (b). We fit the measured data with the waveforms calculated based on Eq. 2.15 and 2.16 and the result is shown as dotted lines. We fit the waveform measured with shorter distance between the excitation and the sampling points because the electrical pulse can be broadened during the transmission from the characteristic dispersion of the transmission line. We find that 1.2 ps makes good fits for both waveforms measured at 810 nm and 850 nm.

The electrical carrier lifetime measured by sliding contact excitation looks to be in agreement with the lifetime measured by optical pump and probe at 810 nm not with the one measured by optical pump and probe at 855 nm. But the origin of this behavior is not clear.

In Table 2.1, the result of the optical pump/probe and the electrical measurements are summarized.

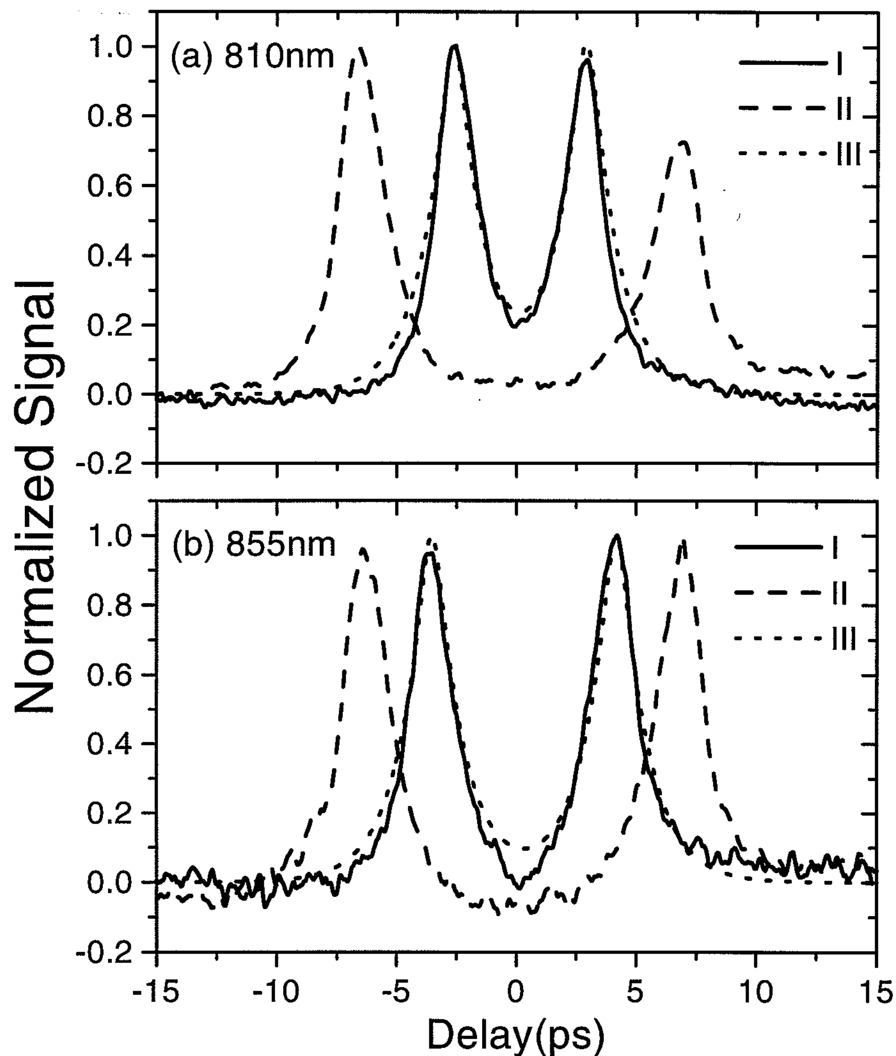

Fig. 2.8. Results of electrical carrier lifetime measurements using sliding contacts. (a) excitation wavelength is 810 nm. Two beam spot separation are I (solid line):1 mm, II (dashed line):2 mm (b) excitation wavelength is 850 nm. Two beam spot separation are I (solid line):1.3 mm, II (dashed line):1.9 mm. In (a) and (b), III (dotted lines) represent the fit to corresponding I's using carrier lifetime of $\tau_r = 1.2\,\text{ps}$.

2.4 Results

2.4.1 Comparison of FS-EOS and PC-sampled waveforms

In this section, we compare the THz waveforms measured by FS-EOS and PC-sampling and show that the waveforms measured by these techniques can be related by simple formulas already given as Eq. 2.3~2.5. Our approach is to use the waveforms measured by FS-EOS as the actual electric field waveform $e_{THz}(t)$ in Eqs. 2.3~2.5 in order to predict the PC-sampled waveforms. Since the PC-sampled waveforms and the FS-EOS waveforms are measured at the same position, we do not need to know the transfer function of the THz pulse from emitter to detector, which would be the same for both waveforms. This is in contrast to the situation where the THz waveforms measured by PC-sampling are modeled based on the calculations of the field at the emitter [70]. Our approach allows for a quantitative investigation of the influence of the antenna response function and the photocurrent lifetime on the photoconductive receiver operation.

We performed FS-EOS and PC-sampling experiments in the setups similar to Figs. 2.1 and 2.2. We did our experiments in the back-to-back configuration, in which emitters and detectors were placed ~12 cm apart facing each other without any collimation optics involved in the beam path. This configuration was used in order to avoid any potential pulse reshaping in the use of THz collection optics such as paraboloidal mirrors. In each case, the receiver (either FS-EOS or PC) was placed at the same position relative to the THz source.

We performed our comparison for three different sources of THz radiation, namely, two different biased large aperture GaAs emitters and an unbiased ZnTe large aperture emitter. These three emitters generated very distinct waveforms, which helped to confirm the validity of our theory. The biased emitters were fabricated by deposition of 3-mm spaced parallel electrodes either on semi-insulating GaAs (SI-GaAs) or LT-GaAs layer grown on SI-GaAs [54]. The LT-GaAs layer was grown at 280°C and subsequently annealed by rapid thermal annealing at 575°C for 30 seconds. We used a very thick (2.8 μm) LT-GaAs layer in order to minimize the partial transmission of the excitation pulse into the SI-GaAs substrate. Typical biases were 200 V and 300 V for SI-GaAs and LT-GaAs emitters, respectively. The unbiased ZnTe emitter was $\langle 1\bar{1}0 \rangle$ oriented and 1 mm thick. In the biased emitters, THz radiation is generated due to current surges, and the far field radiation on the propagating axis is given by the time derivative of the photo-generated current. In the unbiased ZnTe emitters,

optical rectification, which is a second order non-linear process, is responsible for the THz generation [14]. As the FS-EOS receiver, we used a 150 μm thick ZnTe crystal with balanced detection. We used a relatively thin sensor crystal to minimize the waveform distortion by phonon-polariton coupling and GVM, which were described earlier. As the PC-antenna receiver, we used a 50 μm long dipole antenna with a 5 μm gap embedded in a 50 μm spaced coplanar transmission line [6] and fabricated on the LT-GaAs. The LT-GaAs was grown at the same time as the emitter material. Most experiments were performed with the LT-GaAs annealed at 600°C. A mode-locked Ti:Sapphire laser with ~100 fs pulsewidth was used to provide pump and time delayed probe pulses. The delay between pump and probe was scanned using a computer controlled stepper motor stage. The pump power was 800 mW for all cases, and the probe power was 2 mW for FS-EOS and 20 mW for PC-sampling. The pump beam was collimated with a diameter of 1 mm. Of the 12 cm of THz beam path, 10 cm was enclosed in a N_2 purging box in order to reduce the effect of water vapor. Numerical calculations based on the diffraction integral show that with this pump beam size and emitter detector separation, we are measuring the radiated field in the far field region. This was further confirmed experimentally by the observation that when we moved the emitter up to 80 cm away from detector, there was almost no change in the shape of the waveforms. This issue will be covered in more detail in Sec. 2.4.5.

Fig. 2.9 (a), (b) and (c) show the THz waveforms measured by FS-EOS. We can clearly see the difference between the waveforms from different emitters. From the SI-GaAs emitter, we obtained an almost unipolar waveform,which is in sharp contrast to the bipolar waveform obtained from the LT-GaAs emitter. This was expected from the lifetime of photo-generated electrons in these materials. Because of very long carrier lifetime, SI-GaAs has step-like current profile, which gives unipolar waveforms. LT-GaAs has a very short carrier lifetime, therefore, both rising and falling edges of the current profile generate a strong THz field, resulting in bipolar waveforms.

The waveform from the ZnTe emitter has a strong ringing associated with the main oscillation. This ringing seems to be from the emitter, not from the sensor. We performed experiments with ZnTe emitter and sensor of two thickness (1 mm and 150 μm), respectively. The results are shown in Fig. 2.10. When we changed to a 1 mm thick sensor, the ringing remained almost the same, while, when we changed to a 150 μm emitter with the default 150 μm sensor, the ringing almost disappeared.

We also performed the FS-EOS for other emitters with 1 mm thickness sensor. The waveforms are a little bit broadened but quite similar to the ones measured

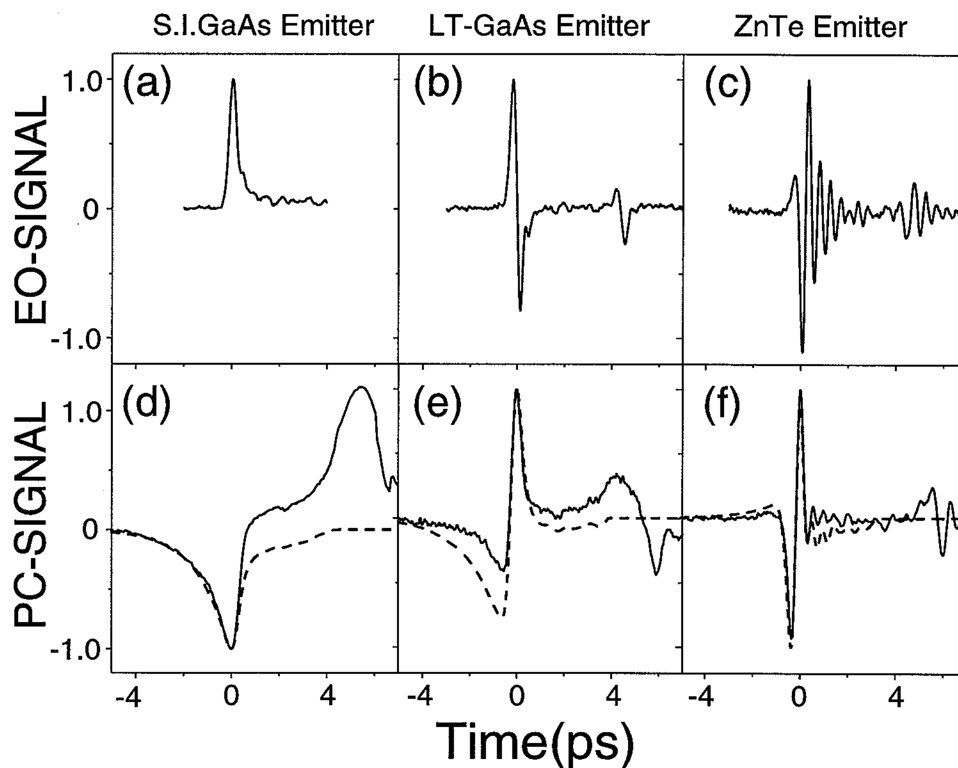

Fig. 2.9. Measured and calculated THz waveforms: (a),(b),(c): FS-EOS measured waveforms; (d),(e),(f): PC-sampled waveforms (measurement: solid line, calculation: dotted line) The PC-receiver was a short dipole fabricated on LT-GaAs annealed at 575°C. No substrate lens was used in the PC-sampling.

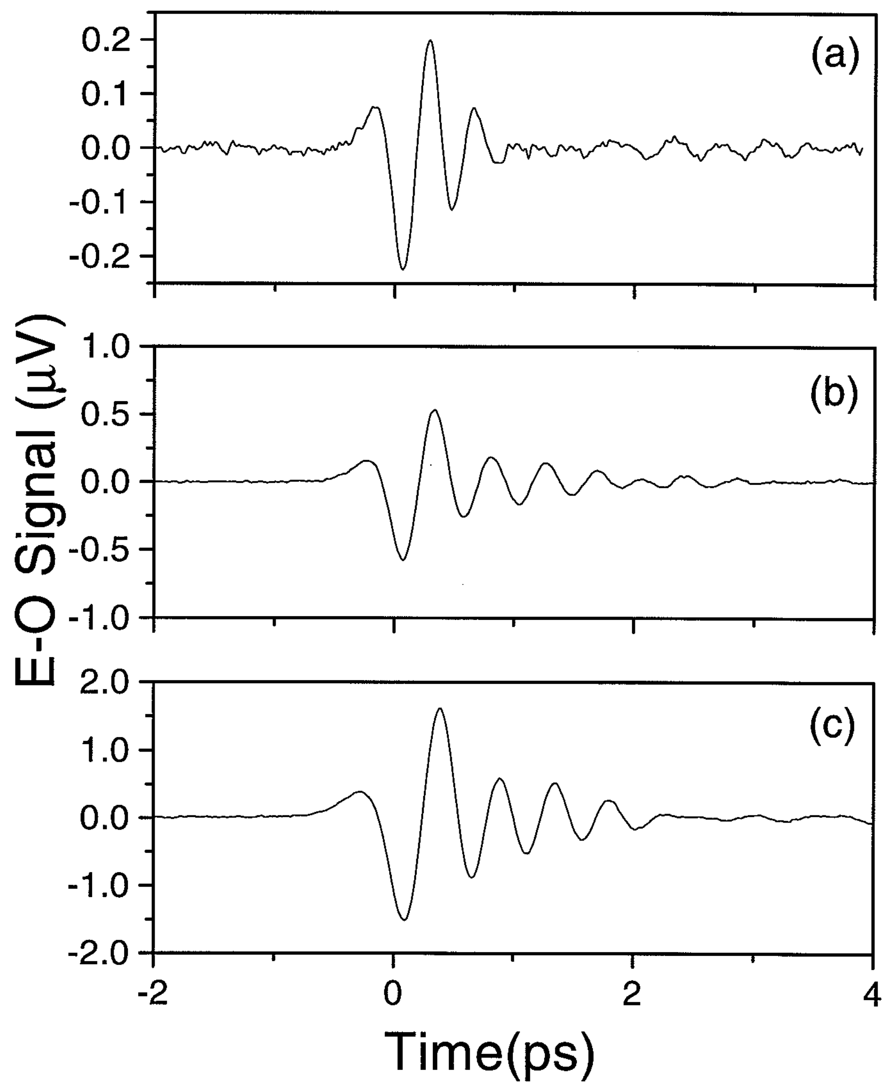

Fig. 2.10. THz waveforms from ZnTe emitter of thickness 150 μm [(a)] and 1 mm [(b) and (c)] measured by another ZnTe sensor of thickness 150 μm [(a) and (b)] and 1 mm [(c)].

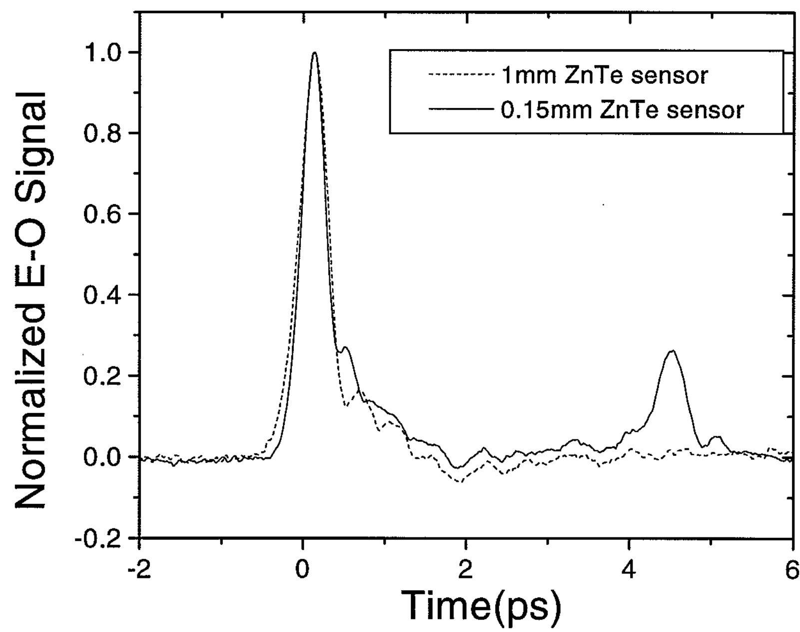

Fig. 2.11. Normalized THz waveforms from the biased S.I. GaAs emitter measured by 150 μm (solid line) or 1 mm (dashed line) thickness E-O sensor crystal

by 150 μm thickness crystal. Fig. 2.11 shows the THz waveforms from the biased SI-GaAs emitter measured by 150 μm or 1 mm thickness ZnTe E-O sensor. These observations also justify our assumption that the FS-EOS measurements with the thin sensor crystal provide a good measure of the actual THz waveform incident on the receiver.

Fig. 2.9 (d), (e), and (f) show the corresponding waveforms measured by PC-sampling (solid lines). Note that no substrate lens was used for these PC-sampling measurements. In each case, the shapes of the PC and the corresponding FS-EOS waveforms are markedly different. Fig. 2.9 (d), (e), and (f) also show the predicted PC-sampling waveforms (dotted lines), which were calculated based on Eqs. 2.3~2.5 using the FS-EOS data as the incident THz field $e_{THz}(t) = \int d\omega\, e^{i\omega t}\, E_{THz}(\omega)$. As fitting parameters we used a carrier lifetime $\tau_R = 1.3$ ps and a momentum relaxation time $\tau_C = 0.18$ ps. The carrier lifetime we used is close to the one measured by pump and probe at 810 nm and sliding contact measurements. We use a flat antenna response function $K(\omega) = 1$, for which the derived and measured waveforms match fairly well. We used the same fitting parameters to calculate waveforms corresponding to each of the three THz emitters. In the data the features 5~6 ps after the main peaks are from reflections which occur at different delays for FS-EOS and PC detectors due to different substrate thickness. (This was not accounted for in the simulation.) The initial dip before the main features of the PC-waveforms is associated with the lifetime of the photo-generated carriers, and is most clearly observed for the unipolar waveform from the SI-GaAs emitter. For the bipolar waveforms (LT-GaAs and ZnTe emitters), this effect is less pronounced, because the positive and negative portions of the waveform partially cancel out in the convolution in Eqs. 2.3~2.5. The agreement between simulated and measured waveforms for all three emitters validates our approach for modeling the PC-receiver response.

Fig. 2.12 shows power spectra of the THz waveforms from the LT-GaAs emitter measured by (a) FS-EOS (solid line) and (b) PC-sampling without Si lens (dashed line). The FS-EOS measurement indicates a spectrum centered around 1 THz and extending to 3 THz, while the spectrum of the PC-sampled waveform centers at 250 GHz and extend to 2 THz. This illustrates the bandwidth limitation arising due to the finite carrier lifetime of the receiver photoconductor.

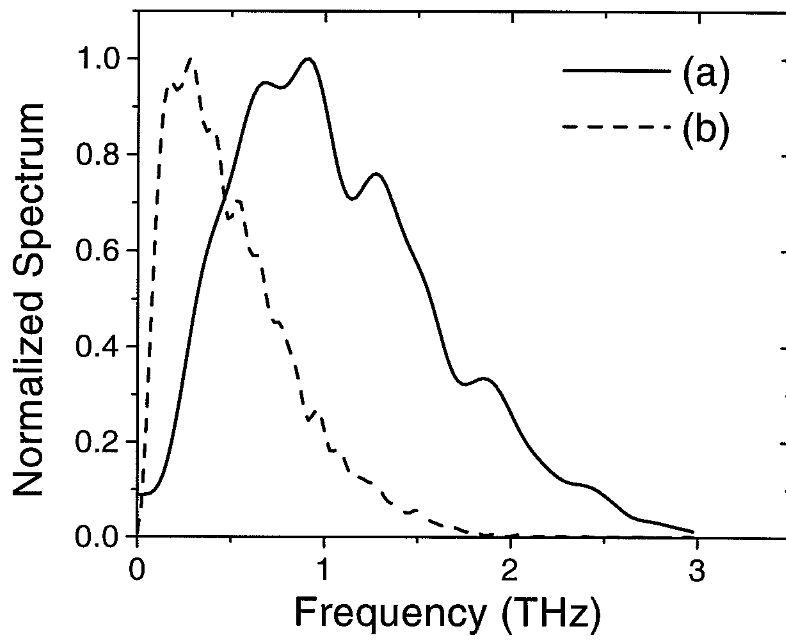

Fig. 2.12. Power spectra of THz waveforms from LT-GaAs emitter measured by FS-EOS (solid line) and PC-sampling (dashed line). The PC-sampling was performed without Si lens.

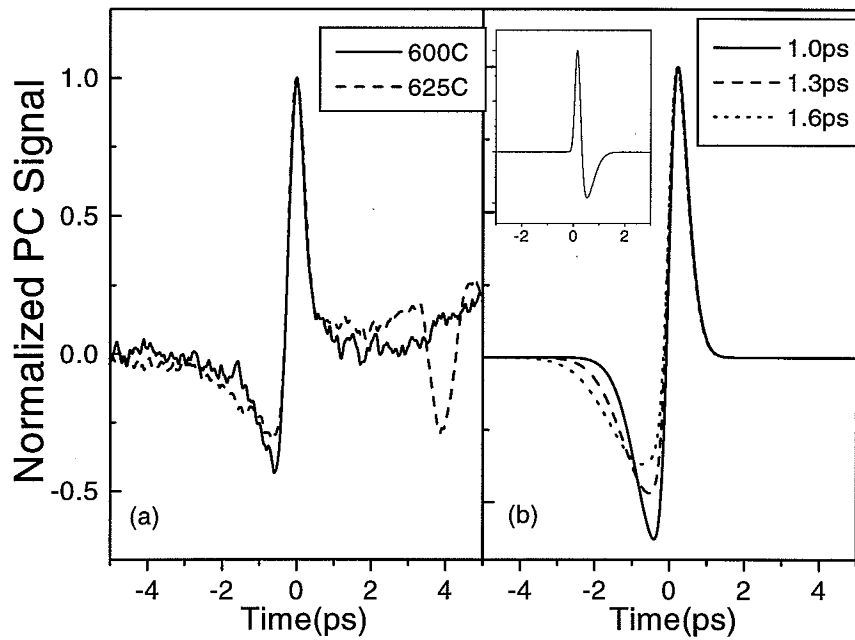

Fig. 2.13. Measured and simulated THz waveforms by PC-detectors fabricated on the materials of different carrier lifetime. (a) measurement (b) simulation using input THz waveform shown in inset.

2.4.2 Effect of carrier lifetime on PC-sampled waveforms

Because of the gated nature of the PC-antenna used in this experiment, the time during which the antenna is open to measure the signal is determined by the convolution of the gate pulse profile and the profile of the photo-generated carriers. Therefore, in order to measure fast transients, it is essential to have very short carrier lifetime and pulsewidth. Usually, the optical pulsewidth is very short compared to the carrier lifetime. Therefore, the carrier lifetime has more effect on the measured THz waveforms. In order to investigate the effect of carrier lifetime on the waveforms, we repeated the PC-detection with two detectors. These detectors were fabricated on LT-GaAs grown at the same time and annealed at 600°C and 625°C, respectively. LT-GaAs has a characteristic that materials annealed at a higher temperature exhibit longer carrier lifetime [60]. According to our optical pump and probe measurement at 800 nm and sliding contact measurement (see Table 2.1 in Sec. 2.3.), the lifetimes are approximately 1.3 ps and 1.6 ps, respectively. The emitter was the same biased LT-GaAs large aperture photoconductor (575°C anneal) as in the previous section. Fig. 2.13 (a) shows the results of the comparison. As expected, the negative dip before the main feature is broadened with the detector annealed at higher temperature. But surprisingly, the main feature itself does not change with anneal temperature. This behavior is compared with the calculation in the Fig. 2.13 (b), in which calculated waveforms from PC-detectors of different carrier lifetime were plotted. We can observe good agreement between Fig. 2.13 (a) and (b). The inset in Fig. 2.13 shows the hypothetical input THz waveform used to calculate the measured waveforms. This comparison demonstrates the character of the distortion of the waveform introduced by long lifetime detector material. This distortion results from the convolution of the time-dependent conductivity and the THz electric field. The conductivity profile is asymmetric in nature because of the fast rise time comparable to the optical pulsewidth and the slower decay time from carrier trapping/recombination. When this conductivity profile is convolved with bipolar waveforms, the first half cycle is greatly reduced while the latter half is less affected, leading to the above observations. In order to preserve the shape of the waveform, the photoconductive decay time should be much shorter than a half period of the THz waveform (which is not the case in our experiments!).

2.4.3 The effect of hyper-hemispherical lens on the PC-sampled waveform

For practical THz systems, the PC-antenna is usually used together with a substrate lens, in order to increase the coupling of the THz energy to the antenna [6]. The effect of such lenses on the waveforms has been discussed by several authors [6, 38, 70]. We have repeated our PC-sampling experiments with a hyper-hemispherical silicon lens attached to the PC-antenna. The PC-antenna receiver was a dipole fabricated on the LT-GaAs annealed at 600°C (the same one as in Sec. 2.4.1). The diameter and the tip to bottom distance of the silicon lens were 10 mm and 6.5 mm, respectively, and the thickness of the GaAs PC receiver chip was 0.63 mm. This design is similar to that used in Ref. [23]

The results of the measurements are shown in Fig. 2.14. We can see distinct differences between the waveforms in Fig. 2.14 and the corresponding PC waveforms in Fig. 2.9. Besides the waveform changes, the amplitude of the THz signal was enhanced by more than a factor of 10 by using the silicon lens. Also shown in Fig. 2.14 are calculated PC waveforms (dotted lines) derived from the FS-EOS data, with the same τ_R and τ_C as used for the modeling results in Fig. 2.9. However, now we use an antenna response function $K(\omega) = j\omega$, which gives excellent agreement with the data waveforms. Agreement was not obtained for flat antenna response $K(\omega) = 1$. The $j\omega$ factor leads to a derivative-like behavior in the time domain.

Our results may be understood as follows. In our back-to-back configuration with 12 cm spacing, the THz beam at the receiver chip is larger than silicon lens aperture for all the frequencies where our PC receiver has significant frequency response. For example, using the diffraction integral, we calculate beam diameters (at the e^{-1} points of the field) of 29 mm and 15 mm for 1 THz and 2 THz, respectively. Therefore, the aperture is defined by the lens diameter and is approximately frequency independent, resulting in a focused THz spot size which is inversely proportional to frequency. This smaller spot size for higher frequency components leads to a higher electric field amplitude for higher frequency, which results in a $j\omega$ frequency factor. In order for this $j\omega$ factor to be observed, the smallest spot size should be larger than the dipole antenna; in our case this condition is easily satisfied. It is interesting to note that the condition that the beam size is larger than the silicon lens is approximately equivalent to the far-field criterion of the emitter/detector system including the silicon lens aperture. It is also important to note that observation of this effect depends on the specific THz optical system and frequency range. Grischkowsky *et al* observed

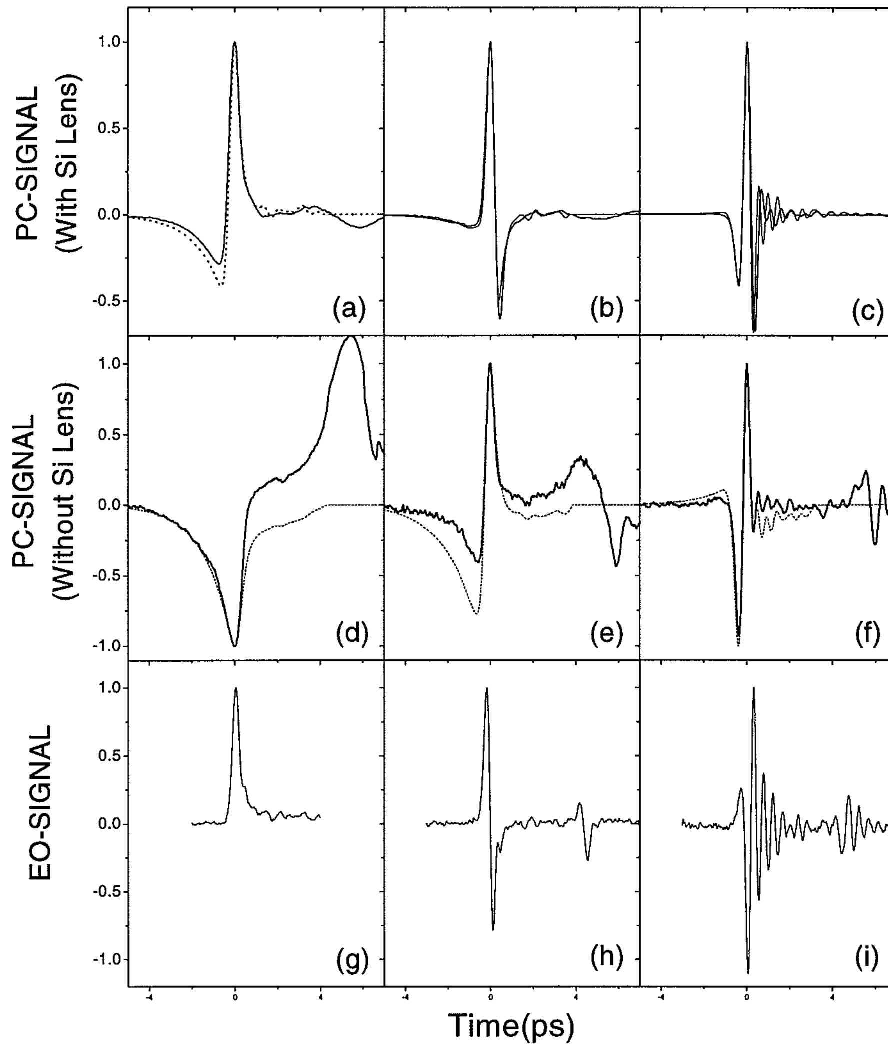

Fig. 2.14. THz waveforms from PC-sampling with silicon lens [(a),(b), and (c)]. (d)~(i) are repetition of Fig. 2.9 for the ease of comparison. The reflection feature from the FS-EOS measured waveform was numerically eliminated before used in the calculation. (measurement: solid line, calculation: dotted line)

a similar time derivative behavior for a different THz optical system employing a pair of paraboloidal relay mirrors [6]. There the THz beam size at the receiver was frequency independent and smaller than the substrate lens aperture; as a result the focused spot was again inversely proportional to frequency, but for a different reason. Silicon lens and optical system designs which do not have a frequency dependent spot size have also been proposed and demonstrated [38].

2.4.4 Comparison of FS-EOS and PC-sampled waveforms with optical doublet excitation

Here, in order to further test our theory, we compare PC and FS-EOS measurements of THz waveforms shaped using femtosecond optical pulse-shaper. Specifically we used doublets generated by a femtosecond optical pulse-shaper [71, 72] to excite a large aperture THz emitter. The pulse-shaper contained a liquid crystal modulator (LCM) array [72, 73] capable of both phase and amplitude modulation [73], which allowed the excitation pulse shapes to be programmed in real time under computer control. The topic of THz pulse-shaping along with the optical pulse-shaping will be covered in Chap. 3. Fig. 2.15 shows three examples of optical cross-correlations of the shaped doublet pulses used in our current experiments.

Fig. 2.16 shows the result of doublet excitation experiments performed with the LT-GaAs emitter annealed at 575°C. The PC-detector was on the LT-GaAs annealed at 600°C, and a Si substrate lens was used. For a doublet spacing of δT=0.5 ps, we have almost a single THz pulse within the resolution of our measurements. From FS-EOS, we could get a small sign of two-pulse excitation; however, the THz generation process at the emitter itself is too slow to make any more significant signature. From PC-sampling no sign of doublet excitation is apparent except for some broadening of the waveform. But as the spacing is increased to 1.0 and 2.0 ps, the THz radiation from each pulse is resolved. When the spacing is 2.0 ps, the two are completely separated from each other in the FS-EOS measurement, whereas in the PC-sampling measurement they are still coupled. In all cases, the match between the measured PC-waveforms and the simulated PC-waveforms using the FS-EOS data for the incident THz wave is very good using the same set of parameters as before.

2.4.5 Near-field effect in the wide-band THz measurement

Lastly, we measured THz waveforms varying the distance between the emitter and detector. We performed PC-detection both with and without the silicon lens as

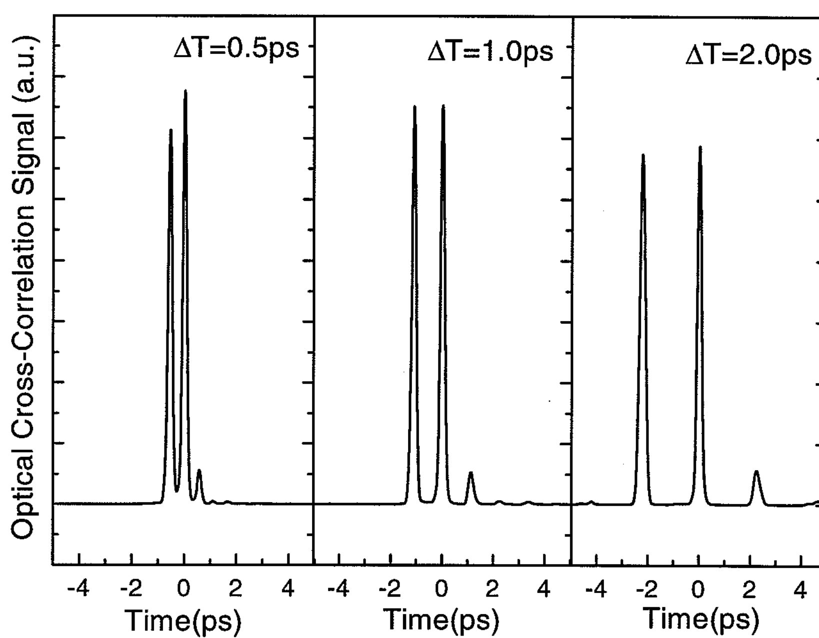

Fig. 2.15. Optical cross correlations of the optical doublets generated by femtosecond optical pulse-shaper

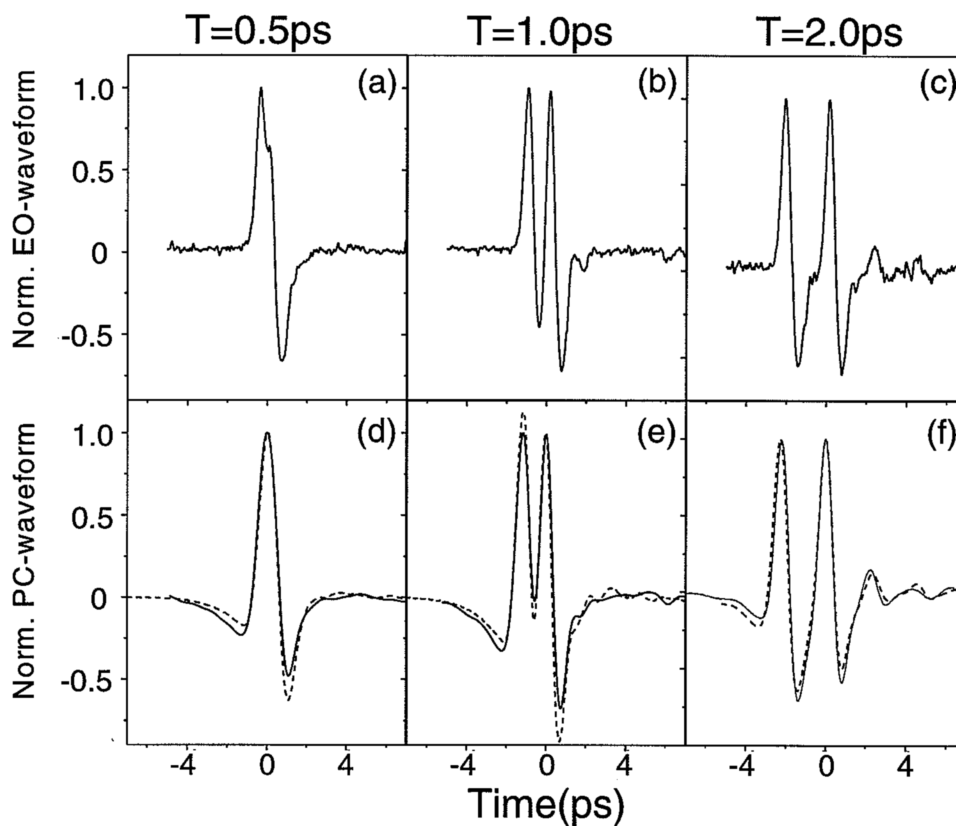

Fig. 2.16. FS-EOS and PC-sampled THz waveforms excited by optical doublet. The emitter was a LT-GaAs large-aperture biased photoconductor and the PC-antenna was used with a hyper-hemispherical silicon lens. (a),(b),(c): EO-sampled waveforms; (d),(e),(f): PC-sampled waveforms (measurement: solid-line calculation: dotted line)

well as FS-EOS, again all in the back-to-back configuration. We used large-aperture photoconductive emitters fabricated from LT-GaAs annealed at 575°C and from SI-GaAs, with an excitation beam diameter of 1 mm. The PC-detector was a dipole fabricated on the LT-GaAs annealed at 600°C. For these experiments we fixed the location of the detector, and changed the separation of the emitter from the detector. Because the optical pump beam and the THz beam are collinear, and assuming the same propagation velocity of THz and optical frequencies in air, we could maintain the same timing condition even while changing the emitter-detector distance. This point is important when comparing the timing between waveforms later. Finally, we did not use the enclosure which was previously used to purge out water in this case because it was difficult both to make enclosure of very large size and to purge the system each time we changed the separation of the emitter and the detector.

Fig. 2.17 shows the THz waveforms from (a) LT-GaAs and (b) SI-GaAs emitters, both measured without a silicon lens. We find that for each emitter, all the waveforms, which were measured at distances varying from 2.6 cm to 11.5 cm, are almost identical. Only the waveforms measured at 2.6 cm separation are perhaps very slightly broadened.

However, in Fig. 2.18, where the THz waveforms from the LT-GaAs emitter were measured by PC-detectors with a silicon lens attached, we see a completely different picture. The waveforms measured at shorter distance are much broader than the waveforms measured at longer distances. Also we found a delay in the arrival time of the THz wave for short emitter-receiver separations. But the waveforms measured for separations greater than 9 cm are almost identical to each other and arrive at the same time.

This behavior can be understood from the antenna theory (or diffraction theory). The electric field $\boldsymbol{E}(\omega, \mathbf{r})$ radiated from a antenna with current distribution $\boldsymbol{J}(\omega, \mathbf{r}')$ can be expressed by [56] (see Fig. 2.19),

$$\boldsymbol{E}(\omega, \mathbf{r}) = -j\omega\mu \int d\mathbf{r}' \frac{e^{ikR}}{4\pi R} \boldsymbol{J}(\omega, \mathbf{r}'), \tag{2.17}$$

where $R = |\mathbf{r} - \mathbf{r}'|$ is the distance from the source point to the measurement point, $k = \omega/c$, and the integration is over the antenna surface. Here, the primed coordinates indicate the source coordinates. This formulation is valid where $R > \lambda$. When $R < \lambda$, the field is more static in nature and cannot be described as a radiating field. But since our measurement is concerned with very high frequency, where the lowest frequency of interest is $\simeq$ 100 GHz, this can be safely ignored for emitter-detector separations

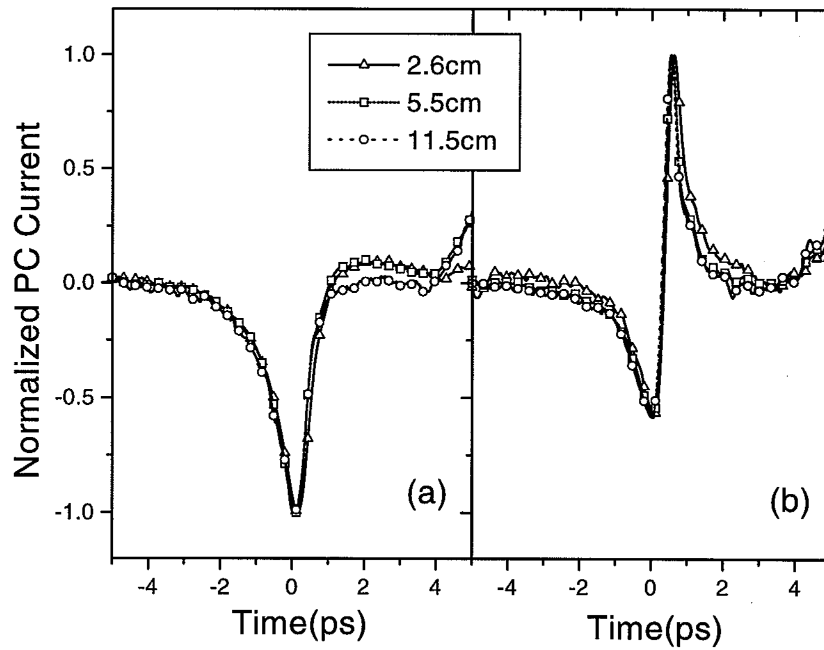

Fig. 2.17. THz waveforms measured at several distances from emitter. Detector: PC-detector without silicon lens. (a) SI-GaAs large-aperture photoconductive emitter (b) LT-GaAs large-aperture photoconductive emitter

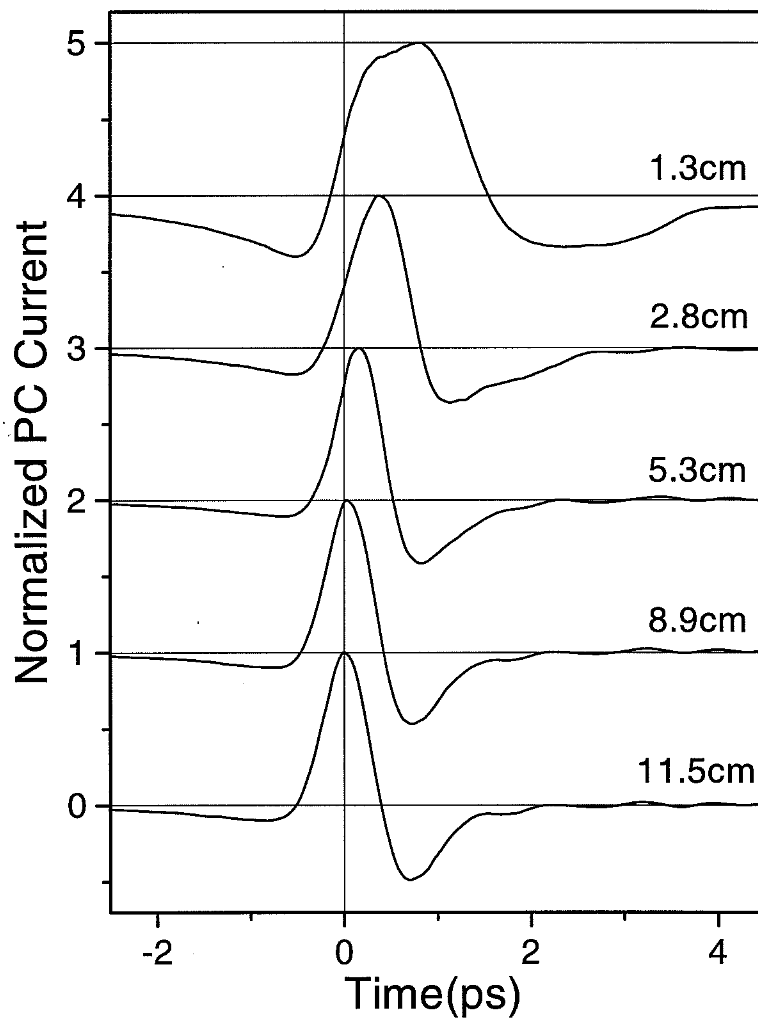

Fig. 2.18. THz waveforms measured at several distances from emitter. Detector: PC-detector with a silicon lens. Emitter: large-aperture emitter on LT-GaAs annealed at 575°C.

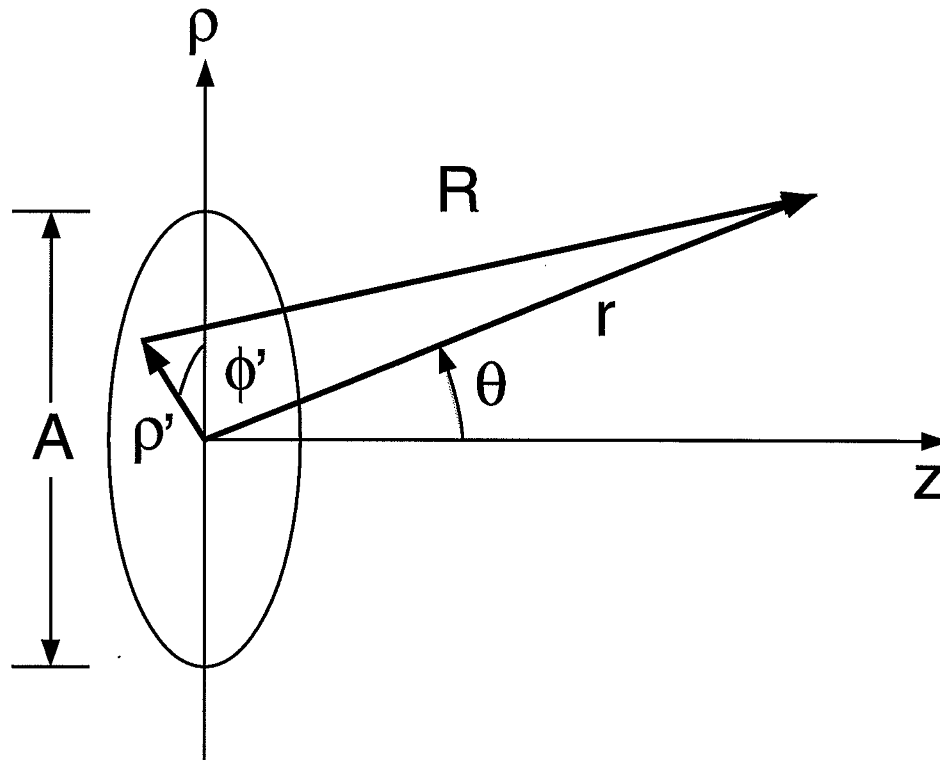

Fig. 2.19. Diagram showing the symbols used in the calculation of electric field E at $\mathbf{r}$ from the current distribution in the xy-plane around the origin. A is the diameter of the emitter. This figure represents the case where the polar angle of the measurement point $\phi = 0$.

over ~1 cm. The distance R is given by

$$R = \sqrt{r^2 - 2\rho' r \sin\theta \cos(\phi' - \phi) + \rho'^2}, \quad (2.18)$$

where $r = \sqrt{x^2 + y^2 + z^2}$ is the distance of the measurement point from the origin (center of the emitter), $\rho' = \sqrt{x'^2 + y'^2}$ is the distance of the source point from the origin, and ϕ and ϕ' are polar angles of $\mathbf{r}$ and $\mathbf{r}'$, respectively. Here we assume that the emitter surface is on the xy-plane ($z = 0$). When r is larger than the antenna radius $A/2$, R can be expressed in series using binomial expansion,

$$R = r - \rho' \sin\theta \cos(\phi - \phi') + \frac{\rho'^2}{2r}(1 - \sin^2\theta \cos^2(\phi - \phi')) + \cdots \quad (2.19)$$

The standard far-field approximation for Eq. 2.17 is that we replace R in the phase term, jkR, with $r - \rho' \sin(\theta)\cos(\phi' - \phi)$ and use $R = r$ in the denominator. In this case, Eq. 2.17 can be simplified as

$$\boldsymbol{E}(\omega, \mathbf{r}) = -j\omega\mu \frac{e^{ikr}}{4\pi r} \int d\mathbf{r}' e^{-ik\rho' \sin\theta \cos(\phi - \phi')} \boldsymbol{J}(\omega, \mathbf{r}'). \quad (2.20)$$

In Eq. 2.20, the source term and propagation term are separated. For this far-field approximation to be valid, the criterion $r > 2(A^2/\lambda)$ should be met which would allow maximum error of $\pi/8$ for the phase term [57]. In this derivation only the size of the emitter was considered. If both emitter and detector have finite size, A_e and A_d, respectively, $A = A_e + A_d$ should be used for the far-field criterion [57]. The above derivation was for the radiation of single frequency ω. When we apply this to wide-band radiation such as the THz of interest here, we should use the maximum frequency with appreciable amplitude. If the the maximum frequency satisfies the far-field criterion, the lower frequency components automatically satisfy the criterion. Now we can calculate the $R_{farfield} = 2(A^2/\lambda)$ for our THz detection system. For the PC-detector without the silicon lens, the size of the dipole antenna detector (50 μm) is negligible compared to the size of emitter aperture (1 mm). In this case the $R_{farfield}$ is 13 mm for 2 THz and 7 mm for 1 THz which are small compared to all the observation distances. This is consistent with the data of Fig. 2.17, which shows the THz waveforms independent of distance over the range > 2.6 cm investigated. But when the silicon lens was used with the PC-detector, the detector aperture size is increased. Fattinger *et al* [11] and Jepsen *et al* [70] have investigated the beam propagation in similar systems. It is difficult to assign an effective aperture size exactly due to partial reflections and the inhomogeneous field distribution. If we use

5 mm (which is half the diameter of the lens) as the combined effective aperture size of system, we get $R_{farfield} = 33$ cm for 2 THz and 16 cm for 1 THz. This agrees roughly with our observation (Fig. 2.18) that the waveform did not change appreciably for propagation over distances ≥ 10 cm. The broadening and additional delay of THz waveforms at shorter observation distances arise because the distances the THz wave components must travel depends on the particular points in the emitter and detector. The delay can be estimated by simple trigonometry. For the center-to-center distance between the emitter and the detector, r, and the combined aperture size, A, the maximum extra time delay, ΔT, is given by $\Delta T = (\sqrt{(r^2 + (A/2)^2)} - r)/c$. For example, if we use $r = 3$ cm and $A = 5$ mm for our PC-detector with silicon lens, we get $\Delta T = 0.35$ps. The THz waveform measured at a distance of 2.8 cm in Fig. 2.18 shows that the peak is displaced by 0.5 ps compared to the far-field data, again in qualitative agreement with our simple estimate.

From Eq. 2.20, we expect that in the far-field region we measure the same waveforms regardless of emitter-detector separations with $1/r$ attenuation of the signal strength. In Fig. 2.20, the peak THz signal measured by PC-antenna with Si lens versus the emitter-detector separation is plotted. When the detector position is very close to emitter, the peak amplitude is small because, the radiation from various point in emitter to various points to detector do not arrive at the same time. But when r is large, we are in the far-field region and the magnitude experiences $1/r$ attenuation. Also shown in dashed line is the fit to expected $1/r$ dependence. We observe relatively good fit although in the long distance the attenuation look a little bit stronger than expected.

We also performed emitter-detector separation dependence PC-detection experiments with emitters of larger aperture which was defined by 3 mm diameter excitation beam size with. The silicon lens was used with PC-dipole antenna. If we calculate the $R_{farfield} = 2(A^2/\lambda)$ with new emitter aperture size, i.e. $A = A_e + A_d = 7mm$, $R_{farfield} = 65$ cm for 2 THz and 33 cm for 1 THz. Fig. 2.21 shows the measured waveforms (individually normalized) from (a) biased S.I.GaAs emitter (b) LT-GaAs emitter (c) ZnTe emitter. For all cases, we can observe that the waveforms measured with 25 cm and 63 cm emitter-detector separations are almost identical, while the ones measured with 10 cm separation show some difference. Furthermore, the waveforms measured 10 cm from the emitter arrived later than the ones measured 25 cm and 63 cm away. This is all in agreement with the previous argument. When the emitter size was 1 mm, the waveforms after 10 cm were already almost identical. But now

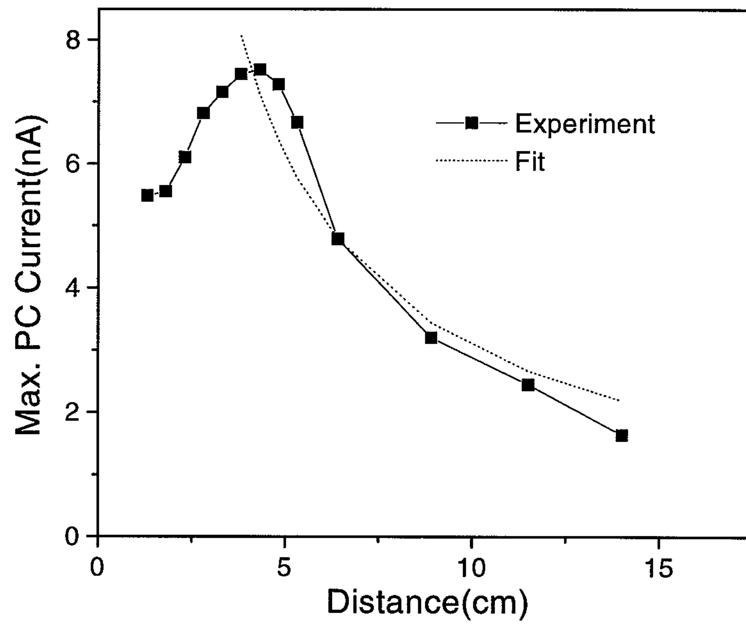

Fig. 2.20. Peak THz signal measured by PC-antenna with Si lens versus the emitter-detector separation. (dashed line : fit to $1/r$ dependence)

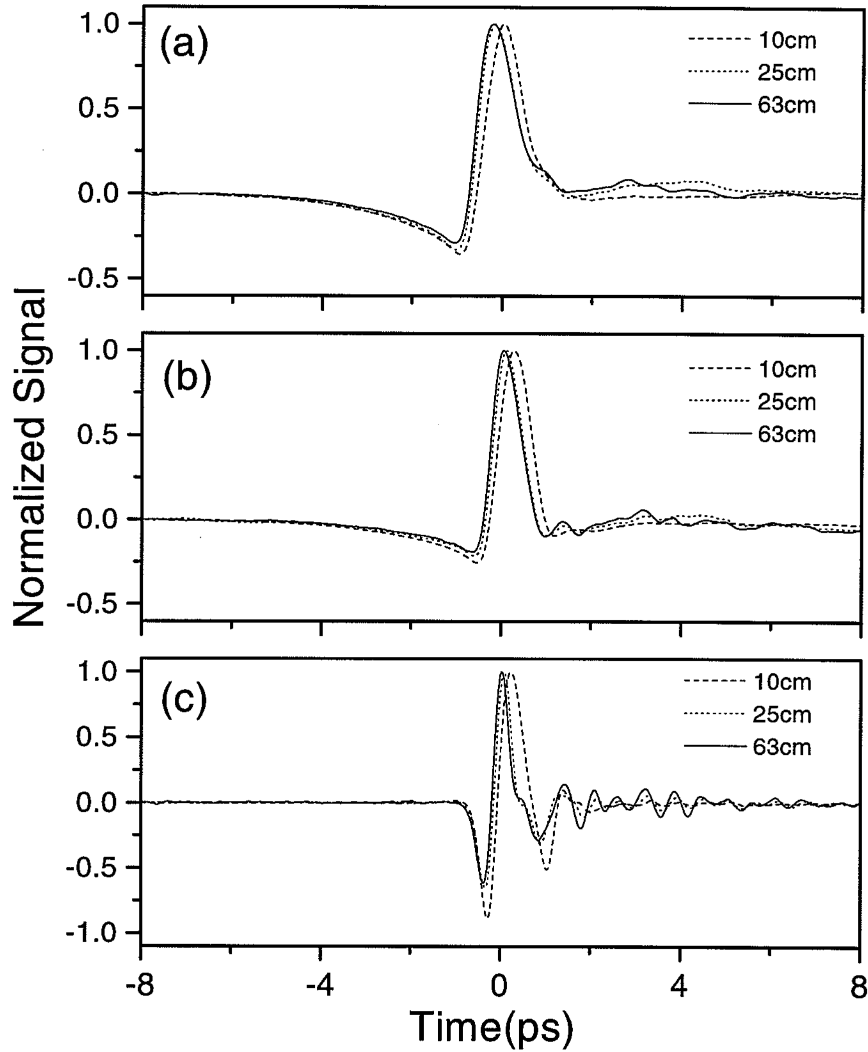

Fig. 2.21. THz waveforms measured by PC-sampling with large separations between the emitter and detector. The biased emitters have 3 mm aperture while the emitters used for Fig. 2.18 and 2.17 have 1 mm aperture. A silicon lens was used with the PC-dipole detector. (a) Biased S.I. GaAs emitter (b) Biased LT-GaAs emitter (c) ZnTe emitter. The LT-GaAs epitaxial layer used here is 1 μm thickness.

with the increased emitter aperture, we observe the near-field effect in the extended area.

We also performed distance dependence experiments with FS-EOS with emitter-receiver separations between 12∼28 cm using 1 mm thickness ZnTe sensor crystal and the results are shown in Fig. 2.22. Because of the presence of the pellicle beam splitter, we could not make the distance shorter. In the range investigated, we did not observe any change of pulse-shape, other than the attenuation at larger distance.

Near-field effects were also observed by Budiarto *et al* [74]. In their experiments, a SI-GaAs photoconductive emitter with a very large aperture (3 cm) was used, and all the experiments were limited to the near-field region.

Our experiments clearly demonstrate the existence of a far-field region even for wide-band THz radiation. When each frequency component satisfies the far-field condition—when the highest frequency component satisfies this, the others do automatically— the spectral amplitude of each frequency component is governed by a $1/r$ scaling rule, so that each frequency is attenuated at the same rate, as seen in Eq. 2.20. Beyond the minimum separation needed to satisfy the far-field criterion, the THz waveform and its frequency dependence become independent of the emitter-detector distance r.

2.5 Conclusion

In conclusion, we have analyzed THz waveforms measured by FS-EOS and PC-sampling and have directly compared the THz radiation waveforms measured from FS-EOS and PC-sampling receivers. Although we observed significant differences between the two types measurements, we demonstrated that the waveforms measured by the PC-antenna can be derived from the FS-EOS waveforms by using a simple theoretical formalism which takes into account the response of the photoconductive antenna and the photo-carrier lifetime. For a PC THz receiver consisting of a short dipole without a substrate lens, we showed both experimentally and theoretically that the receiver antenna response is approximately flat over the THz frequency range of interest. For the same receiver with a substrate lens, we found a $j\omega$ frequency dependence for the receiver's antenna response, which we explained based on the specific optical system in use. Our results help to elucidate the role of the frequency-dependent antenna response in PC-sampling THz receivers. We also investigated the effect of the photoconductive carrier lifetime on the THz waveform measurement and

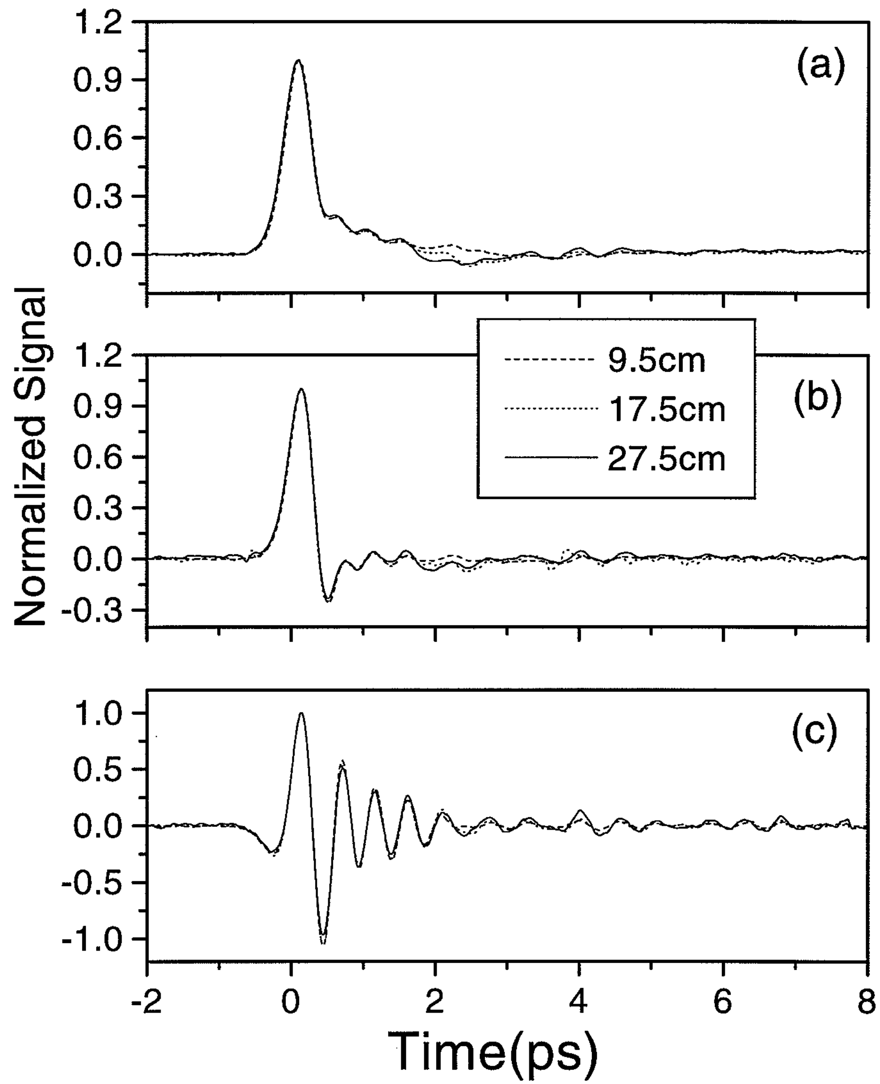

Fig. 2.22. THz waveform measured by EO-sampling with emitter-detector separations between 10~28 cm with the same emitters used for Fig. 2.21. Detector :ZnTe crystal of 1 mm thickness. (a) Biased S.I. GaAs emitter (b) Biased LT-GaAs emitter (c) ZnTe emitter. The LT-GaAs epitaxial layer used here is 1 μm thickness.

explained our results through simulation. Finally, we demonstrated near-field effects in PC-sampling measurements of THz waveforms and explored the evolution of the THz radiation from the near-field into the far-field region.

3. THZ PULSE-SHAPING USING A FEMTOSECOND OPTICAL PULSE-SHAPER

3.1 Introduction

Coherent THz radiation is usually generated by illuminating an emitter (either biased or not) with a single short optical pulse. The illuminated emitter generates THz radiation in a form of short of pulse. This short pulse possesses broad-band spectrum and it represents the capability of producing more complex waveforms. To extend the flexibility of THz radiation for some other applications, such as coherent control of molecular states in the THz-frequency range and submillimeter communications, it is also desirable to have capabilities of generating arbitrarily shaped millimeter and submillimeter waveforms. Similar to applications of optical pulse-shaping for ultrafast optical communications [75] and coherent control [76], the ability to shape THz radiation fields has great potential for coherent control of dynamical processes such as chemical reactions [76, 77] and submillimeter-wave interconnect systems based on THz radiation. There have been some attempts to generate THz waveforms other than simple short pulses. These efforts can be divided into three categories.

The first one is the direct manipulation of the generated THz radiation. This approach is difficult to implement because of the lack of devices which can handle THz radiation. One of the works used a variable size slit as a tunable high-pass filter and could change the THz waveforms in a certain way [78]. But it could not be used to generate THz waveforms in general and the shaping is accompanied by a heavy loss of the THz energy.

The second one is to have array-type antenna which is designed for the desired waveforms. PC-antenna arrays have been made where the bias voltage applied to each pair of electrodes could be specified to generate desired waveforms [79, 4]. With these, they could shape the THz waveforms quite arbitrarily, but again this was obtained with a large loss of signal strength because we detect a particular angular slice of the THz power from the array, which might be radiating more energy to other direction.

The third one is to shape the optical excitation pulse. This approach, which we will follow in this research, is easier to implement and versatile. There have been some works of THz pulse shaping using approaches along this line. Weling *et al* generated narrow-band THz radiation using a pulse train which in turn was generated by an interference of chirped optical pulses [80, 81]. Also the attempts to generate simple THz waveforms through coherent control of charge oscillations in quantum-well structures fall into this category [82, 83, 84]. In the former case, because of the special excitation pulse shaping method, the waveforms which can be generated is limited to the multiple pulse sequences of THz. In the latter case, the available waveform is strictly limited by the intrinsic charge oscillations and the available power is also very much limited.

Recent developments in femtosecond optical pulse-shaping technology, which provides the ability to synthesize ultrashort optical waveforms according to specification [71, 85, 73, 86, 75, 87, 88, 89, 90], have significant implications for the THz pulse-shaping. In this chapter, we describe a technique for THz waveform synthesis using optical shaping of the excitation pulses to the PC-emitter [91]. This technique combines the broad-band capability of the PC-antenna with the optical pulse-shaping where we can freely manipulate the temporal profile of the optical pulses. Our technique provides a simple way to generate flexible THz waveforms. Also, this method does not suffer from a large loss of THz energy which is inherent in the shaping using antenna arrays or spatial filters. We also present a theory that quantitatively predicts THz radiation from the single pulse response and the temporal intensity profile of the shaped optical excitation pulse. We then demonstrate several examples of THz waveform synthesis, including amplitude and/or phase modulated THz radiation, binary bit sequences and tunable narrow-band THz radiation. We compare the experimental results with calculations using our theory and obtain excellent agreement between theory and experiment without any external adjustable parameters.

This chapter is organized as follows. In Sec. 3.2, the femtosecond optical pulse-shaping technology will be reviewed. In Sec. 3.3, we describe the theory which relates the measured THz radiation to the excitation pulse profile. Section 3.4 describes the experimental setup for generation of shaped THz radiation fields. In Sec. 3.5, we present several examples of shaped THz radiation. In Sec. 3.6, THz pulse-shaping using difference frequency generation will be briefed.

The work covered in this chapter was performed in collaboration with Dr. Yongqian Liu.

3.2 Femtosecond optical pulse-shaping

In this section, we describe the femtosecond optical pulse-shaping which is a integral part of our THz pulse-shaping technique. The femtosecond optical pulse-shaper was developed in the 1980's by Weiner and coworkers [71, 85, 73, 86, 75, 87, 88]. The basic principle of this pulse-shaper is that we separate each frequency component in space and apply any desired modulation to each separated frequency component. The schematic of this grating and lens pulse-shaper is shown in Fig. 3.1. It consists of two lenses, two gratings and a modulator at the center of symmetry plane. A femtosecond pulse entering the pulse-shaper is first dispersed in space by the first grating by following Eq. 3.1.

$$\sin\theta_d(\lambda) - \sin\theta_i = -\frac{\lambda}{d}, \tag{3.1}$$

where d is the grating groove period, λ is the frequency of the light, and $\theta_d(\lambda)$, θ_i are the diffracted and incident angle of the beams, respectively. Here, we assume the use of order (-1) diffracted beam off the grating. The individual spectral components separated by the grating is then focused at the mask plane by a lens. At that plane, the separation between the spectral components of the pulses is at its maximum. After being modulated at the mask plane, spectral components are recombined by another lens and grating. The beam leaving the pulse-shaper has temporal profile of the Fourier transform of the filter function of the modulator as given in Eq. 3.2.

$$e_{out}(t) = \frac{1}{2\pi}\int d\omega e^{i\omega t} H(\omega) \int dt' e^{-i\omega t'} e_{in}(t') \tag{3.2}$$

It should be noted that when there is no modulator, the the output pulse is identical to the input pulse.

As a modulator, both fixed masks fabricated on optical glass and programmable liquid crystal modulator (LCM) arrays have been used. With these modulators, 'amplitude only', 'phase only' and 'amplitude and phase' modulation have been demonstrated. Recently, the optical pulse-shaping employing acousto-optic modulators was demonstrated [90]. It has fast switching time between frames, but the result is still preliminary and also only useful for low repetition rate femtosecond systems which typically involve an optical amplifier. In this research, we used both programmable LCM array and fixed phase mask array fabricated on fused silica using micro-lithography. In the fixed phase mask, the phase modulation is introduced by etching the desired portion defined by micro-lithography thus changing the optical

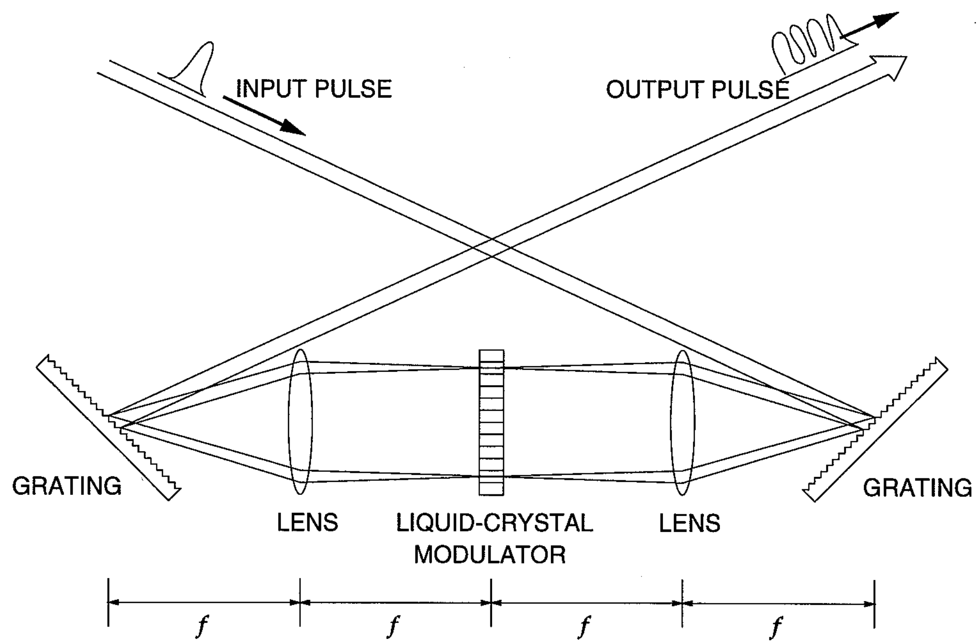

Fig. 3.1. Grating-Lens programmable pulse-shaper

path length for the light which passes that area. The operation of the more popular programmable LCM array is described in the next section.

3.2.1 Liquid crystal modulator

A basic LCM is a thin layer of liquid crystal which is sandwiched between two glass slides. The inner surface of the slides are coated with transparent indium tin oxide (ITO) conducting films. The ITO at one side is lithographically patterned into array of electrodes leaving small gap between them so that we can apply bias to individual pixels defined by the ITO electrodes. The ITO at the other side remains intact and is used as a ground plane. This structure is illustrated in the Figure 3.2.

Without any bias, the molecules in the LCM are aligned to the y-direction. As we apply the bias, they tend to tilt to the direction of the bias field (z-direction) which is in this case the direction of the optical beam path. When the orientation of the molecules is changed, the refractive index of the material along y-axis is changed while the refractive index along x-axis remains the same. If the light which is polarized in y-axis pass through the LCM, it experiences extra retardance from the change in the refractive index. Therefore, we can control the phase-retardation of the light passing through the modulator by controlling the voltage applied to the modulator array. Therefore, we have phase-only modulation. We can also get amplitude modulation by using a polarizer with the LCM. For example, let's say the input light polarization is along $(\hat{x} + \hat{y})/\sqrt{2}$ direction [$\mathbf{E} = E_0(\hat{x} + \hat{y})/\sqrt{2}$] and the crystal is oriented along y-axis as before. When the bias is applied, the modulated light is represented by $\mathbf{E} = E_0(\hat{x} + \hat{y}e^{i\Delta\phi})/\sqrt{2}$, where $\Delta\phi$ is the extra phase retardence experience by y-polarized polarization components. If we use a polarizer aligned to $(\hat{x} - \hat{y})/\sqrt{2}$, we get the output light for which the modulation function can be represented by $H = \cos(\Delta\phi/2)e^{i\Delta\phi/2}$. But in this case, the amplitude modulation is coupled to the phase modulation. In general, we cannot control the phase and the amplitude modulation independently with a single LCM.

Recently, a new scheme employing dual modulator arrays was demonstrated [73]. Using two modulator arrays, they successfully modulated the phase and amplitude of light independently. A schematic of a dual-LCM is shown in Figure 3.3. The dual-modulator unit is sandwiched between two polarizers aligned to x-direction. The two modulators are aligned to $\pm 45°$ from x-axis in the $x - y$ plane (the direction of light propagation is taken as z-axis). For x-polarized light, the filter function H_n for pixel

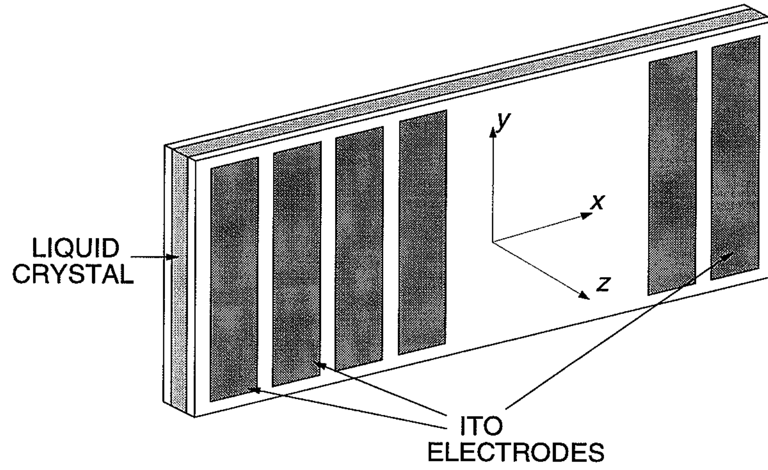

Fig. 3.2. Liquid crystal spatial modulator array

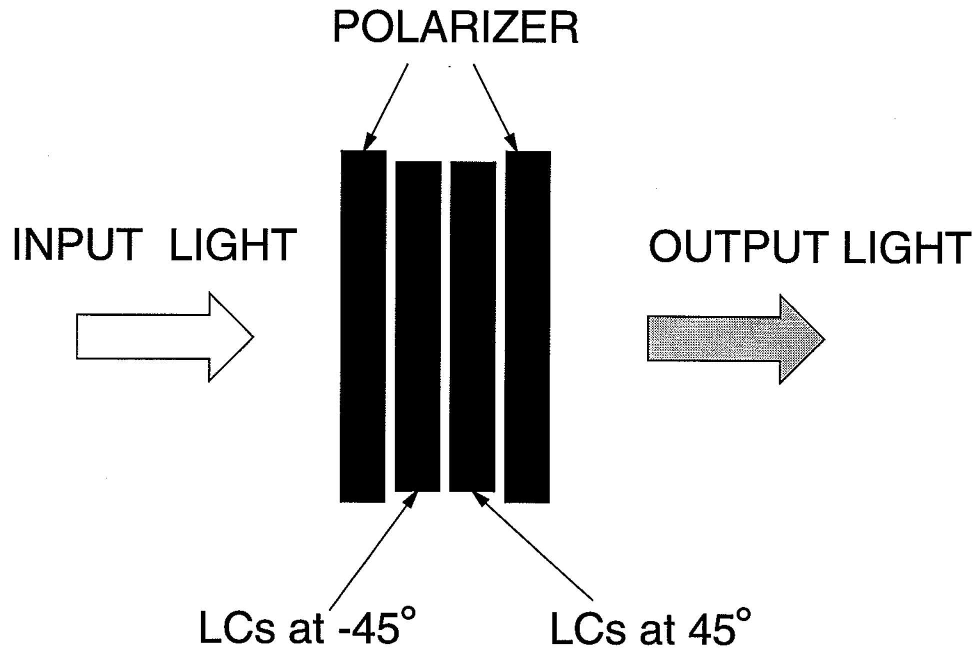

Fig. 3.3. Schematic of programmable pulse-shaping mask. The mask consists of two LCM with LCM aligned at ±45° from the x-axis and modulator pair is sandwiched by two polarizers aligned along the x-axis.

n is given by

$$H_n = \frac{1}{2}\{\exp(i\Delta\phi_n^{(1)}) + \exp(i\Delta\phi_n^{(2)})\} \tag{3.3}$$
$$= \exp[i(\Delta\phi_n^{(1)} + \Delta\phi_n^{(2)})/2]\cos[(\Delta\phi_n^{(1)} - \Delta\phi_n^{(2)})/2], \tag{3.4}$$

where $\Delta\phi_n^{(1)}$ and $\Delta\phi_n^{(2)}$ are phase retardation due to modulator 1 and 2. By manipulating $\Delta\phi^{(1)}$ and $\Delta\phi^{(2)}$ properly, we can control phase and amplitude independently. For example, if we want to use it as a phase modulator, we set $\Delta\phi^{(1)} = \Delta\phi^{(2)}$ and if we want to use it as a amplitude modulator we set $\Delta\phi^{(1)} = -\Delta\phi^{(2)}$. Generally to make $H_n = |H_n|\angle\phi_n$, we set $\Delta\phi_n^{(1)} = \phi_n + \cos^{-1}(|H_n|)$ and $\Delta\phi_n^{(2)} = \phi_n - \cos^{-1}(|H_n|)$

The dual LCM modulator described above was used in this research. The modulator was made by Cambridge Research and Instrumentation. It has 128 pixels of 2 mm height and 100 μm center-to-center separation with 3 μm gap between pixels. A calibration pixel of 2 mm by 2 mm size was made at an end of the modulator array to facilitate the calibration procedure.

In order to use the modulator in the pulse-shaper, we need to know the relation between the phase retardation induced by LCM and the applied voltage. This relation was obtained by using the modulator as a amplitude modulator (coupled with phase modulation). First fixing the bias of the one of the modulators (modulator A), the bias voltage of the other modulator (modulator B) was scanned and the optical power of the transmitted light was measured. Then, the bias of modulator A was scanned fixing the bias of modulator B. With these two sets of data, we can get the bias versus phase relationship for each modulator using Equation 3.4; one of these is shown in Fig 3.4. The modulator turns on at around 1 V, and the phase increases linearly at first. Then the increase of the phase slows down at high voltage as it saturates. We can get up to 8π of phase modulation with the dual LCM.

Fig. 3.5 shows examples of shaped pulses. Here we generated three pulse sequences with varying separations between the pulses. For these, the following filter function was used.

$$H(\omega) = \frac{1}{3}(1 + e^{-i\omega\tau} + e^{i\omega\tau}), \tag{3.5}$$

where τ is the spacing between the individual pulses in the pulse sequences. We have pulse trains of high contrast ratio. We can see the height of the peak becomes smaller when τ grows larger. It is mainly from the temporal Gaussian window which comes from the finite spot size of the individual frequency components on the mask plane [92].

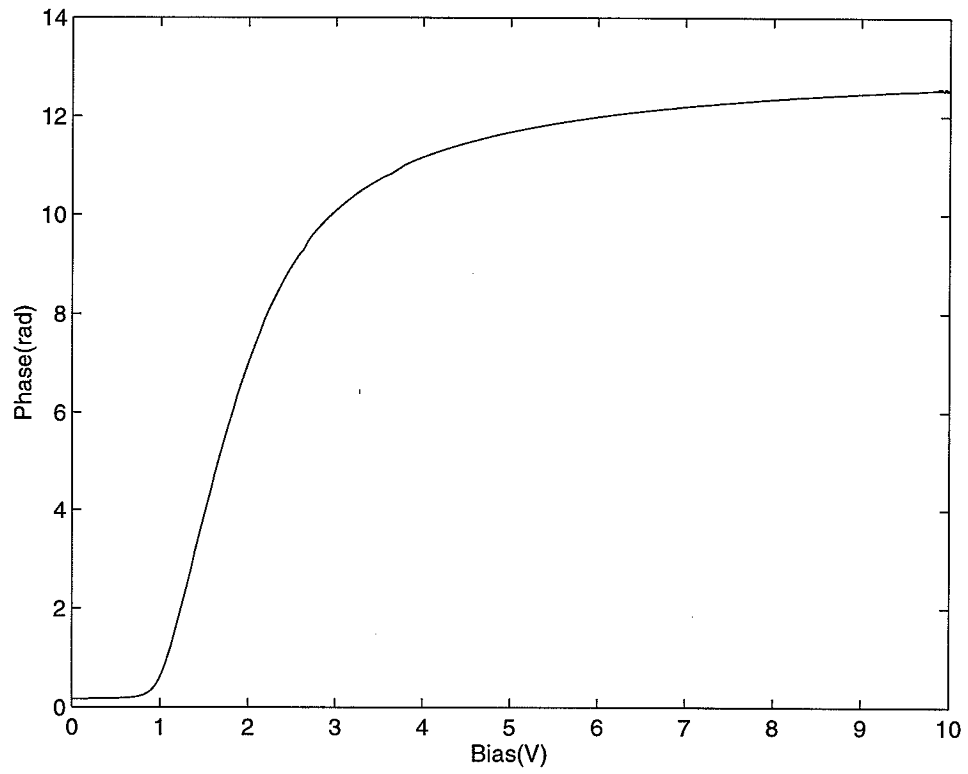

Fig. 3.4. Phase versus applied bias of a single LCM array

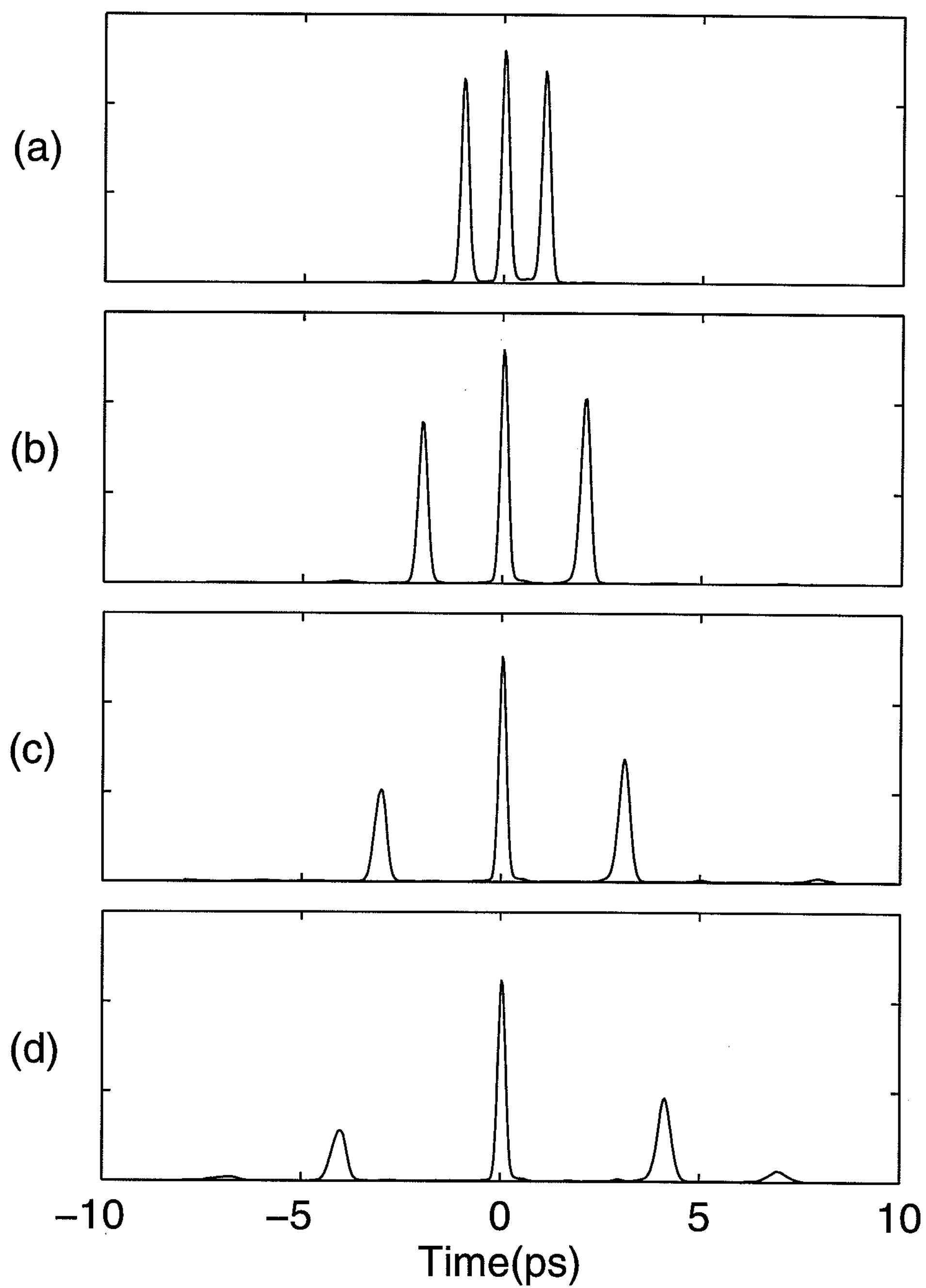

Fig. 3.5. Three pulse sequences with varying separations between pulses.

3.3 The theory of THz pulse-shaping

In this section, we develop a linear theory which predicts the temporal profile of the shaped THz radiation from the temporal intensity profile of the shaped optical excitation pulses and the characteristic response of the THz system. The principle of THz waveform synthesis we demonstrate in this chapter is to control the waveforms of THz radiation by shaping the temporal profile of the excitation optical pulses. The optical waveforms are generated by a femtosecond optical pulse-shaper and used to excite a PC-dipole antenna.

We use $e_{in}(t)$ and $e_{out}(t)$ to denote the electric field profiles of the pulses before and after the pulse-shaper, respectively. The pulse emerging from the pulse-shaper was given as Eq. 3.2 or in frequency domain given by Eq. 3.6,

$$\int dt\, e_{out}(t)\, e^{-i\omega t} = E_{out}(\omega) = E_{in}(\omega)H(\omega), \tag{3.6}$$

where $E_{out}(\omega)$ and $E_{in}(\omega)$ are the Fourier transforms of $e_{out}(t)$ and $e_{in}(t)$, respectively, and $H(\omega)$ is the effective frequency filter implemented by the masks within the pulse-shaper. The output profile of the shaped optical pulse is written as $I_{out}(t) \sim |e_{out}(t)|^2$, with Fourier transform [86],

$$\int dt\, I_{out}(t)\, e^{-i\omega t} = \tilde{I}_{out}(\omega) = \int d\Omega\, E^*_{out}(\Omega)E_{out}(\Omega + \omega). \tag{3.7}$$

Here, $\tilde{I}_{out}(\omega)$ denotes the Fourier transform of $I_{out}(t)$.

The generated THz radiation originates from the transient current induced by the optical pulses. In the linear response regime, the radiation field is given by the convolution of the intensity profile of the exciting optical pulse and the emitter response. Now we consider a PC-emitter illuminated by pulses from the optical pulse-shaper. The transient current density in the transmitter can be described by

$$j_T(t) = \sigma_s(t)E_{dc} \sim I_T(t) \otimes R_T(t), \tag{3.8}$$

where $\sigma_s(t)$ is the surface conductivity, E_{dc} is the bias field, $\otimes$ denotes convolution, and $I_T(t)$ is the exciting optical pulse intensity on the transmitter. $R_T(t)$ is the photocurrent response function of the transmitter but the exact form of $R_T(t)$ is not important to our theory. Eq. 3.8 is valid when the bias field E_{dc} is constant and there is no saturation mechanism. When the PC-antenna is excited by high fluence optical pulses, its behavior deviates from linear operation. Therefore, the validity of this model is limited to the case when the optical fluence of the excitation pulse is kept

sufficiently small. We can obtain the spectral amplitude of the transient current by performing a Fourier transform of Eq. 3.8.

$$J_T(\omega) = \tilde{I}_T(\omega)\tilde{R}_T(\omega), \tag{3.9}$$

where $\tilde{R}_T(\omega)$ is the Fourier transform of the transmitter photocurrent response $R_T(t)$. In general, the radiation field $E_{rad}(\omega)$ can be related to the transient current $J_T(\omega)$ by a characteristic frequency-dependent antenna response $K_T(\omega)$ as in Eq. 3.10.

$$E_{rad}(\omega) = K_T(\omega)\tilde{I}_T(\omega)\tilde{R}_T(\omega) \tag{3.10}$$

When we measure the field in the far-field region, the antenna response can be represented by $K_T(\omega) \sim i\omega$ since the radiation field follows the time-derivative of the current profile. Again, the exact form of $K_T(\omega)$ is not important to our derivation.

In our studies, we used the unshaped optical excitation pulse as a reference which characterized the THz system response. Then the THz response from the shaped excitation was obtained from this THz system response. The unshaped and shaped pulse can be represented from Eqs. 3.6 and 3.7 as follows.

$$\tilde{I}_T(\omega) = \int d\Omega E_{in}^*(\Omega)E_{in}(\Omega+\omega)H^*(\Omega)H(\Omega+\omega) \tag{3.11}$$

$$\tilde{I}_{in}(\omega) = \int d\Omega E_{in}^*(\Omega)E_{in}(\Omega+\omega), \tag{3.12}$$

where $\tilde{I}_{in}(\omega)$ is the Fourier transform of the intensity profile of the unshaped input optical pulse. Now, using Eqs. 3.11 and 3.12 in Eq. 3.10, we can rewrite the radiated field $E_{rad}(\omega)$ as

$$E_{rad}(\omega) = S(\omega)H'(\omega), \tag{3.13}$$

where $S(\omega)$ is the characteristic THz system response resulting from the unshaped pump $I_{in}(t)$ and is given by

$$S(\omega) \sim K_T(\omega)\tilde{I}_{in}(\omega)\tilde{R}_T(\omega), \tag{3.14}$$

and $H'(\omega)$ is the effective response function of the pulse-shaper in terms of the optical intensities and is defined by

$$H'(\omega) = \frac{\tilde{I}_T(\omega)}{\tilde{I}_{in}(\omega)}. \tag{3.15}$$

It should be noted that $H'(\omega)$ is different from $H(\omega)$.

Eqs. 3.13~3.15 represent one of our key results. They indicate that the shaped THz radiation $E_{rad}(t) = (1/2\pi)\int d\omega \tilde{E}_{rad}(\omega)e^{i\omega t}$ is equal to the convolution of the

THz response function observed for unshaped pulses with an effective impulse response function for the pulse-shapers. If the unshaped input pulses are very short compared to the photocurrent response functions, the THz response function $S(\omega)$ is approximately independent of the input pulse duration; in this case the waveform $E_{rad}(\tau)$ observed in response to a shaped pump pulse is just the unshaped pulse THz response convolved directly with the shaped intensity profile.

From the above equations, it is obvious that linear filtering of the optical field can be used to modify THz radiation field. Thus, the ability to shape optical pulses can be extended to control the shape of THz waveforms, provided that the response of the THz system is sufficiently fast, i.e., the single pulse response $S(\omega)$ has enough bandwidth; we cannot generate new frequency components through linear filtering.

The PC-antenna is driven by the optical intensity of the excitation pulse. This fact has some implications on our THz pulse-shaping. Firstly, the fact that the emitter is driven by the intensity limits the THz waveforms which can be generated in this method and this will be discussed further in Sec. 3.6. Also, since the phase profile of the optical pulse can be arbitrarily set without changing the intensity profile, in general more than one pulse-shaping filter $H(\omega)$ is available to produce the required optical intensity profile $I(t)$ of the excitation pulse. This has the practical implication that $H(\omega)$ can often be implemented as a phase-only filter [93].

In order to compare our experiments with theory, we use Eq. 3.13 to calculate the expected THz waveforms with a given mask function in the pulse-shaper using the measured $H'(\omega)$ together with the measured THz system response $S(\omega)$ obtained from single optical pulse excitation experiments. An expression for $H'(\omega)$ can be obtained experimentally using the intensity cross-correlation data. Expressions for the cross-correlation of the shaped and the unshaped pulses with unshaped pulses directly from the laser are given respectively as follows:

$$X_T(\tau) = \int dt I_T(t) I_{in}(t-\tau) \tag{3.16}$$

$$X_{in}(\tau) = \int dt I_{in}(t) I_{in}(t-\tau). \tag{3.17}$$

The Fourier transforms of the intensity cross-correlations are given by

$$\tilde{X}_T(\omega) = \int d\tau X_T(\tau) e^{-i\omega\tau} = \tilde{I}_T(\omega)\tilde{I}_{in}^*(\omega) \tag{3.18}$$

$$\tilde{X}_{in}(\omega) = \int d\tau X_{in}(\tau) e^{-i\omega\tau} = \tilde{I}_{in}(\omega)\tilde{I}_{in}^*(\omega). \tag{3.19}$$

The $H'(\omega)$ is determined by dividing the Fourier transformed cross-correlation data

$$H'(\omega) = \frac{\tilde{I}_T(\omega)}{\tilde{I}_{in}(\omega)} = \frac{\tilde{X}_T(\omega)}{\tilde{X}_{in}(\omega)}. \tag{3.20}$$

This approach using only measured data takes into account any non ideal mask responses from pulse-shaper as well as lack of complete knowledge about the photoconductive material parameters. The examples shown later in this chapter verify that this calculational approach produces an excellent agreement with shaped pulse experiments with no adjustable parameters.

Note that our calculation should not be limited to THz waveforms design using particular optical pulse-shaper used in this research. It could also be applied to general cases of THz waveform synthesis based on optical pulse-shaping using other techniques.

3.4 Experimental setup

A schematic diagram of the experimental setup is shown in Fig. 3.6. We used a Ti:Sapphire laser (Spectra Physics Tsunami) producing ~100 fs pulses at a repetition rate of 80 MHz around a center wavelength of 800 nm. The femtosecond laser output is split into two beams. One of them is used as the pump to a transmitting antenna while the other is used as the probe beam gating a receiving antenna. The antennas were PC small dipole antennas fabricated on subpicosecond carrier lifetime LT-GaAs. The small dipoles were embedded in the transmission lines which connected the antenna to the biasing or detection circuitry. The dipoles and transmission lines were fabricated by depositing Ti-Au. The separation between the transmission lines was 30 μm and the small gap in the dipole antenna was 5 μm.

A pulse-shaper is used in the pump beam to design the exciting optical pulse intensity profiles. The pulse-shaping apparatus was shown in Fig. 3.1. It consists of a pair of 1800-line/mm gratings and a pair of 15 cm focal length achromatic lenses. The optical pulse-shaping is accomplished by a programmable liquid crystal modulator (LCM) or fixed phase mask fabricated on fused silica. As mentioned in Sec. 3.2.1, the LCM which we used was a combination of two 128-element liquid crystal modulators that can filter both the amplitude and the phase of the optical spectrum. The detailed operation principle of this device was described in the Sec. 3.2.1. The LCM was controlled through a home-made computer graphical interface to set the driving voltage of each modulator element using a calibration table relating the filter function

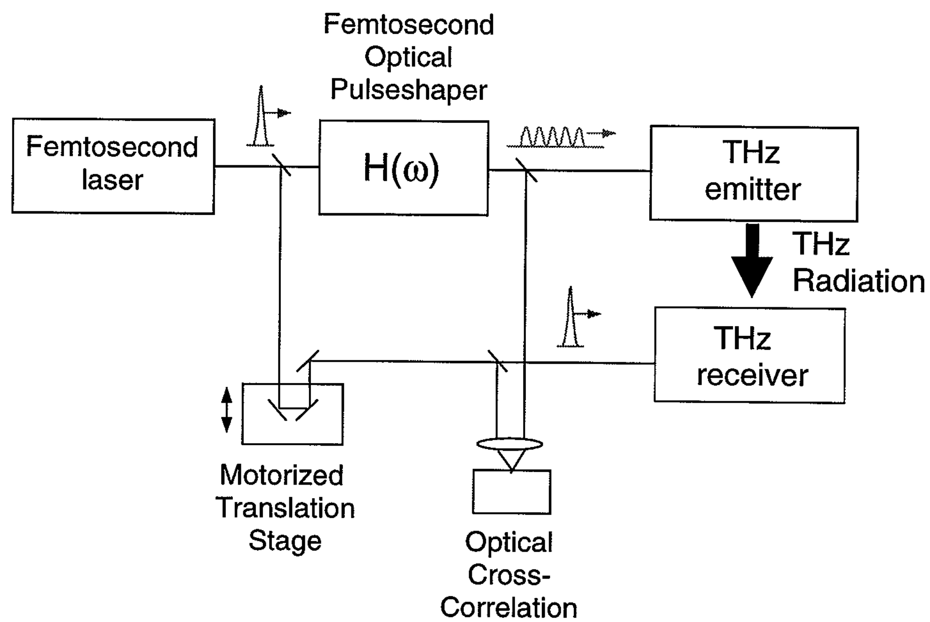

Fig. 3.6. The schematic of the setup for THz pulse-shaping employing femtosecond optical pulse-shaper and PC-antennas.

$H(\omega)$ and the driving voltage. Intensity profiles of the shaped pulses are measured by cross-correlation via second harmonic generation in non-colinear geometry, using pulses directly from the laser as the reference. The shaped optical pulses are focused to a $\sim 10\,\mu$m spot on the transmitting antenna. The dipole antennas are mounted on high-resistivity silicon hyper-hemispherical lenses which has a 10-mm diameter and a center thickness of 6.4 mm. The transmitting antenna is biased by a dc power supply with ~ 25 V. The THz radiation from the transmitting dipole is collected by the silicon lens attached to the transmitter and propagates to the receiver through the free space. There it is focused by another silicon hyper-hemispherical lens onto a receiving dipole. The receiver was placed ~ 10 cm away from the transmitter. The unshaped optical probe beam was used as a trigger to sample the THz radiation field sensed by the detector. The current signal, which is proportional to the radiated field, was amplified by a current preamplifier and recorded by a lock-in amplifier. The THz radiation was mapped out as a function of the time by scanning the delay between the excitation pulse and the sampling pulse. A typical pump average power of ~ 7 mW and probe average power of ~ 20 mW were used in the following experiments.

3.5 Results

In this section, we demonstrate several examples of THz waveform synthesis by using different optical pulse sequences. We will show that both the phase and amplitude profiles of THz waveforms can be modulated. In order to compare our experimental results with calculations, for every data set we measured the characteristic THz system response $S(\omega)$ using single-pulse excitation in order to account for any changes due to day-to-day variations in the system alignment. Fig. 3.7 shows an example of the THz response $S(\tau) = \int d\omega e^{i\omega\tau} S(\omega)$. In each case, we also performed intensity cross-correlation measurements of both the shaped and unshaped optical pulses using pulses directly from the laser as the reference.

3.5.1 Terahertz internal phase modulation

As the first example, we demonstrate control of the phases of a six-cycle THz radiation waveform. We accomplish this by designing sequences of six optical pulses with different separations. The filter function we used is the Fourier transform of a sequence of delta functions. Eq. 3.21 and 3.22 represent the filter function used here.

$$H_1(\omega) \;=\; e^{-2i\omega\tau} + e^{-i\omega\tau} + 1 + e^{i\omega\tau} + e^{2i\omega\tau} + e^{3i\omega\tau} \qquad (3.21)$$

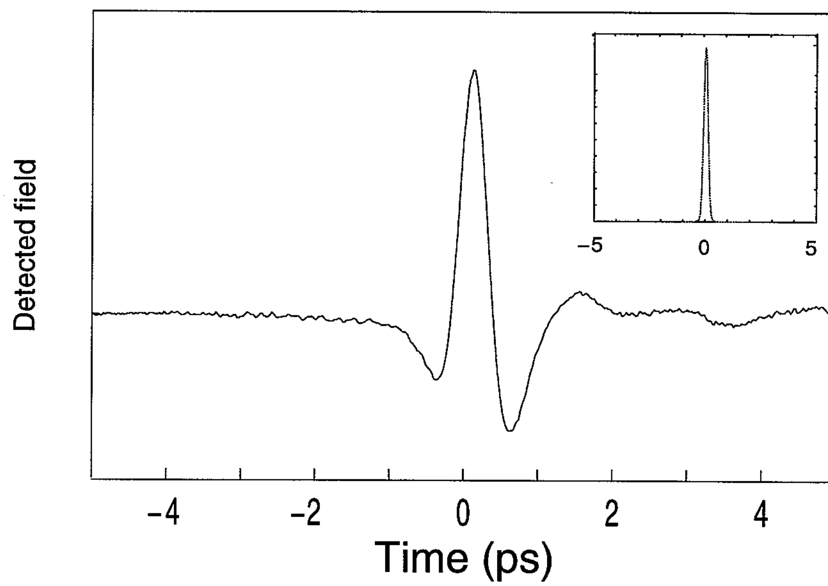

Fig. 3.7. Typical characteristic THz system response with single-pulse optical excitation. The inset shows the optical cross-correlation of unshaped pump pulses with pulses directly from the laser as the reference.

$$H_2(\omega) \quad = \quad e^{-2i\omega\tau} + e^{-i\omega\tau} + 1 + e^{1.5i\omega\tau} + e^{2.5i\omega\tau} + e^{3.5i\omega\tau}, \tag{3.22}$$

where ω corresponds to the optical frequency. $H_1(\omega)$ represents the six pulse sequence of temporal spacing τ, while $H_2(\omega)$ represents the pulse sequence where the latter three pulse were displaced by $\tau/2$ in time. Control of the internal phase of the resultant THz waveform can be achieved simply by modifying the separations between pulses. As long as the THz response function is fast enough to respond to each pulse, the phases of individual THz cycles are changed as a result of the optical pulse timing.

Fig. 3.8 (a) shows the cross-correlations between six-pulse optical pulse sequences from the pulse-shaper and the unshaped pulse. The first (I) has equal pulse spacing [Eq. 3.21, $\tau \sim 0.8$ ps.]; The second (II) has an extra time delay at the fourth pulse. [Eq. 3.22, $\tau \sim 0.8$ ps] The THz waveforms resulting from these excitation pulse sequences are shown in Fig. 3.8 (b). The first pulse sequence generated a quasi-sinusoidal THz waveform with a constant frequency corresponding to the repetition rate of the six-pulse sequence. The second waveform generated a similar THz waveform but with a π phase shift occurring between the third and fourth THz cycle. The phase reversals at the instants of time shown by the dashed lines are clearly visible. Internal phase modulation, as demonstrated in this simple example, could potentially be used to generated orthogonal THz waveforms with reduced cross-talk for communication applications.

Fig. 3.8 (c) shows THz waveforms calculated based on Eqs. 3.13 and 3.15 using the measured THz system response from an unshaped pump pulse as well as the cross-correlation measurements of the unshaped pulse and the shaped optical pulse sequences [see Fig. 3.8 (a)]. An excellent agreement with the experimentally observed THz waveform is observed. It should be noted that no adjustable parameters were used in these calculations; only the measured single-pulse THz response and the measured intensity cross-correlations of unshaped and shaped optical pulses are needed. The agreement validates the role of the optical pulse-shaper in THz waveform synthesis as described in Sec. 3.3.

3.5.2 THz amplitude modulation

The next demonstration of our technique is the generation of THz waveforms forming binary bit sequences. These binary bit sequences could be valuable to various applications. For example, these could be used for high speed chip-to-chip or board-to-board interconnect systems involving high-speed time-division multiplexed (TDM)

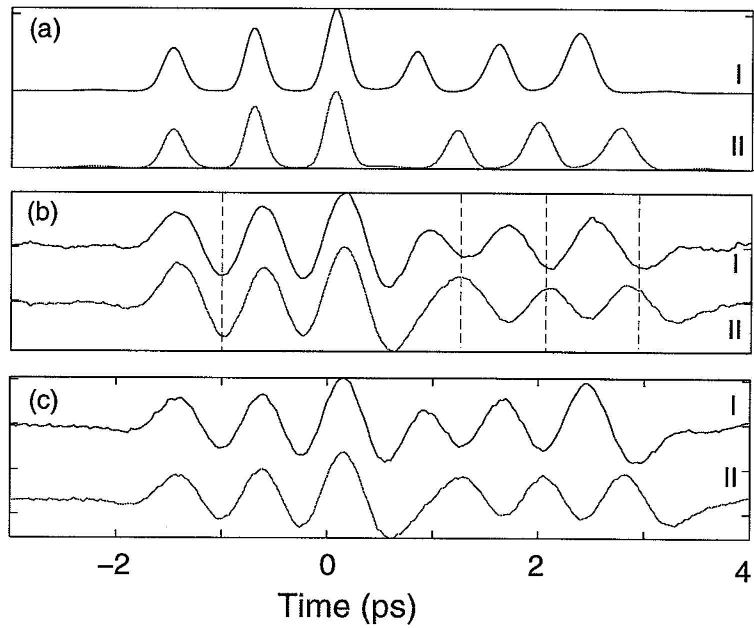

Fig. 3.8. Optical cross-correlation of six-pulse sequences and the corresponding THz radiations demonstrating the phase modulation of THz radiation (a) measured optical cross-correlation of two designed six-pulse sequences: (I) equally time-spaced (II) an extra time delay at the fourth pulse. (b) measured THz radiation from the two pulse sequences. (c) calculated THz radiation using the measured characteristic THz system response and cross-correlation data

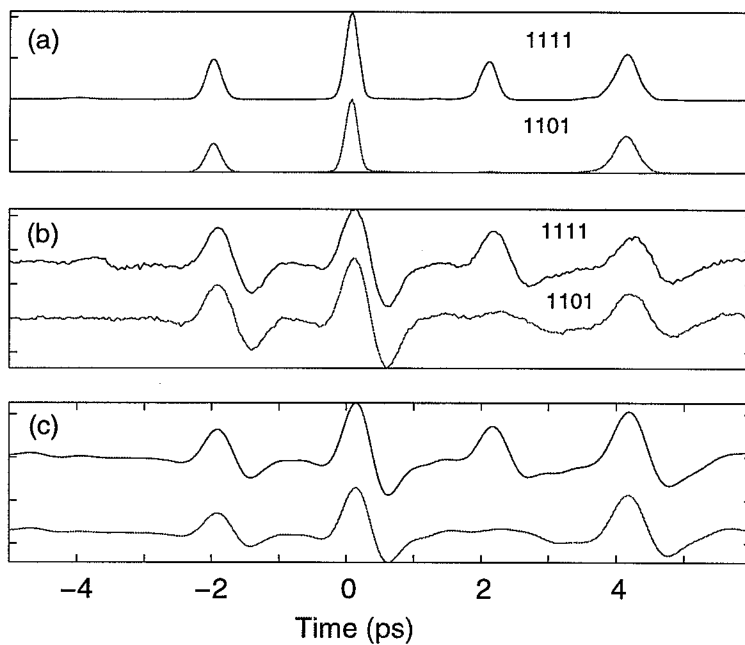

Fig. 3.9. Terahertz time-domain multiplexing of two 4-bit words. (a) measured optical cross-correlation of input pulses. (b) measured THz radiation as a result of the two encoded sequences. (c) calculated THz radiation of the two 4-bit words based on THz system response using measured characteristic THz system response and cross-correlation data.

data. Similar bit sequences have been demonstrated by illuminating PC-antenna arrays using space-to-time mapping [79]. Compared to that work, our optical pulse-shaping approach can be applied to more complicated bit sequences which in turn allows more complex encoding.

Fig. 3.9 shows one set of our data, where we used two different femtosecond pulse sequences to generate THz waveforms encoded as two different 4-bit words. The optical pulse sequences consist of up to four pulses with pulse separation of ~2 ps as shown by the cross-correlation trace in Fig. 3.9 (a). They represent [1111] and [1101] 4-bit sequences with each peak of the pulses representing one, respectively. These modulated optical signals are directly transferred to THz waveforms as shown by the corresponding THz measurement in Fig. 3.9 (b). Fig. 3.9 (c) shows the calculated radiation field based on Eqs. 3.13 and 3.15. Again, we can see a very close agreement between the calculation and the experimentally observed results shown in Fig. 3.9 (b). We can estimate the maximum data rate of this system as following. The maximum data rate is determined by either minimum optical pulse separation or the bandwidth of the THz system. When we use ~100 fs pulses, usually we can position the pulses as close as 300 fs from each other. In that case, the THz system response will be the bottleneck. With current bandwidth of about 2 THz of the system response, the maximum data rate would be less than 1 Tbit/sec.

3.5.3 Tunable narrow-band THz radiation

As the final demonstration of the THz pulse-shaping, we generated tunable narrow-band THz radiation. When the spectrum of a short pulse is periodically modulated $[H(\omega + \Omega_p) = H(\omega)]$, the time domain electric field becomes sequence of pulses whose separation is given by $T = 2\pi/\Omega_p$. Therefore, by modulating the optical pulse spectrum with the tunable modulation period, we can obtain an optical pulse train whose spacing between the pulses can be tuned. The relation of the optical repetition rate and phase mask periodicity can be described by

$$\nu_0 = \frac{c\, d \cos\theta_d\, \Delta x}{F\lambda^2}, \tag{3.23}$$

where ν_0 is the repetition frequency of a designed pulse sequence, c is the speed of light, d is the grating period, θ_d is the focal length of lens after the grating, λ is the optical wavelength, and Δx is the spatial period of the phase mask. If we use these pulse trains to excite THz emitters, we can get tunable THz radiations. For this we used a phase-only filter which consists of periodic repetitions of M-sequence [94].

In order to demonstrate the generation of tunable narrow-band radiation, we tuned the center frequency ν_0 through the control of the mask spatial period Δx. Our M-sequence was fabricated on fused silica. This M-sequence phase mask is similar to the ones used in Ref. [71, 86, 88]. The phase mask contains a series of approximately 20 one-dimensional phase patterns, where each individual pattern is designed as a periodic repetition of an M-sequence, as described above. The spatial periodicity varies from pattern to pattern, and therefore, the pulse repetition period ν_0 can be tuned by physically translating the mask to place different patterns in front of the spatially dispersed optical beam. For comparison, the mask also contains a blank constant phase area which produces a single unshaped optical pulse.

Fig. 3.10 shows the Fourier transforms of the intensity cross-correlation of an unshaped optical pulse and a shaped optical pulse pulse sequence. We can clearly observe that the periodic optical phase mask acts as a periodic narrow-band filter which selects only certain frequency components from $\tilde{I}(\omega)$, the Fourier transform of the temporal intensity profile. Again it should be stressed that this frequency selection is not occurring for the Fourier transform of the electric field. The spectral amplitude at the selected frequencies are the same as for the unshaped pulse. This can be understood with the reference to Eq. 3.6 and 3.7, which show that $I(\omega)$ is given by the correlation function of the masked optical spectrum $E(\omega)$. As long as the filter $H(\omega)$ is a periodic phase-only function, the correlation is unchanged by the phase mask for frequencies $\nu_n = n\nu_0$, where n is an integer and ν_0 is determined by the spatial periodicity of the mask through Eq. 3.23.

Fig. 3.11 shows the THz radiation measured (solid lines) using this phase mask for several representative cases: $\Delta x =$ (a) 0.875 mm, (b) 0.717 mm, (c) 0.625 mm. The THz radiation shows quasi-sinusoidal waveforms with center frequencies equal to the repetition frequencies of the optical pulse trains generated from each phase pattern. The phase shift $\Delta\Phi = 0.84\pi$ was used in order to have a central pulse amplitude consistent with a smooth pulse sequence envelope. The center frequency of the narrow-band THz radiation is tuned as a result of varying the spatial period of the mask patterns, which changes the optical pulse repetition frequency. Dashed lines in Fig. 3.11 represent the respective THz waveforms from calculations based on Eq. 3.13 and 3.15 using the measured THz system response [Fig. 3.11 (a)] together with measured cross-correlations (not shown). The calculations show a smaller temporal window due to shorter temporal scans in cross correlation measurements. Once

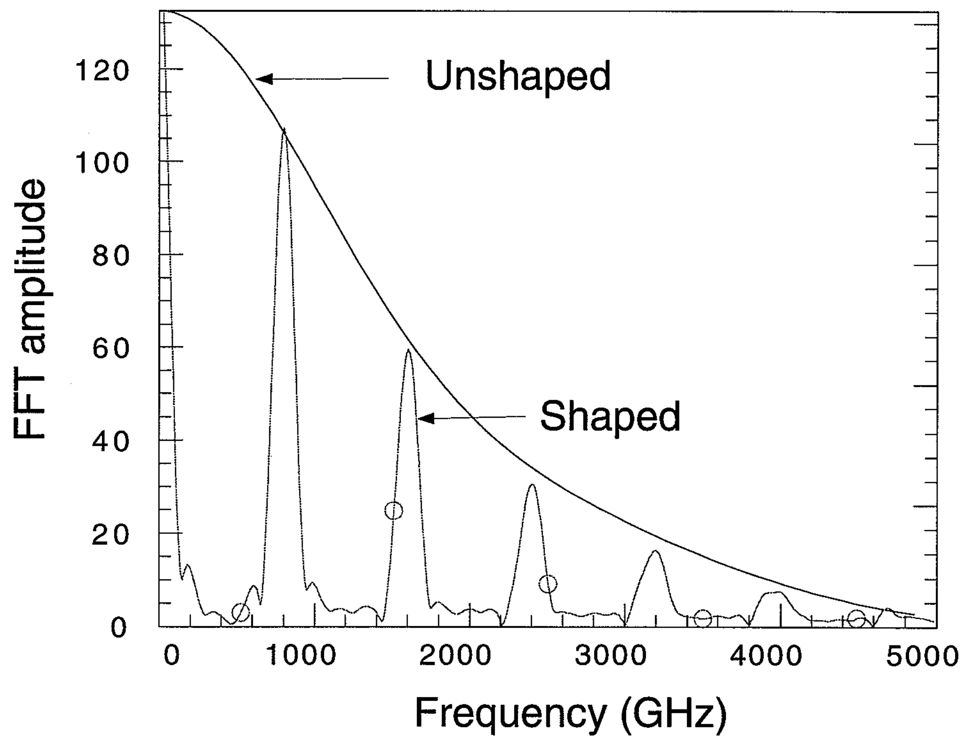

Fig. 3.10. Fourier transform of measured intensity cross correlation of single and multiple optical pulses

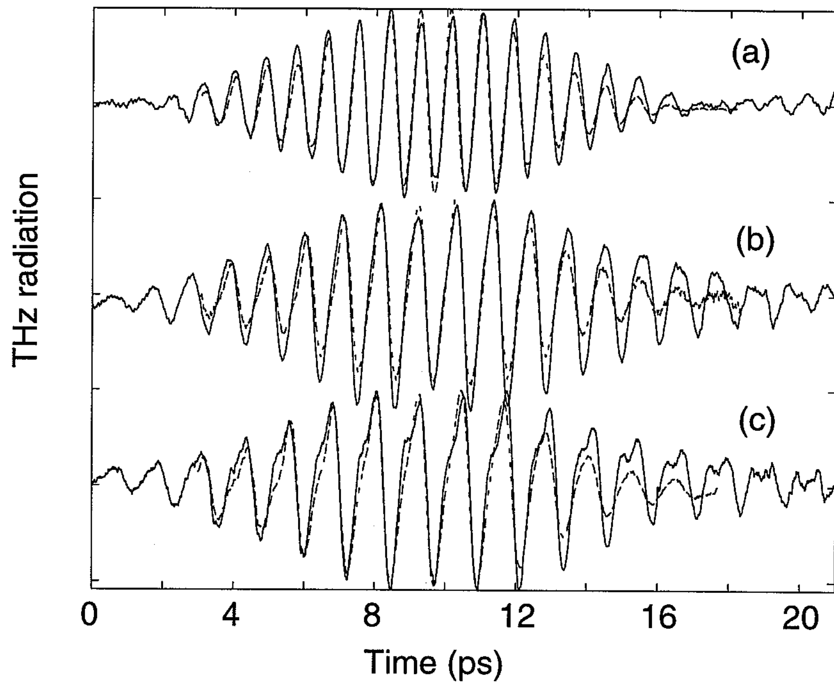

Fig. 3.11. Measured (solid lines) and calculated (dashed lines) THz radiation with fixed periodic M-sequence phase mask: (a) Δx=0.878 mm, (b) Δx=0.717 mm, (c) Δx=0.625 mm

again, we obtain a very good agreement between theory and experiment, including the shapes of the individual THz features making up the quasi-sinusoidal burst.

Fig. 3.12 shows the Fourier transforms of the time-domain THz waveforms from Fig. 3.11 along with the Fourier transform of the single-pulse excited THz radiation. As expected, the single-pulse radiation is broad-band with spectral content extending up to 2.5 THz (limited by our detector bandwidth). The narrow-band radiation from the pulse sequences shows both first-harmonic and second-harmonic peak within our bandwidth. This figure clearly indicates the frequency tuning of the center wavelength of the narrow-band radiation by the spatial periodicity of the phase mask. It can be noticed that the spectral peak amplitude at the first harmonic of the narrow-band radiation is enhanced compared to single-pulse radiation envelope. Chap. 4 will cover this phenomenon which is related to the saturation of the PC-emitter.

Fig. 3.13 shows the center frequency of the narrow-band radiation as a function of spatial period Δx. We have demonstrated a tuning range from 750 GHz up to 1.3 THz with our current mask and our pulse-shaper design. As indicated by the fitted dashed line, the center frequency of the radiation field linearly depends on Δx. This is in reasonable agreement with Eq. 3.23 and our estimated pulse-shaper parameters. We should point our that the tuning range of this technique is not limited to the range illustrated here. With proper design of the phase mask, we can expect an even wider frequency tuning range.

3.6 THz pulse-shaping using difference frequency mixing

3.6.1 Motivation

As mentioned in the Sec. 3.3, THz pulse-shaping using PC-antenna has limitations which result from driving the PC-antenna by the optical intensity of the excitation pulses, which is always non-negative. One simple example of the shaping we are not capable of performing in this scheme is reversing the polarity of the THz field. Eq. 3.13 and 3.15 are repeated here.

$$E_{rad}(\omega) = S(\omega)H'(\omega) \tag{3.24}$$

$$H'(\omega) = \frac{\tilde{I}_T(\omega)}{\tilde{I}_{in}(\omega)} \tag{3.25}$$

From Eq. 3.24 and 3.25, it is obvious that we need to make $\tilde{I}_T(\omega) = -\tilde{I}_{in}(\omega)$ to have the polarity of THz radiation $E_{rad}(\omega)$ reversed, which it is not possible. This

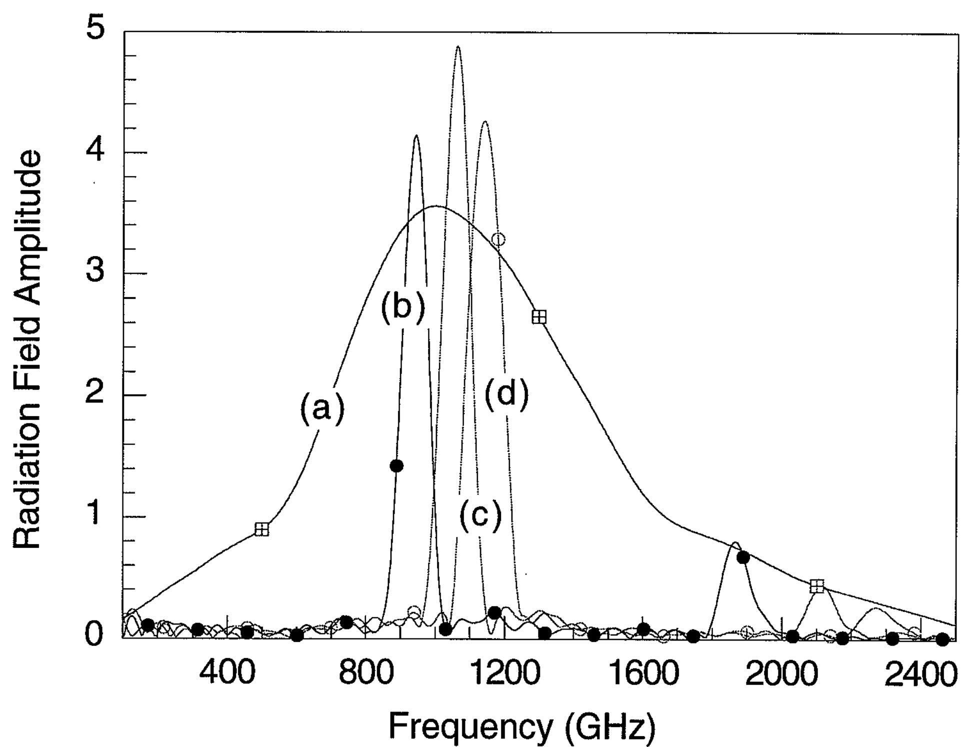

Fig. 3.12. FFT field spectral amplitude showing the tuning of narrow-band frequencies through changes of the spatial period: (a) Single-pulse, (b) Δx=0.878 mm, (c) Δx=0.717 mm, (d) Δx=0.625 mm.

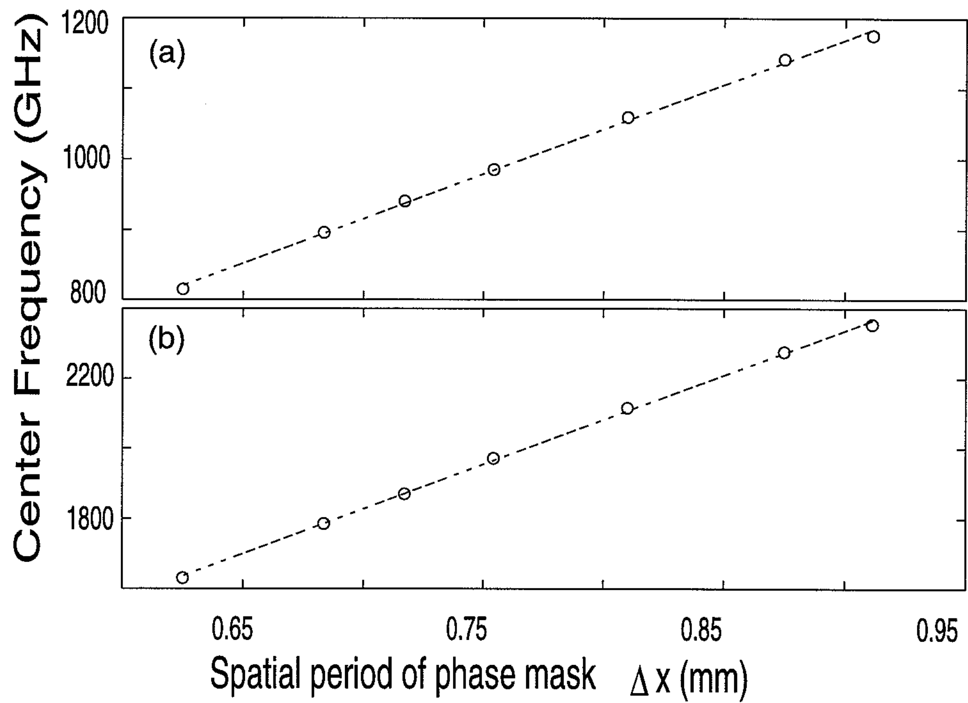

Fig. 3.13. Tuning range of the narrow-band THz radiation with current apparatus: (a) First-harmonic (b) Second harmonic

limitation can be avoided by using emitters sensitive to the electric field itself not to the intensity. In that case, we can control the polarity of the THz radiation by changing the polarity of the electric field.

In this section, we propose a THz pulse-shaping scheme which use difference frequency mixing (DFM) in the electro-optic crystal as the THz generation mechanism. We expect by using this scheme we can generate arbitrary THz waveforms overcoming the limitations on the THz pulse-shaping using PC-emitters. In Sec. 3.6.2, we describe the theory of THz pulse-shaping using difference frequency mixing and in Sec. 3.6.3 some preliminary results will be presented.

3.6.2 Theory of THz pulse-shaping employing emitter using difference frequency generation

When an electric field **E** propagates in an electro-optic crystal which has second order electro-optic tensor χ, the non-linear polarization **P** is generated by difference frequency mixing and given by [95]

$$P_i(t) = \sum_{jk} \chi_{ijk} E_j(t) E_k^*(t) + c.c., \tag{3.26}$$

or in the frequency domain

$$P_i(\omega) = \sum_{jk} \chi_{ijk} \int d\omega E_j(\Omega) E_k^*(\Omega - \omega) + c.c. \tag{3.27}$$

Here, we assumed frequency independent χ. This newly generated nonlinear polarization acts as a source of THz radiation [96, 97, 15, 98]. From the above equations, it is clear that by changing the relative polarity of E_j to that of E_k we can change the polarity of the polarization P_i. To do this, we should use two beams. If we have just one beam, when we change the polarity of E_i, the polarization of E_k is also reversed and therefore, we can only generate THz in a mechanism which is sensitive to the intensity of the excitation.

In general, the difference frequencies are generated from both the self-term ($j = k$) and cross-terms ($j \neq k$). In order to use DFM for THz pulse-shaping, we should be able to separate these two. One way of doing it is using <110> oriented Zinc Blend crystals. A simple diagram which represents the electric field at the fundamental frequency and the polarization field at the difference frequency in a <110> crystal is shown in Fig. 3.14. In a Zinc Blend crystal, the only non-vanishing second-order nonlinear tensor element is χ_{123} with the subscripts interchangeable. When the polarization of the incoming electric fields are <001> (E_v) and <110> (E_h) as in

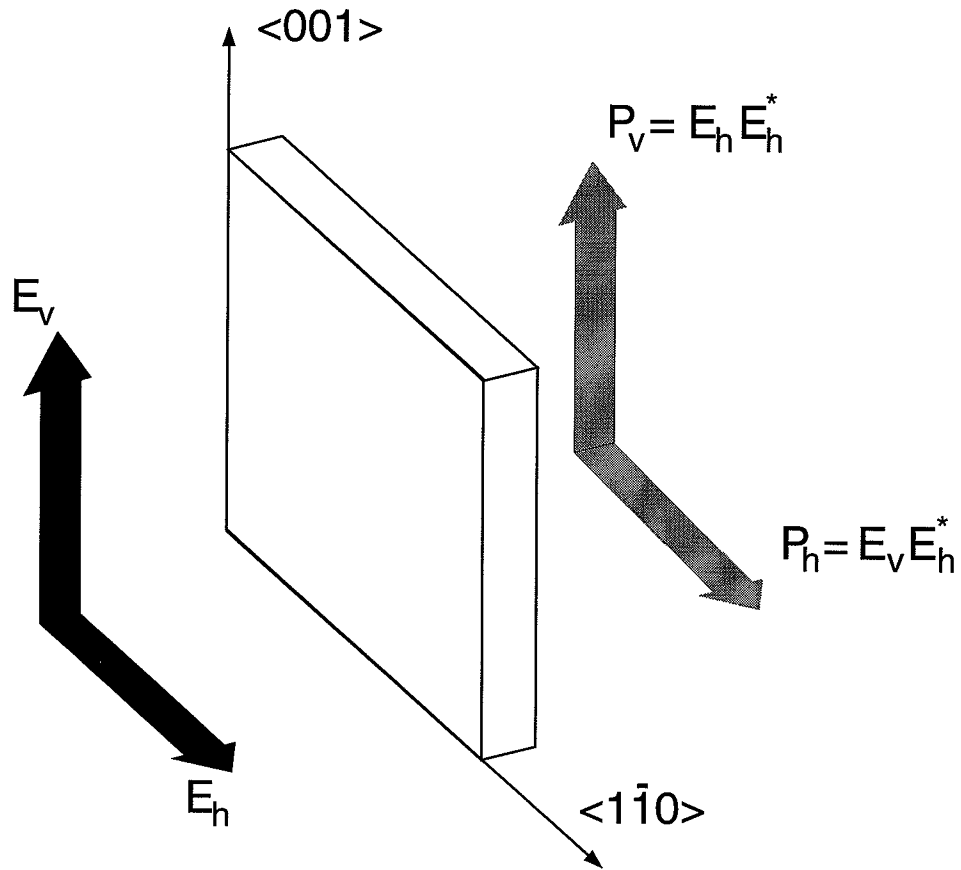

Fig. 3.14. The diagram showing the difference frequency generation in <110> ZnTe crystal. E_v,E_h: electric field at fundamental frequency, P_v,P_h: polarization at the difference frequency

Eqs. 3.28 and 3.29,

$$\mathbf{E_v} = E_{v0}\,\hat{z} \tag{3.28}$$

$$\mathbf{E_h} = \frac{E_{h0}}{\sqrt{2}}(-\hat{x}+\hat{y}), \tag{3.29}$$

the nonlinear polarization can be calculated as

$$\mathbf{P_v} = -\chi E_{h0}E_{h0}^{*}\,\hat{z} + c.c. \tag{3.30}$$

$$\mathbf{P_h} = -\chi E_{v0}E_{h0}^{*}\frac{(-\hat{x}+\hat{y})}{\sqrt{2}} + c.c.. \tag{3.31}$$

From Eqs. 3.30 and 3.31, we observe that $\mathbf{P_h}$ is from the cross-term of $\mathbf{E_v}$ and $\mathbf{E_h}$ while $\mathbf{P_v}$ is from the self-term of $\mathbf{E_v}$. Therefore, if we use a polarizer, we can separate the self-term from the cross-term.

Since the two electric field components are used to synthesize a desired electric filed, it is important to maintain the relative phase of two beams precisely. This requires interferometric precision.

3.6.3 Preliminary results

In order to test the feasibility of our new THz pulse-shaping scheme, we performed a THz generation experiment with a single pump beam. Here, we checked the generation of the nonlinear difference frequency polarization. We generated THz radiation using a <110> ZnTe crystal and detected the radiation using PC-detection. We changed the incoming light polarization using a half-wave plate and the <001> direction of the crystal was oriented in vertical (z) direction. When the polarization of the incoming light makes angle θ with the z-axis, the resulting nonlinear polarization can be expressed as

$$P_h = -\frac{\chi}{2}\sin 2\theta\, E_0E_0^{*} \tag{3.32}$$

$$P_v = -\frac{\chi}{2}(1-\cos 2\theta)E_0E_0^{*}. \tag{3.33}$$

The PC-detection is sensitive only to the electric field polarized parallel to the dipole antenna orientation. Therefore, we can selectively detect the THz component in the horizontal direction. Fig. 3.15 shows some representative waveforms measured with varying the polarization orientation of the incoming light. As expected at zero and 90 degrees, the THz signal is very weak but we have strong signal at $\pm 45°$. Fig. 3.16 shows the peak THz signal measured while changing the polarization angle. We can clearly see the $\sin 2\theta$ dependence.

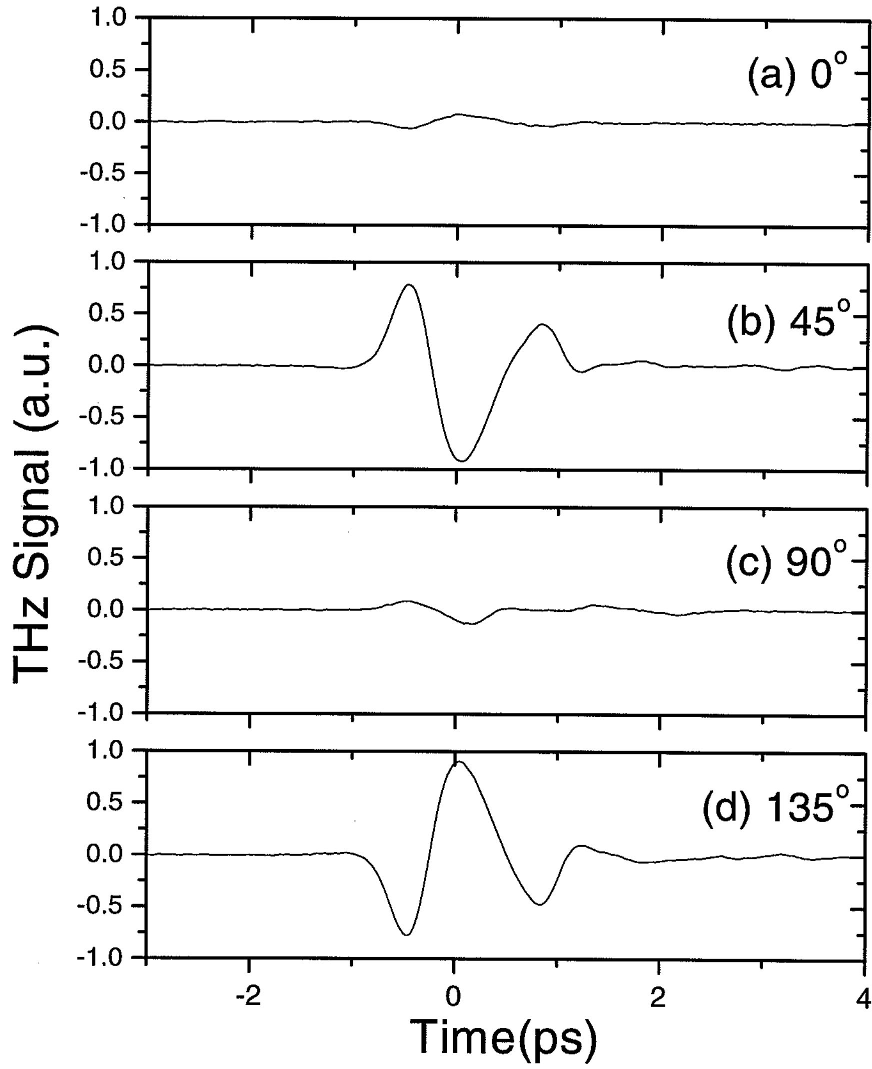

Fig. 3.15. THz waveform obtained from ZnTe emitter by varying the crystal orientation while fixing the polarization of the excitation pulse.

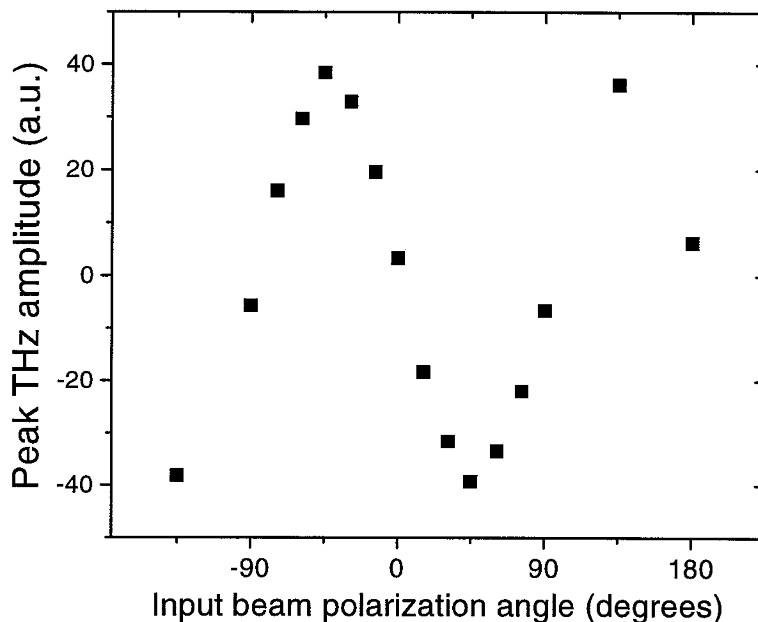

Fig. 3.16. Peak amplitude of the THz waveform obtained from a ZnTe emitter by varying the crystal orientation while fixing the polarization of the excitation pulse.

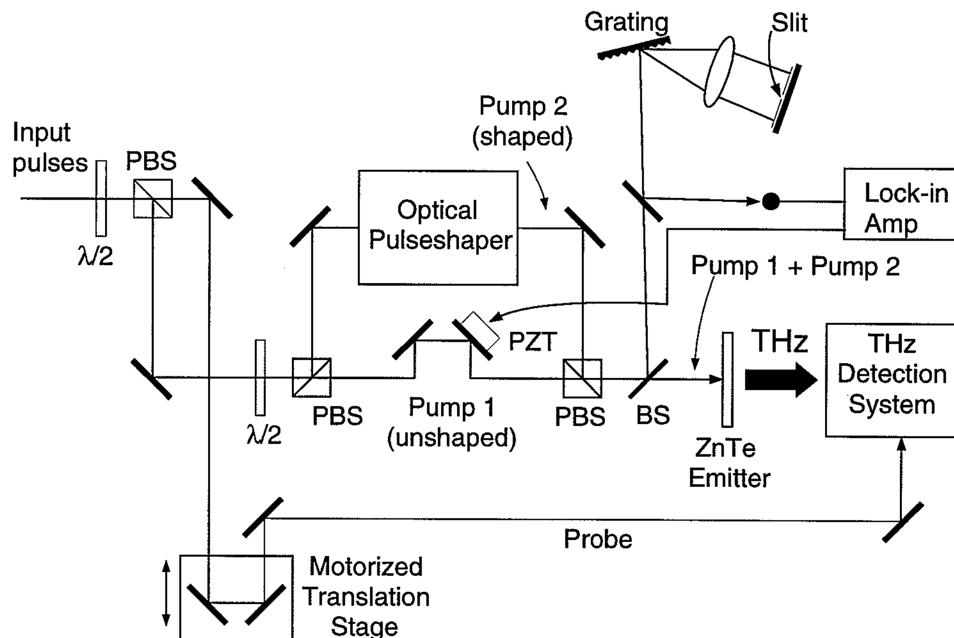

Fig. 3.17. The schematic of the setup for THz pulse-shaping using difference frequency generation. Pump 1 was vertically polarized and pump 2 was horizontally polarized. PBS: polarization beam splitter, $\lambda/2$: half-wave plate

After we have made sure that we could get THz generation through the cross-term, we setup the experiment employing two separate excitation beams for each polarization. Fig. 3.17 shows the setup. Ideally, we should have two pulse-shapers to independently shape pulses in each polarization. But as a preliminary work, we choose to have only one shaper. The beam through the shaper is horizontally polarized and the beam which does not pass through the shaper is vertically polarized. Since the THz generation scheme is sensitive to the relative phase difference between the two excitation beams of different polarization, the phase should be stabilized with interferometric precision. This phase stabilization was implemented using a piezo-electric modulator. Similar technique has been successfully applied to the relative phase stabilization of two ultrashort pulses [82, 99]. A half-wave plate and a polarizer were used to make the two beams of different polarization interfere each other. The spectral intensity at the specified wavelength is selected by a grating and fed into a photo diode which, in turn, feeds a lock-in amplifier. The piezo-electric modulator is stabilized from the signal from the lock-in amplifier which, in turn, is produced by small dithering of the piezo-electric modulator. At the present time, the stabilization at zero-delay has been accomplished. For this, no grating was used since at zero time delay no frequency domain fringe pattern is developed. Instead, we used a power meter to measure the optical power of the two interfering beam. Depending on the reference signal phase of the lock-in, the optical power was stabilized either at minimum or maximum value. However, the contrast ratio was not very high. This is most likely from the imperfect alignment of the optical pulse-shaper.

As a first step of THz generation using two excitation beams, we used unshaped beams for both polarization excitations. This particular experiment was performed without active phase stabilization. Fig. 3.18 shows the THz radiation excited by (a) both vertical and horizontal polarization pulses (b) only vertical polarization pulse and (c) only horizontal polarization pulse. When the alignment is perfect, we should observe the THz signal only for the case (a). The horizontally polarized pulse generates a THz pulse through its own self term, but our detection scheme is not sensitive to the vertical polarization of the self-term. The vertically polarized pulse itself cannot generate THz. In the Fig. 3.18, we see that as expected we get strongest THz radiation when both beams are present. Still there is small THz signal in (b) and (c). They seem to be mainly due to the not-perfect directional alignment of the system. In order to get good extinction ratio, the ZnTe emitter direction, the two pump polarizations should be exactly matched to either parallel or orthogonal

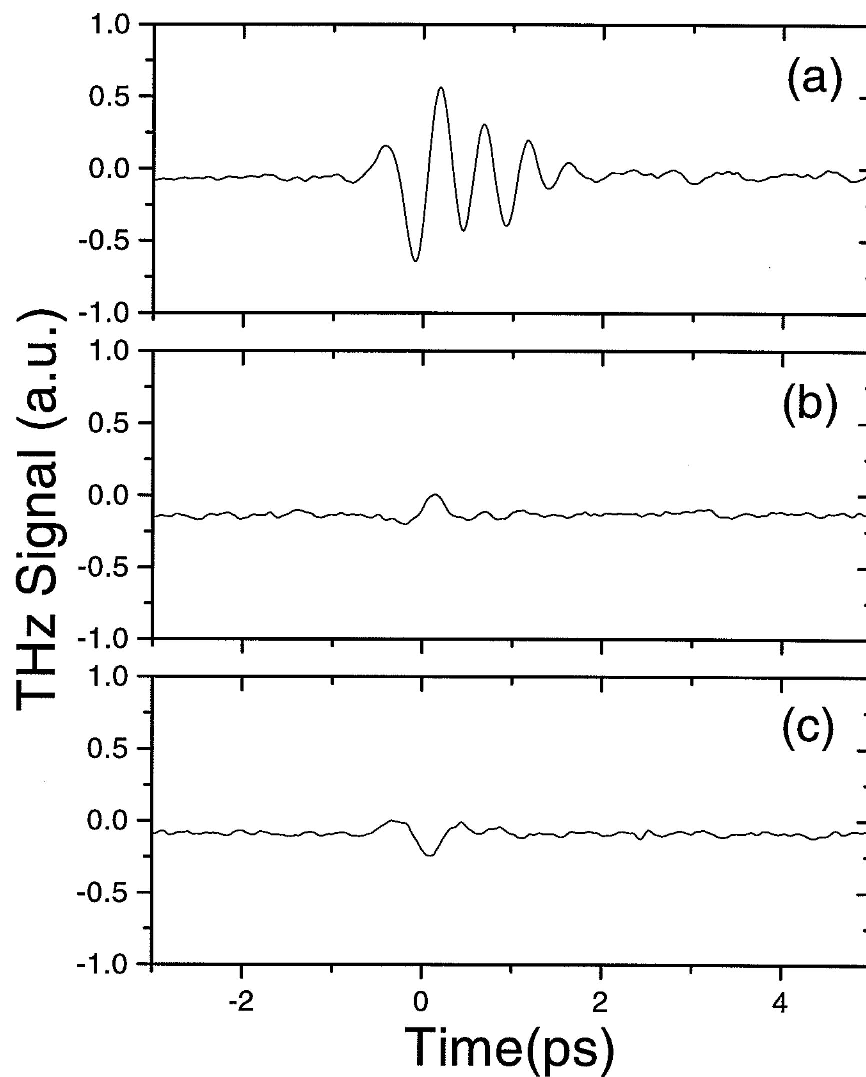

Fig. 3.18. THz radiation generated by difference frequency generation in ZnTe crystal. (a) both vertical and horizontal polarization excitation beams present (b) only vertical polarization excitation beam present (c) only horizontal polarization excitation beam present.

direction of PC-dipole antenna. Also, the finite polarization sensitivity of the dipole antenna itself can contribute to the signal in (b) and (c).

3.7 Conclusion

In this chapter, we demonstrated the shaping of the THz radiation via optical pulse-shaping of the excitation pulse. By shaping the intensity profile of the optical pulses which excite the PC-antennas, we could generate a number of THz waveforms including binary bit streams, and narrow-band radiation. This technique is very versatile and has very low loss compared to other techniques. We also discussed the limitation of this pulse-shaping using a PC-antenna which is driven by the intensity of the optical pulses. To overcome this, we proposed a THz pulse-shaping scheme which is sensitive to the electric field of the excitation pulses, and some preliminary results were presented.

4. SATURATION AVOIDANCE AND THE HIGH-POWER NARROW-BAND THZ GENERATION USING MULTIPLE-PULSE OPTICAL EXCITATION OF PHOTOCONDUCTIVE ANTENNAS

4.1 Introduction

The THz radiation has been an issue of intense research since the 80's. From that time, coherent THz generation has been generated using femtosecond lasers illuminating various emitters, including externally biased photoconductive (PC) antennas, semiconductors biased by surface built-in field and nonlinear crystals. Until now the strongest radiation power below 2 THz frequency range has been generated by externally biased PC-antennas [100, 101, 102]. High power THz radiation can be desirable for a number of applications both in science and engineering. Therefore, a lot of effort has been directed to obtain stronger radiation and to investigate the source of the limitation of the available THz radiation generated from PC-antennas [100, 101, 102, 103, 104, 105, 106, 107].

In Chap. 3, we generated a number of THz radiation waveforms using optical pulseshaping. Among the THz waveforms generated was tunable narrow-band THz radiation. These tunable narrow-band radiations were generated by exciting a PC-emitter with pulse trains which have various inter-pulse spacings. By varying the separation between the pulses in the train we could tune the center frequency of the narrow-band THz radiation. These narrow-band THz radiation can be applied to communications or spectroscopy where narrow-band excitation and tunability is desirable. For nonlinear spectroscopy, very high power radiation is also desirable. An application of this narrow-band THz generation is the high power narrow-band THz generation avoiding the saturation of the PC-emitter.

When the PC-emitter is excited by a very high fluence optical pulse, the output power of the resulting THz radiation does not grow proportionally to the excitation fluence due to the saturation of the emitter. In this chapter, we demonstrate that by using multiple-pulse excitation of the PC-emitter, we can avoid the saturation of the

THz emitter and can extract more THz power in the narrow-band than when we use single-pulse excitation.

This saturation avoidance and the high power generation is first demonstrated using small dipole antenna excited by unamplified pulses [91, 108]. Then this work is extended to large-aperture antennas excited by amplified pulses [109]. In this work, we developed large-aperture PC-antennas for narrow-band THz radiation, which can be used with amplified excitation pulses of fluence of up to 1 mJ. We could reduce the saturation effect and enhance the peak power spectral density of emitted THz radiation by using multiple-pulse excitation and the PC-emitter fabricated on low temperature grown GaAs (LT-GaAs) [54] photoconductor whose carrier lifetime is shorter than the pulse spacing. We find that short carrier lifetime of the photoconductor is very important, because of the near-field nature of the field-screening of the biased emitter. Also we find that the thickness of the short carrier lifetime photoconductor is important when we design emitters for use with very high fluence excitation. When the thin film photoconductor is excited by high fluence optical pulse, a portion of light penetrate into the substrate which has long carrier lifetime which in turn degrades the performance of the PC-emitter.

This chapter is organized as follows. In Sec. 4.2, we review the theory of the saturation of PC-antennas. In Sec. 4.3, we present the high power narrow-band THz generation using dipole antenna, where we demonstrate for the first time that saturation effect could be reduced by multiple-pulse excitation where individual pulses have small peak power. Sec. 4.4 and 4.5 covers the extension of the above work presented in Sec. 4.3 to the case where we use large-aperture PC antenna with amplified high fluence excitation pulses. In Sec. 4.4, we discuss some considerations which are important in the design of large-aperture PC-antennas and the modeling procedure we developed to predict the THz radiation from the antennas. In Sec. 4.5, experimental results will be presented.

The saturation avoidance and high power narrow-band THz generation using dipole antenna with unamplified excitation was performed in collaboration with Dr. Yongqian Liu. The extension of the above work to large-aperture emitter excited by amplified pulses was performed in collaboration with Dr. Tony Taylor, Dr. Craig Siders, Dr, Jennifer Siders at Los Alamos National Laboratory.

4.2 The theory of the saturation of PC-antennas

4.2.1 The saturation theory

In this section, we review the theory of the PC-antenna and point out some implications of this. When a PC-antenna is excited by strong optical pulses, the THz output strength is saturated. This saturation mechanism comes from the screening of the externally applied bias field. The origins of this screening are known to be the radiation field screening [100] and the space-charge screening [104, 110].

In the radiation field screening, the near-field at the surface generated by the transient current cancels out a portion of the bias field. For the case of large-aperture antenna, where the aperture size is larger than the center-wavelength of the emitted THz radiation, the radiation field screening effect can be derived by simple electromagnetic boundary conditions [100]. The electric and magnetic field around the antenna can be divided into stationary ones from the applied bias (E_b,H_b) and transient ones from the induced current from optical excitation (E_r,H_r). Fig. 4.1 shows a large aperture PC-emitter. Fig. 4.1 depicts the quantities which is relevant to the theory. We use ($E_{r,1}, H_{r,1}$) and ($E_{r,2}, H_{r,2}$) to designate the transient field inside the semiconductor and the free space. Since there is no current without excitation, only electric field E_b is present ($H_b = 0$) before the arrival of the excitation pulses. When the photoconductor is excited by light, the photo-generated carriers flow in the bias field generating surface current J_s. When there is surface current density $J_s(t)$, following boundary condition of Eqs. 4.1 and 4.2 hold.

$$E_{r,1}(t) = E_{r,2}(t) \equiv E_r(t) \quad (4.1)$$

$$J_s(t) = H_{r,2}(t) - H_{r,1}(t) \quad (4.2)$$

Also, when the aperture of the antenna is large compared to the wavelength of the radiation, $H_{r,2}(t)$ and $H_{r,1}(t)$ can be related to $E_{r,2}(t)$ and $E_{r,1}(t)$ by Eq. 4.3 and 4.4, respectively.

$$H_{r,1}(t) = \frac{\sqrt{\epsilon_s}}{\eta_0} E_{r,1}(t) \quad (4.3)$$

$$H_{r,2}(t) = \frac{1}{\eta_0} E_{r,2}(t) \quad (4.4)$$

where η_0 is the intrinsic impedance of free space and ϵ_s is the relative dielectric constant of the photoconductor. By combining Eqs. 4.1~4.4, we obtain Eq. 4.5 which

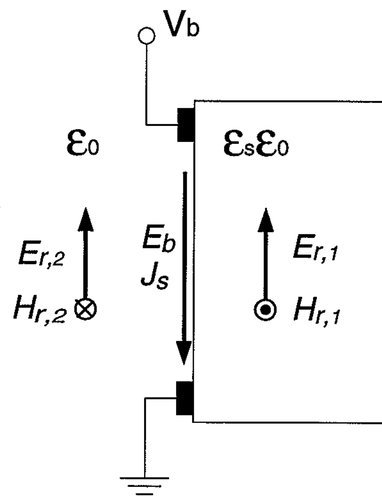

Fig. 4.1. The photoconductive biased emitter. E_b: biased electric field. V_b: applied voltage, J_s: induced current, and $E_{r,1}$, $H_{r,1}$: radiated electric and magnetic field into the semiconductor. $E_{r,2}$, $H_{r,2}$: radiated electric and magnetic field into the free space.

relate the surface current to the radiation electric field.

$$E_r(t) = -\frac{\eta_0}{1+\sqrt{\epsilon_s}} J_s(t) \tag{4.5}$$

Eq. 4.5 tells us that the surface electric field component developed by surface current is opposite to the direction of J_s. By the way, J_s can be expressed using Ohm's law,

$$J_s(t) = \sigma(t)\,(E_b(t) + E_r(t)), \tag{4.6}$$

where $\sigma(t)$ is the surface conductivity of the emitting antenna. Combining Eqs. 4.5 and 4.6, we get Eq. 4.7 for surface current $J_s(t)$.

$$J_s(t) = \frac{\sigma(t) E_b}{1 + \frac{\sigma(t)\eta_0}{1+\sqrt{\epsilon_s}}} \tag{4.7}$$

It is evident from Eq. 4.7 that the magnitude of the induced current is saturated when $\sigma(t)\eta_0/(1+\sqrt{\epsilon_s}) \geq 1$. (i.e. when excited by large fluence pulses.) The far-field radiation $E_{rad}(t)$ from current distribution $J_s(t)$ on the propagating axis of the radiation can be expressed by [111]

$$E_{rad}(t) \cong -\frac{A}{4\pi\epsilon_0 c^2 r}\frac{dJ_s(t)}{dt}, \tag{4.8}$$

where A is the area of the emitter carrying the current distribution. When comparing Eq. 4.5 and Eq. 4.8, we observe a difference in the characteristic of the far-field and the near-field. The far-field is proportional to the time-derivative of the current, while the near-field is directly proportional to the current. The saturation behavior of the photoconductive emitter is governed by the near-field as shown in Eq. 4.7. Because the near-field is proportional to the surface current, not to the time-derivative of it, the saturation effect persists as long as there is current. The difference between these two is clear when a long carrier lifetime photoconductor is considered. When the photoconductor is illuminated by a short optical pulse, a current surge is generated which leads to THz radiation. If the carrier lifetime is long, current keeps flowing long after the excitation pulse, when the far-field radiation, which is proportional to the time derivative of the current, is not present anymore. If another pulse arrives before the current dies out, and excite the emitter, a new THz pulse will be generated, but this time the background current which is already present, may affect the THz generation.

For small dipole case, the above derivation of radiation screening should be modified. Yet no theory of radiation screening of small dipole has been developed. The

difficult part is that we can no longer assume that the radiated wave is a plane wave. Then Eqs. 4.3 and 4.4 do not hold. Also in that case, Eqs. 4.1 and 4.2 become ones govern only the transverse part of the field of the radiation which can no longer be approximated as plane wave. Nevertheless, we expect that the radiation screening plays a role in the THz generation using small dipole with an adjustment of saturation fluence compared to large aperture emitters.

The space-charge screening arises from the separation of the photo-generated electrons and holes in the bias electric field. When the electrons and holes drift in the opposite direction, regions of net positive and negative space charge develop. The electric field induced by this space-charge is in the opposite direction to the bias field and screen the bias field. This space-screening can be important for small dipole antenna [110, 104], but for large-aperture antenna, radiation screening is the major source of the saturation [112].

4.2.2 Power and amplitude scaling relations of the THz radiation excited multiple-pulse sequence

In this section we examine the power and amplitude scaling relations of the THz radiation relevant to our work of multiple-pulse excitation. First we examine the case when the THz emitter operates in a linear regime. Let's say that the optical excitation $I_1(t)$ generates THz radiation $E_1(t)$. Then the optical excitation is split without loss into N-pulses of equal total fluence to the one pulse case with inter-pulse separation T as in Eq. 4.9.

$$I_N(t) = \frac{1}{N}\sum_{n=0}^{N-1} I_1(t-nT) \tag{4.9}$$

Since the emitter is in the linear regime, the THz radiation from the N-pulse excitation can be calculated as a linear combination of single pulse response as in Eq. 4.10,

$$E_N(t) = \frac{1}{N}\sum_{n=0}^{N-1} E_1(t-nT). \tag{4.10}$$

The Fourier spectrum of $E_N(t)$ is given in Eq. 4.14,

$$\begin{aligned} S_N(\omega) &= \int dt\, e^{-i\omega t} E_N(t) & (4.11)\\ &= \frac{1}{N}\sum_{n=0}^{N-1} e^{i\omega nT}\int dt\, e^{-i\omega t}E_1(t) & (4.12)\\ &= \frac{1}{N}\frac{1-e^{Ni\omega T}}{1-e^{i\omega T}}S_1(\omega) & (4.13)\end{aligned}$$

$$= \exp[\frac{(N-1)i\omega T}{2}]\frac{\text{sinc}(N\omega T/2\pi)}{\text{sinc}(\omega T/2\pi)}S_1(\omega) \quad (4.14)$$

,where $S_1(\omega) = \int dt\, e^{-i\omega t} E_1(t)$ is the Fourier transform of the THz pulse from single-pulse excitation. This is the well-known linear theory of Fourier transform. We now have the multi-pulse THz spectrum which is represented by the multiplication of the single pulse THz spectrum and the interference term. As the frequency ω approaches the multiples of the repetition rate of the pulse train, $\omega \to 2\pi m/T$, where m is an integer, the interference term approaches 1 as given in Eq. 4.15.

$$\lim_{\omega \to 2\pi m/T} \frac{1}{N}\frac{1-e^{Ni\omega T}}{1-e^{i\omega T}} \to 1. \quad (4.15)$$

Therefore, we know that when the emitter operates in the linear regime, multiple-pulse excitation generates the same peak spectral amplitude as the single pulse excitation at the frequency of $\omega = 2\pi m/T$. Therefore, we do not have any gain in terms of the spectral amplitude when we excite the linear emitter with multiple pulses of equal integrated fluence as the single pulse. Still, the spectrum of the multiple-pulse excited THz becomes narrower as the number of pulse is increased. Therefore, if the purpose of the multiple-pulse excitation is frequency selection, we can achieve this as demonstrated in [91, 108].

Next, let's consider the case when the emitter is completely saturated both by a single pulse of $I_1(t)$ and by individual pulses $I_1(t)/N$ of the N-pulse train. Here, we consider the ideal situation where the emitter recovers from the saturation very rapidly compared to the inter-pulse spacing of the multiple-pulse train. Again, let's say $E_1(t)$ is the THz radiation excited by $I_1(t)$. Since the emitter is completely saturated, $I_1(t)$ and $I_1(t)/N$ should generate roughly the same THz radiation. Then, the THz radiation from multiple-pulse excitation is represented by

$$E_N(t) = \sum_{n=0}^{N-1} E_1(t - nT), \quad (4.16)$$

and the Fourier spectrum $S_N(\omega)$ is given as

$$S_N(\omega) = \frac{1-e^{Ni\omega T}}{1-e^{i\omega T}}S_1(\omega), \quad (4.17)$$

Again, $S_1(\omega)$ is the Fourier transform the THz by single pulse excitation. Now, at frequency $\omega = 2\pi m/T$, where m is an integer, the spectral amplitude of S_N is N times larger than that of S_1; i.e., $S_N(\omega = 2\pi m/T) = N \times S_1(\omega = 2\pi m/T)$. This

translates into N^2 enhancement in the peak power spectral density of the THz radiation generated by N-pulse excitation illuminating a completely saturated emitter. The total THz power around $\omega = 2\pi m/T$ is proportional to N since the spectral narrowing partially compensate N^2 enhancement in the power density.

For cases when there is partial saturation in the THz output for single pulse excitation , but still very fast inter-pulse recovery,

$$E_N(t) = \beta \sum_{n=0}^{N-1} E_1(t - nT) \tag{4.18}$$

where $1/N < \beta < 1$. Then, there is still enhancement—but reduced—compared to complete saturation.

4.3 The avoidance of saturation of small dipole antenna using multiple pulse sequence excitation

In this section, using a dipole PC-emitter, we demonstrate for the first time that the power spectral density at the peak of the narrow-band THz spectrum can be significantly enhanced by the use of multiple-pulse sequence excitation. Our experimental setup is similar to the one described in the Chap. 3 for the THz pulseshaping [Fig. 3.6]. A Ti:Sapphire oscillator produced ~100 fs input pulses at a repetition rate of 80 MHz centered around a wavelength of 800 nm. These input pulses passed through a grating-and-lens optical pulse-shaper. The phase-only M-sequence mask fabricated on fused silica was used in the Fourier plane of the pulse-shaper to tailor the optical frequency spectrum. The excitation pulse was focused to an ~10 μm spot on the transmitting antenna. The antenna, mounted on a Si hyper-hemispherical substrate lens, was a dc-biased PC dipole antenna fabricated on low-temperature-grown GaAs (LT-GaAs) with a subpicosecond lifetime. In our experiment, a 25 V bias was applied across a 5 μm photoconductive gap. The THz radiation propagated in free space and was focused by another Si hyper-hemispherical lens onto a similar PC dipole antenna, which acted as the receiver. The receiver was placed ~10 cm away from the transmitter. A portion (~ 40 mW) of a split beam from the original pulse was used as a trigger to sample the THz radiation sensed by the detector. The current signal, proportional to the radiated field, was amplified by a current preamplifier and recorded by a lock-in amplifier. We mapped out the THz radiation field as a function of time by scanning the delay between the excitation pulse and the sampling pulse.

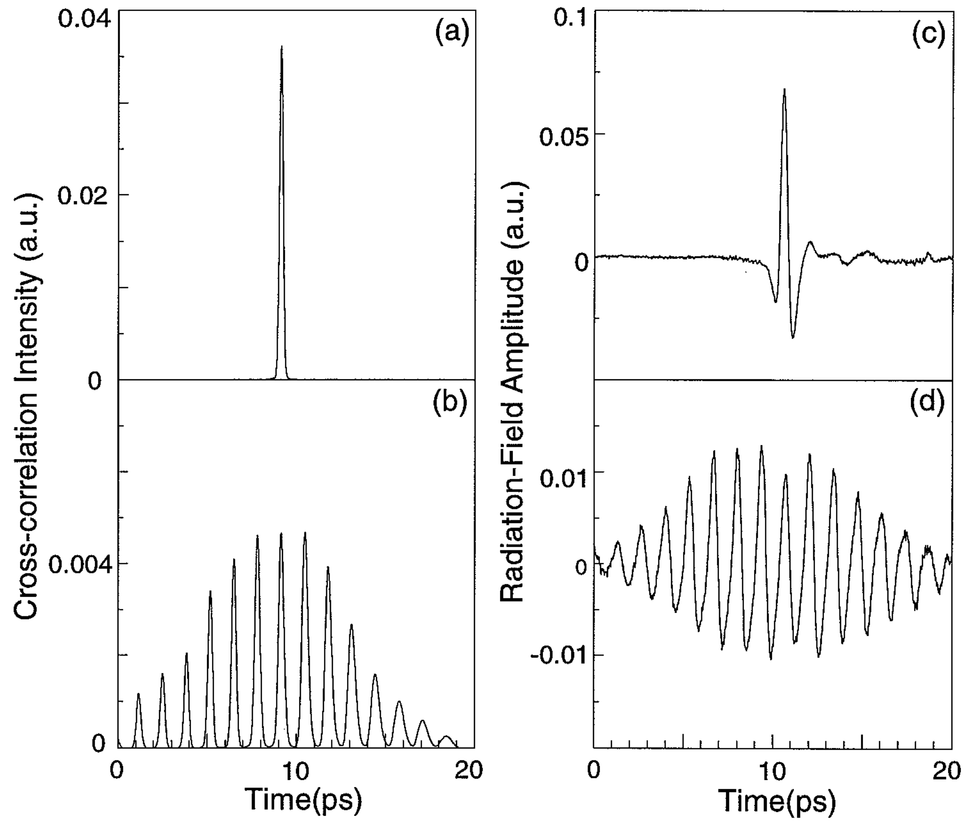

Fig. 4.2. Intensity cross-correlation measurement of the input optical excitation pulse: (a) single pulse, (b) multiple pulses, and time-domain waveforms for the THz radiation using (c) single-optical pulse and (d) multiple-optical-pulse excitation

Figs. 4.2 (a) and (b) show intensity cross-correlation measurements of the optical excitation pulses made with a single unshaped pulse split off from the laser as a reference. Cross-correlation measurements are shown both for single excitation pulses obtained by removing the mask pattern from the pulse-shaper [Fig. 4.2 (a)] and for a 750 GHz multiple pulse sequence [Fig. 4.2 (b)]. Figs. 4.2 (c) and (d) show measurements of the THz radiation generated by the single-pulse [Fig. 4.2 (c)] and the multiple-pulse sequences [Fig. 4.2 (d)] at a fixed 44 mW average pump power. Excitation with the pulse sequence resulted in a quasi-sinusoidal THz waveform with a center frequency equal to the repetition rate of the optical pulse train. The multiple-pulse sequence functions as an active filter to select a particular THz radiation frequency.

We showed in Sec. 4.2.2 that if the photoconductive antenna remains in the linear response regime, the peak THz spectral amplitude at frequency ν_0 is the same as the THz spectral amplitude at frequency ν_0 that results from single-pulse excitation, provided that the overall optical fluence is unchanged. Thus, even though use of a multiple-pulse sequence diminishes the peak optical intensity and the peak THz field as viewed in the time domain, the multiple-pulse excitation leads to the same THz spectral amplitude at the selected frequency.

Actually, this is the case in our experiments at low optical powers ($P < 12\,\mathrm{mW}$), which is shown in Fig. 4.3 (a). However, for higher optical power a dramatic difference between single-pulse and multiple-pulse excitation is observed. Fig. 4.3 (b) shows the FFT power spectrum for a high fluence excitation case of an average optical power of 44 mW. The peak THz spectral amplitude observed at the first-harmonic frequency ν_0=750 GHz resulting from multiple-pulse excitation is increased by a factor of 1.84 compared to that for single-pulse excitation. This corresponds to a factor-of 3.4 enhancement in the power spectral density. This enhancement of narrow-band THz generation by use of multiple-pulse optical excitation arises because of the avoidance of saturation mechanisms that limit the THz amplitude in the case of high-power single-optical pulse excitation.

Fig. 4.4 is a plot representing the THz spectral amplitude at $\nu_0 = 750\,\mathrm{GHz}$ as a function of average optical power for both single- and multiple-pulse excitation. The filled symbols in the plot are derived directly from the FFT of the measured THz time-domain waveforms; we obtained the open symbols simply by recording the peak amplitude of the detected time-domain THz waveforms versus power and then multiplying by the appropriate scale factors to convert from peak time-domain amplitude to spectral amplitude at ν_0. We determined the scale factor by comparing

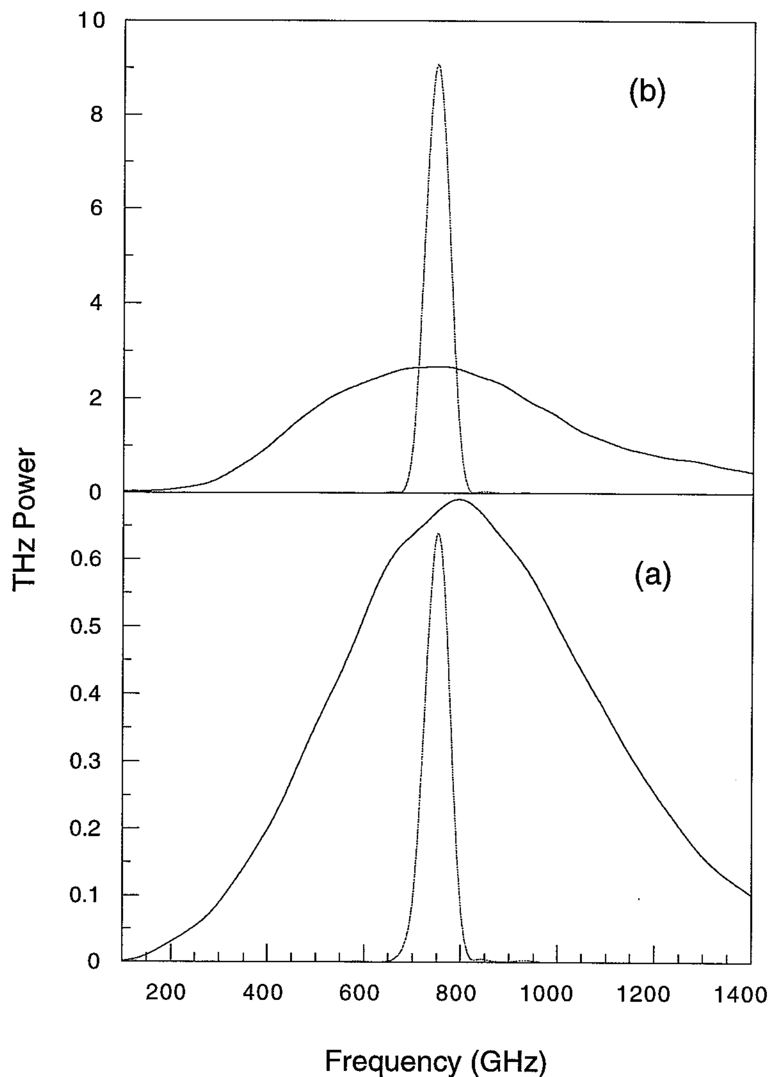

Fig. 4.3. Fourier transformed power spectrums of the THz radiations from broad-band single pulse excitation and narrow-band multiple pulse excitation at an average power of (a) $P \sim 11\,\mathrm{mW}$, and (b) $P \sim 44\,\mathrm{mW}$ showing the enhancement of radiation by multiple pulse excitation at high powers.

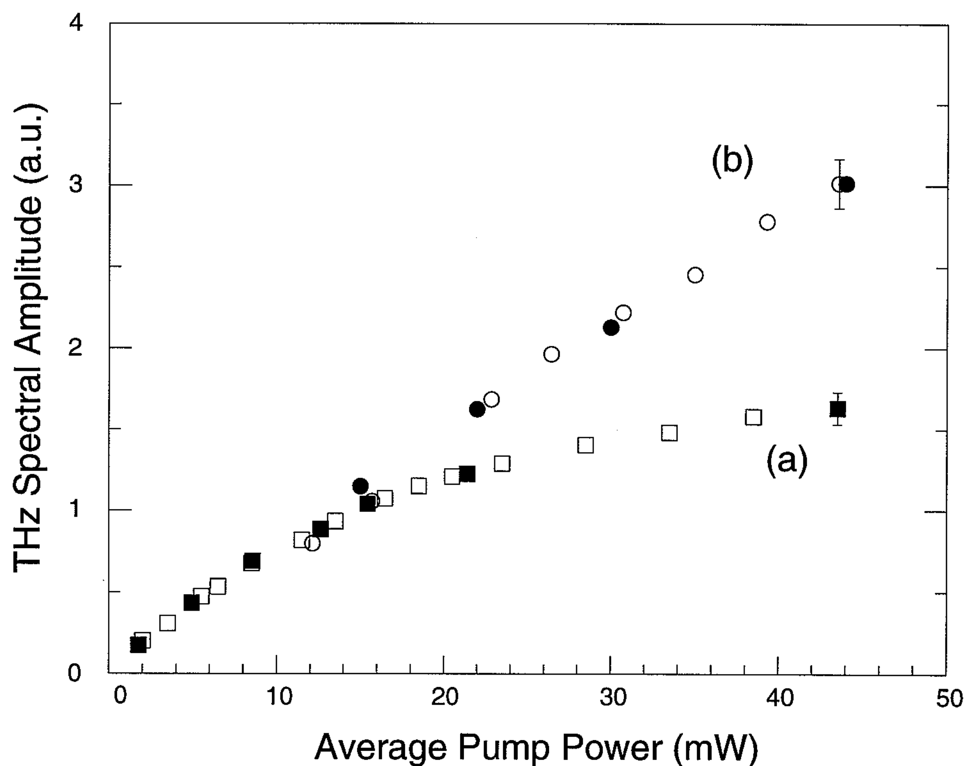

Fig. 4.4. Spectral amplitude of the THz radiation as a function of the average excitation powers for the (a) single- and (b) multiple-optical pulse excitations. Filled symbols represent peak spectral amplitudes obtained directly from FFT's. Open symbols represent peak amplitudes in the time domain scaled to the spectral amplitudes at fundamental frequency ν_0 by multiplication by the appropriate scale factors. Also shown are typical error bars.

the THz time-domain data and their Fourier transforms for 44 mW average pump power for both single- and multiple-pulse excitation. The same scale factors (one for single pulses and one for multiple pulses) were then applied to generate the amplitude represented by all the open symbols. Both single- and multiple-pulse plots show a linear dependence on optical power for average powers below ~12 mW. At higher powers, however, the THz amplitude for single-pulse excitation saturates, whereas the THz signal obtained by multiple-pulse excitation remains linear with optical power. The avoidance of saturation in the latter case arises because the peak optical intensity of the multiple-pulse sequence is reduced nearly tenfold compared with that of the original single pulse, thus scaling multiple-pulse excitation into the linear response regime.

Saturation studies of dipole antennas and related structures have focused on space-charge screening, which has led to significant saturation on an ultrafast time scale at carrier densities in the $10^{17} \sim 10^{18}$-cm^{-3} range [110, 104]. In our highest-power (44 mW) single-pulse experiments the estimated carrier density is 3×10^{18} cm^{-3}. This suggests that space-charge screening may play a role in our single-pulse experiments, even though the magnitude of these effects will depend on the precise device geometry. With multiple-pulse excitation each individual pulse generates substantially fewer electron-hole pairs. Provided that the space-charge relaxation time is faster than the pulse repetition period (as is likely given the subpicosecond carrier lifetime of our LT-GaAs transmitter), screening effects that are due to the space-charge field are strongly reduced with multiple pulses.

In the case of large-aperture antennas, attention has focused on screening of the bias field by the radiation field. Our dipole experiments use fluence as high as 700 μJ/cm^2, well above the saturation fluence reported for large-aperture antennas [100, 111]. Therefore, it is most likely that screening by the radiation field may be an important effect in our experiments, even though the large-aperture results do not directly apply to our setup, for which the dipole size is much less than the average THz wavelength. In the experiments using multiple-pulse excitation the saturation is linked to peak optical power (or fluence per individual pulses). Spreading the optical excitation into multiple pulses, resulting in a reduced peak radiation field, greatly extends the linear regime as long as the lifetime of the photo-generated carriers are shorter than the pulse spacing. We do not see any sign of saturation for the multiple pulse excitation case in the fluence range used in the experiments. Our current

research does not distinguish between space-charge field and radiation field screening mechanisms. However, multiple excitation appears capable of alleviating both mechanism.

In conclusion, by using multiple pulse sequence optical excitation which has reduced peak power, we could avoid the saturation of the PC dipole antenna and enhance the THz power spectral density at the repetition frequency of the pulse train.

4.4 Design of the large-aperture PC-antenna for high power narrow-band THz generation

4.4.1 Some design considerations in developing the large-aperture antenna for use with multiple-pulse excitation

When designing THz emitters which would overcome saturation and generate strong narrow-band radiation, we should consider several things. Firstly, from the near-field nature of the screening, we know that the lifetime of the carrier should be short compared to the inter-pulse spacing of the excitation pulse train. Assuming exponential decay, the inter-pulse spacing should be larger than the lifetime by factor of 2∼3 in order to reduce the carrier population to below 10% of peak value. This means that in order to have narrow-band radiation around 1 THz, where inter-pulse spacing is 1 ps, carrier lifetime less than 300 fs is required. In this research, experiments were performed to generate 300 GHz radiations. Another important factor is the thickness of the photoconductive layer. Most of the time, fast photoconductive layer is epitaxially grown on another semiconductor substrate of long carrier lifetime (typically > 100 ps). Therefore, if the excitation pulse penetrates into the substrate, very slowly decaying populations of electrons and holes are generated and the performance of the emitter is degraded. For GaAs epitaxial layer, the absorption coefficient at 800 nm wavelength $\alpha^{-1} \sim 1\,\mu$m [113]. Therefore, if the thickness of the epitaxial layer is 1 μm, about 30% of the light is absorbed in the substrate. In order to reduce substrate absorption below 5%, about 3 μm of the epitaxial thickness is required.

4.4.2 Simulation of THz radiation from large-aperture PC-antenna subject to saturation

We performed numerical calculations to predict the saturation behavior of the emitters more quantitatively. We calculated far-field radiation from the large-aperture PC-antenna taking into account the saturation. In this calculation, only the radiation

screening was included. The space-charge screening effect was not considered since it has negligible effect on the large-aperture antenna [112]. To account for the absorption of the light in the substrate, we used two layers of electrons which correspond to the electrons in the epitaxial thin-film and the substrate, respectively For SI-GaAs emitter, the two layers have same the mobility and the same recombination time.

We start with the electron concentration in the epitaxial layer. The electron concentration $n(x,t)$ in the epitaxial layer can be calculated from Eq. 4.19.

$$\frac{\partial n(x,t)}{\partial t} = -\frac{(1-R)}{h\nu}\frac{\partial I_{opt}(x,t)}{\partial x} - \frac{n(x,t)}{\tau_{r,epi}} \tag{4.19}$$

,where $\tau_{r,epi}$ is the recombination/trap lifetime in the epitaxial layer, $I_{opt}(x,t)$ is the excitation pulse intensity profile, R is the reflection coefficient at the photoconductor surface, x is the distance from the semiconductor surface and $h\nu$ is the excitation photon energy. In Eqs. 4.19, the first term on the right hand side represents the absorption of the light which leads to the generation of electrons (and holes). The second term represents the removal of the electrons from the conduction band through recombination or trapping. Let's define the sheet electron concentration in epitaxial layer as

$$n_{epi}(t) \equiv \int_0^l n(x,t)\,dx \tag{4.20}$$

,where l is the thickness of the epitaxial layer. Then, Eq. 4.19 can be integrated to yield,

$$\begin{aligned}\frac{\partial n_{epi}(t)}{\partial t} &= \frac{(1-R)}{h\nu}\{I_{opt}(0,t) - I_{opt}(l,t)\} - \frac{n_{epi}(t)}{\tau_{r,epi}} && (4.21)\\ &= \frac{(1-R)}{h\nu}I_{opt}(0,t)\{1-e^{-\alpha l}\} - \frac{n_{epi}(t)}{\tau_{r,epi}} && (4.22)\end{aligned}$$

In Eq. 4.22, linear absorption of light with absorption coefficient α was used. The sheet electron density in the substrate $n_{sub}(t) \equiv \int_l^\infty n(x,t)\,dx$ can be calculated easily as,

$$\begin{aligned}\frac{\partial n_{sub}(t)}{\partial t} &= \frac{(1-R)}{h\nu}I_{opt}(l,t) - \frac{n_{sub}(t)}{\tau_{r,sub}} && (4.23)\\ &= \frac{(1-R)}{h\nu}I_{opt}(0,t)e^{-\alpha l} - \frac{n_{sub}(t)}{\tau_{r,sub}} && (4.24)\end{aligned}$$

,where $\tau_{r,sub}$ is the recombination/trap lifetime of electrons in the substrate. In Eq. 4.23 and 4.24, we assumed that all the light reach the substrate will be absorbed inside the substrate and generate electrons and holes.

In the above derivation, only linear absorption of excitation light in the semiconductor was considered. The expressions for the more general case of nonlinear absorption (optical bleaching) is derived in the Appendix.

In Eqs. 4.22 and 4.24, the current transport effect was ignored ($\nabla \cdot J = 0$), since this effect is very small compared to the fast decaying term. We can compare the relative size of the current transport term and the decaying term. The current transport term can approximated by $v(n/L)$, where L is the size of the emitter and v is the velocity of electrons, while decaying term is n/τ_r. If we use saturation velocity of GaAs $v = 10^7$ cm/sec and $L = 0.5$ cm and $\tau_r = 1$ ps, $(v/L){:}(1/\tau_r) = 1{:}\ (5 \times 10^4)$. Therefore, the current transport term can be safely ignored for large-aperture antenna calculation.

The surface current density J_s is obtained using Eq. 4.7 with the sheet conductivity given by Eq. 4.25

$$\sigma(t) = e\mu_{epi}n_{epi}(t) + e\mu_{sub}n_{sub}(t) \tag{4.25}$$

,where μ_{epi} and μ_{sub} are time-independent electron mobilities in the epitaxial layer and substrate, respectively. In this formalism, we ignored the hole concentration, due to its low mobility. When we have the surface current $J_s(t)$, we can calculate the far-field radiation $E_{rad}(t)$ using Eq. 4.8.

In order to compare the calculated waveforms with the measured waveforms, we finish the simulation by calculating the waveforms $E_{meas}(t)$ which would be measured from the measurement. For the measurement technique of THz waveform, we choose electro-optic (E-O) sampling [43], because of its large bandwidth. In the calculation of the measured waveforms, we took into account of the effect of probe beam pulsewidth t_{probe}, and the group velocity mismatch of the optical probe beam and the THz beam. These effects are important because of the thick (1 mm) sensor ZnTe crystal used we used. The E-O sampled waveforms were calculated using following equations. The optical probe beam profile with the GVM effect taken into account is given by Eq. 4.26

$$I_p'(t) = \int dt' I_p(t-t')\, \Pi(t_{walkoff} : t') \tag{4.26}$$

,where $I_p(t) = e^{-t^2/t_{probe}^2}$ is the probe beam profile, and $\Pi(t_{walkoff} : t)$ is the unit pulse function given as

$$\Pi(t_{walkoff} : t) = \begin{cases} 1 & , -t_{walkoff}/2 < t < t_{walkoff}/2 \\ 0 & , \text{otherwise} \end{cases} \tag{4.27}$$

Then, the measured THz waveform, $E_{meas}(t)$ can be calculated using the convolution integral of Eq. 4.28

$$E_{meas}(t) = \int dt' E_{rad}(t')\, I'_p(t-t') \tag{4.28}$$

For the all calculations which will be presented in this chapter, $t_{walkoff} = 0.4\,\text{ps}$ and $t_{probe} = 0.2\,\text{ps}$ were used.

4.5 Experimental results of high-power narrow-band THz generation using large-aperture PC-antenna

4.5.1 Experimental Setup

The experimental setup for narrow-band THz generation through multiple-pulse excitation is shown in Fig. 4.5. An amplified Ti:sapphire laser system produces 130 fs, 0.7 mJ pulses at 800 nm with a repetition rate of 1 kHz. Prepulses preceding the main amplified pulse by >1 ns are eliminated by placing a Pockel's cell after the amplifier. Roughly 90% of this beam is input into a novel hyper-Michelson interferometer [114], which is used to produce a train of equal-amplitude pulses separated by 3.3 ps, corresponding to a repetition rate of 300 GHz. Fig. 4.6 shows a version of hyper-Michelson interferometer used in this work, which can generate 2 to 8 pulses. We chose to generate pulse sequences after the amplification of the optical pulses in the regenerative amplifier in order to avoid cross-talk between the adjacent pulses during the amplification [115]. A typical cross-correlation of an 8-pulse optical pulse output from this interferometer with the unshaped reference beam is shown in Fig. 4.7. The optical pulse train is lightly focused to a 4-mm-diameter spot and is incident on a 5-mm-gap photoconductive emitter biased at 3 kV/cm. For the detection of the THz radiation, E-O sampling was used. As a detector a 1 mm thickness <1$\bar{1}$0> ZnTe crystal was used. The THz radiation and a sub-nJ optical probe beam were focused on the ZnTe crystal by the 15 cm off-axis parabolic reflector placed 20 cm from the emitter. The THz electric field is mapped out temporally by scanning the time delay between the probe pulse and the THz pulse train using computer controlled stepper motor stage.

We studied four PC-emitters made on SI-GaAs and LT-GaAs [54]. The photoconductors studied consist of a 1-mm-thick SI-GaAs sample, and three samples with a 2.8-μm-thick LT-GaAs layer grown on a 0.6-mm-thick SI-GaAs substrate. The LT-GaAs layer were grown at 280°C by Prof. Melloch using molecular beam epitaxy and subsequently annealed for 30 seconds at 575°C, 600°C, and 625°C. For the SI-GaAs sample the carrier lifetime is >100 ps, while for the LT-GaAs samples, the lifetimes are

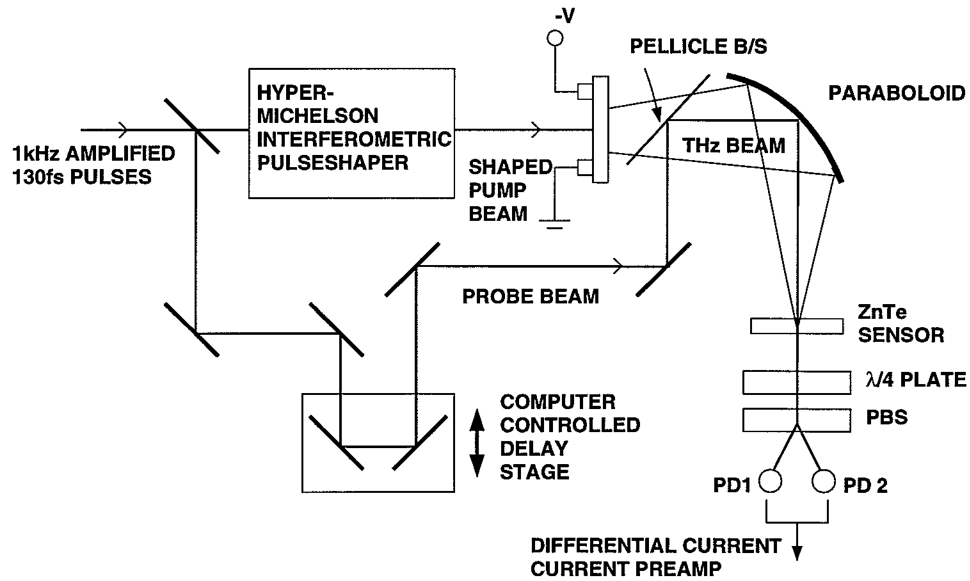

Fig. 4.5. The schematic of the setup for multiple-pulse excitation experimental.

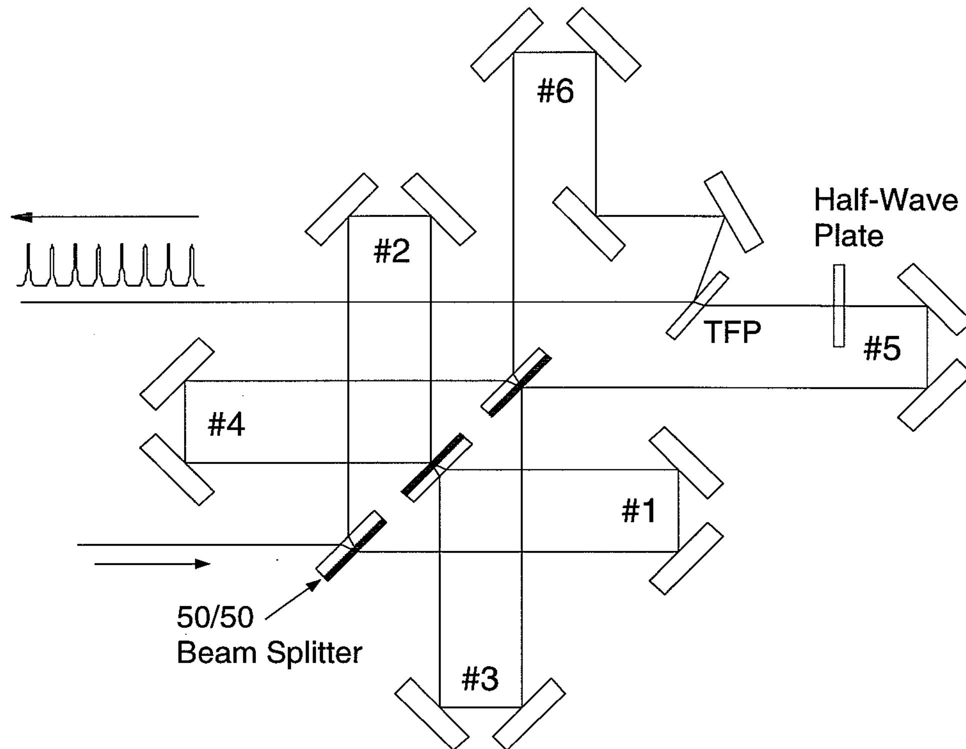

Fig. 4.6. The hyper-Michelson interferometric pulseshaper used in this experiment. The version shown here and used in the experiments can generate pulse sequences of maximum 8 pulse. TFP: thin-film polarizer, #1∼6 are pair of mirrors mounted on the micrometer translational stages.

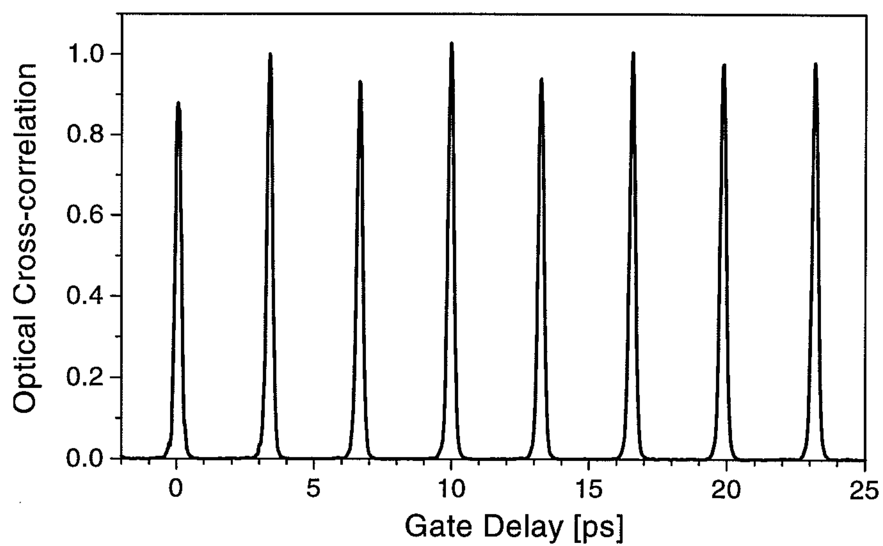

Fig. 4.7. Cross correlation in a 500 μm KDP crystal of the 8-pulse optical pulse output from the hyper-Michelson interferometer with a single optical gate pulse.

all <10 ps. We used very thick layer of LT-GaAs of 2.8 μm to reduce the absorption of the light in the substrate and subsequent contributions of the carriers generated in the substrate to the THz signal.

4.5.2 Single Pulse Excitation

Fig. 4.8 shows the THz waveforms from four emitters excited by single pulses of low optical excitation fluence. The dotted lines are the calculated waveforms. The lifetime of the photo-generated carriers used in the calculation is given in each figure. Because of its very low excitation fluence, the saturation effect is almost negligible. Therefore, carrier lifetimes of the photoconductors were only adjustable parameters in this fit. From three waveforms from LT-GaAs emitters (a-c), we can clearly identify the transition from almost symmetrical bipolar radiation to very asymmetrically bipolar or almost unipolar radiation. This is the direct consequence of the different carrier lifetimes of LT-GaAs layers annealed at different temperatures. The SI-GaAs emitter has almost unipolar waveforms. The slight negative feature in the waveforms from SI-GaAs emitter after the main peak cannot be understood at this time.

In chapter 2, we discussed on the comparison between the THz waveforms measured by E-O and PC-sampling techniques using the same LT-GaAs photoconductors as detectors. There, we used 1.3 ps carrier lifetime as a fitting parameter to model the PC-detector fabricated on the LT-GaAs annealed at 600°C which is substantially different from 0.7 ps used here. This discrepancy might be related to the presence of several different lifetimes in the semiconductor and the possibility of our detecting different lifetimes depending on whether we use the material as emitter or as detector. To independently determine the carrier lifetime, we performed optical pump and probe differential reflection measurements and electrical lifetime measurements using sliding contact excitation [7]. The results of these measurement were summarized in the Table 2.1 in chapter 2. The optical pump and probe measurements at 855 nm and 810 nm measured different lifetimes, and for 600°C annealed LT-GaAs they are close to the value used in the fit here for emitter and the value used before to model the PC-detector, respectively. The sliding contact measurements at 810 nm and 855 nm produced lifetime close to the one measured by optical pump and probe at 810 nm. Despite the range of lifetimes obtained from these different measurements, we can say that the lifetimes used to fit Figs. 4.8 are within the range of values estimated via these techniques. We also note that exact fitting of the single pulse data of Fig. 4.8 is not essential for our multiple pulse experiments discussed below.

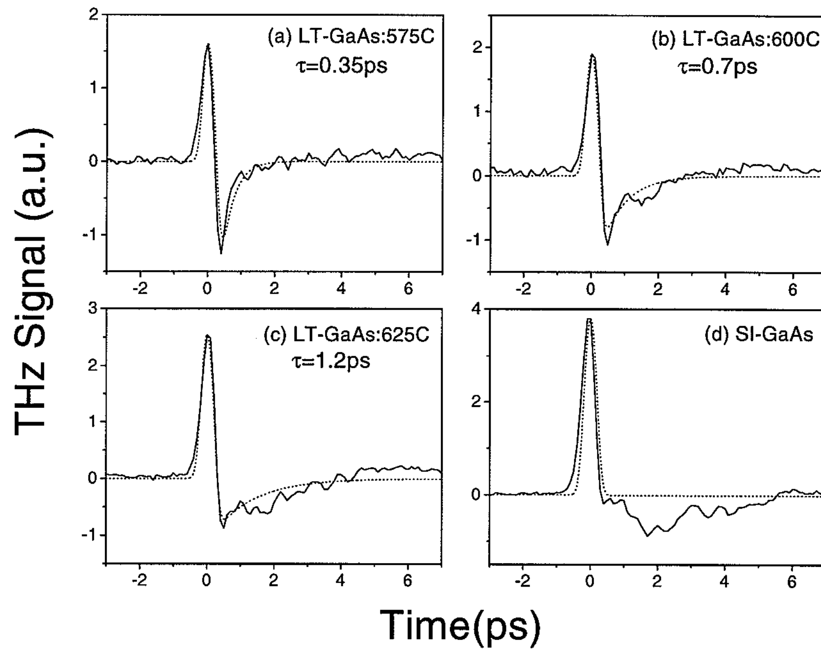

Fig. 4.8. THz radiation waveforms from LT- and SI-GaAs emitters with the excitation by low optical fluence single pulses. The solid-lines represent the measured waveforms and the dashed lines represent the calculated waveforms. Emitter material: (a) LT-GaAs annealed at 575°C (b) LT-GaAs annealed at 600°C (c) LT-GaAs annealed at 625°C (d) SI-GaAs

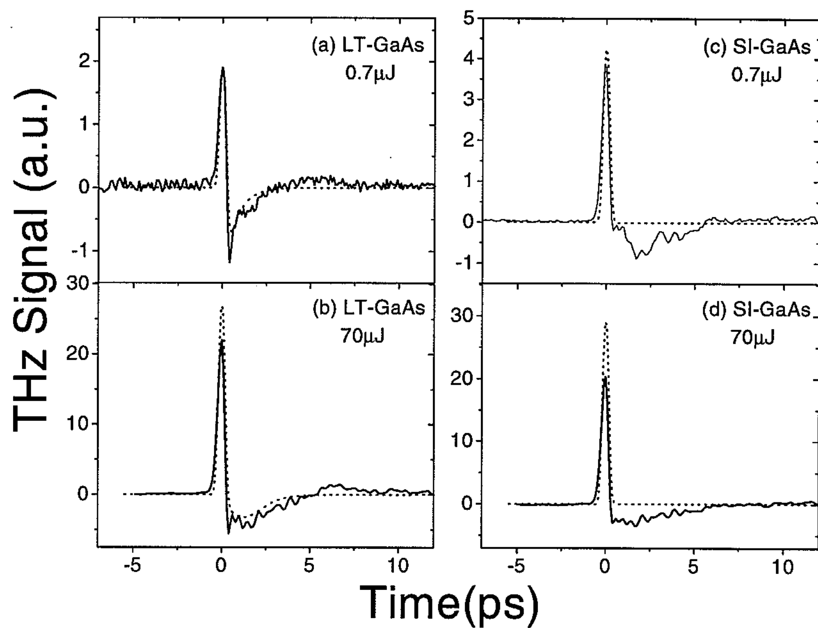

Fig. 4.9. THz radiation waveforms from (a),(b) a LT-GaAs emitter (annealed at 600°C) and (b),(d) a SI-GaAs emitter. The LT-GaAs was annealed at 600°C. The emitters were excited by (a),(c) low fluence (0.7 μJ) or (b),(d) high fluence (70 μJ) excitation. The solid lines represent the measured waveforms and the dashed lines represent the calculated waveforms.

Fig. 4.9 shows the measured THz waveforms by single-pulse excitation emitted from SI-GaAs emitter and LT-GaAs emitter annealed at 600°C. The cases for excitation fluence of $0.7\,\mu$J [(a) and (c)], and $70\,\mu$J [(b) and (d)] are shown here. We can observe several features. Firstly, while the waveforms from SI-GaAs emitter did not change much at different excitation fluence, the ones from LT-GaAs emitter change very much when the fluence was increased from $0.7\,\mu$J to $70\,\mu$J. We can clearly observe that the negative peak, which is as high and fast as the positive peak in the low fluence excitation case as shown in (a), becomes very broad and weak. This can be explained by the saturation effect. From Eq. 4.8, we know that negative feature comes from the falling edge of the current profile, while the positive part comes from rising edge of the current. When the excitation fluence is small, i.e. when the emitter is not in the saturation, the current follows the temporal profile of the carrier concentration. Therefore, when the carrier concentration dies out with short lifetime, the current does too, which generates a strong negative peak. When the emitter is excited by high fluence beams, the THz waveforms change from saturation effect. When the emitter is driven into the saturation regime, the current does not decay fast even when the carrier concentration does because in deep saturation, current is not sensitive to the carrier concentration or conductivity (Eq. 4.7). This slow decay of current at high fluence leads to the smaller negative peak and extended decay. Furthermore, with high fluence excitation, a lot of carriers are generated in the substrate, and the presence of the large population of the long lifetime carriers affect the waveforms.

Secondly, with low fluence excitation, the SI-GaAs emitter gives stronger emission (positive peak= 3.7) than the LT-GaAs emitter (positive peak = 1.6). But, at the high fluence, THz emission from LT-GaAs is comparable to or slightly stronger than the emission from SI-GaAs. This is because at the low fluence excitation the mobility of the photoconductor determines the strength of the THz radiation, while at the high fluence they saturate into the same strength determined by the bias value. The dashed lines in Fig. 4.9 show the calculated THz waveforms from SI-GaAs emitter and LT-GaAs emitter with the corresponding excitation conditions used in experiment. Throughout this paper, the linear absorption coefficient $\alpha_0 = 1.25/\mu$m was used. The amplitude of the calculated waveforms were normalized so that the measured and calculated waveforms have the same peak intensity for low fluence excitation of LT-GaAs (Fig. 4.9 (a)). We can observe good agreement in the amplitude between the corresponding measured and calculated waveforms in Fig. 4.9. Again, the negative features in the waveforms from SI-GaAs can not be explained. However, the waveform

measured from high fluence excitation of LT-GaAs generated a waveform very close to the one predicted by calculation.

With single pulse excitation, not much improvement was possible in obtaining high-power THz radiation, even when we use short lifetime material, because they were all subject to the same saturation limit from the fact the carrier lifetime is much longer than the pulse duration. (Even with the carrier lifetime much shorter than pulse duration, one cannot get enhancement because then the amount of current itself will be reduced.)

4.5.3 Two-pulse experiment

In order to observe the duration of the saturation effect directly, we performed two-pulse experiments [107] on the LT-GaAs and SI-GaAs emitters. We used two equal optical fluence pump beams to excite the emitters and scanned the spacing between the two pump beams, while only one of the pump beams was mechanically chopped. The probe beam delay was set such that the we measure the peak THz signal from the chopped excitation beam. Fig. 4.10 shows the result of the two-pulse experiments on (a) SI-GaAs and (b) LT-GaAs emitters. The LT-GaAs was annealed at 600°C. The results for optical fluence of $40\,\mu$J, $5\,\mu$J, and $0.5\,\mu$J for each pump pulse are shown and all results are individually normalized. The negative time delay means that the chopped pump pulse arrives before the un-chopped pump pulse. As expected from the results of Ref. [107], for SI-GaAs emitter, the radiation from the chopped pump pulse is dramatically reduced from the value before the arriving of the un-chopped pump (negative time delay in the figure) and does not recover at all. Some sharp features around zero time delay seem to be from the coherent artifact from the interaction of two pump pulses when they overlap in time [116]. We observe that the saturation effect in SI-GaAs is quite dramatic even with low fluence excitation. When we do the single-pulse excitation experiment with varying excitation fluence, the saturation effect with below μJ excitation fluence is very weak. The difference arise because the far-field radiation is generated mostly during the rising edge of the current profile in the SI-GaAs. Therefore, in the single pulse excitation case, the peak of the THz field does not correspond to the near maximum of the carrier concentration, and THz emission process suffers less from saturation. But in the two-pulse (or multiple pulse) experiment, the carrier population generated by the first pulse has not decayed when the second pulse arrives. Therefore, THz generation process from the second

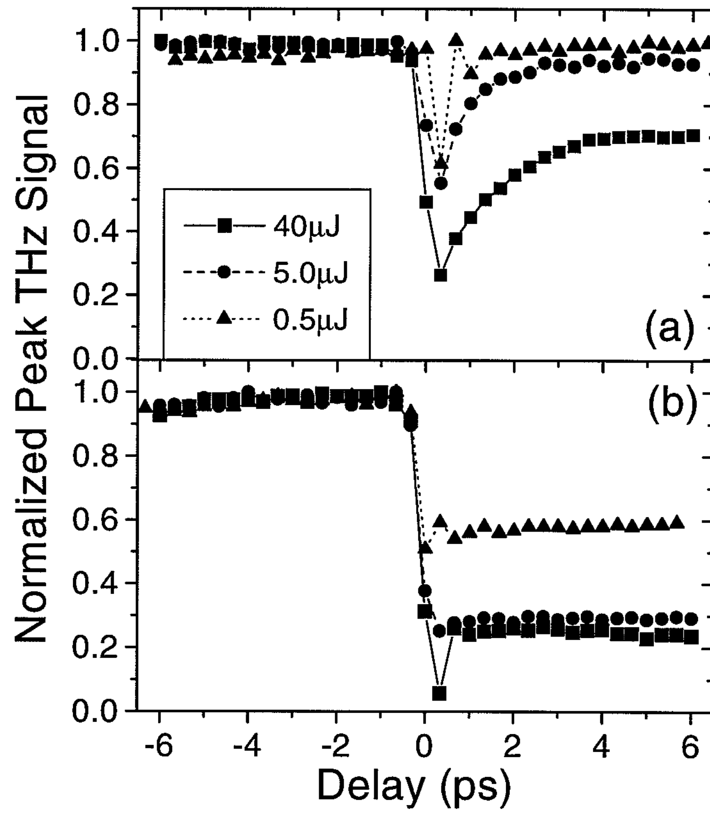

Fig. 4.10. Results of two-pulse THz emission experiments where the peak amplitude of the second emitted THz pulse is plotted versus inter-pulse separation for (a) a LT-GaAs emitter annealed at 600°C and (b) a SI-GaAs emitter

excitation pulse sees entire carrier concentration from the first pulse and experiences more severe saturation.

In contrast to the SI-GaAs emitter, the LT-GaAs emitter shows very different features. Firstly, they have very fast recovery. Once again, the sharp feature which is seen very clearly for 0.5 μJ excitation case seems to be from coherent artifact. Because of this, it is difficult to determine the recovery time of the LT-GaAs from this low fluence excitation data. However, the recovery looks complete after 1.3 ps. The higher fluence excitation results show somewhat slower and non-complete recovery, of which the degree is increasing with increasing fluence. This feature seems to be from the absorption of the pump light in the substrate. One might think of the possibility of the saturation of traps in the LT-GaAs layer [64]. The fast removal of the carriers from the conduction band in the LT-GaAs is due to the traps induced by excessive arsenic in the epitaxial film. But, when the traps remove electrons from the conduction band, the actual recombination of the trapped electrons with the holes takes much longer time. Therefore, once the trap is filled with electrons, the trapping of the electrons in the conduction band can be stopped. However, this seems not to be the case. We performed optical pump and terahertz probe experiments [36] on several LT-GaAs thin-films. Fig. 4.11 shows the result of the experiments. The experiments were performed on the same 2.8 μm thick GaAs [(c)] as well as on a different 1 μm thick LT-GaAs [(a), (b)] which was grown in a similar condition as our 2.8 μm thick LT-GaAs. We repeated the experiments with this 1 μm thickness sample with [(a)] and without [(b)] the substrate removed. The measurements with 2.8 μm sample were performed only with a sample with the substrate. Fig. 4.11 (b) shows the complete recovery with the excitation energy of 70 μJ, while the sample with substrate showed incomplete recovery with 15μJ excitation. 2.8 μm sample also shows incomplete and slow recovery with higher fluence excitations [Fig. 4.11]. Given that our current sample is 2.8 μm thick, the observed incomplete recovery should be from the substrate absorption and the possibility of trap saturation is very slim.

We performed simulations of the two-pulse experiments to verify our understanding of the saturation. The basic approach is to use the equations given in Sec. 4.4.2. But, because of the nature of pump scheme where only one of the two pump pulses was chopped, the procedure was modified a little in order to simulate the detection of the THz radiation from the second excitation pulse only. First, we calculated the reference THz waveform with single excitation pulse. Then, we repeated the calculations with two pump pulses and the simulated THz waveforms corresponding to our

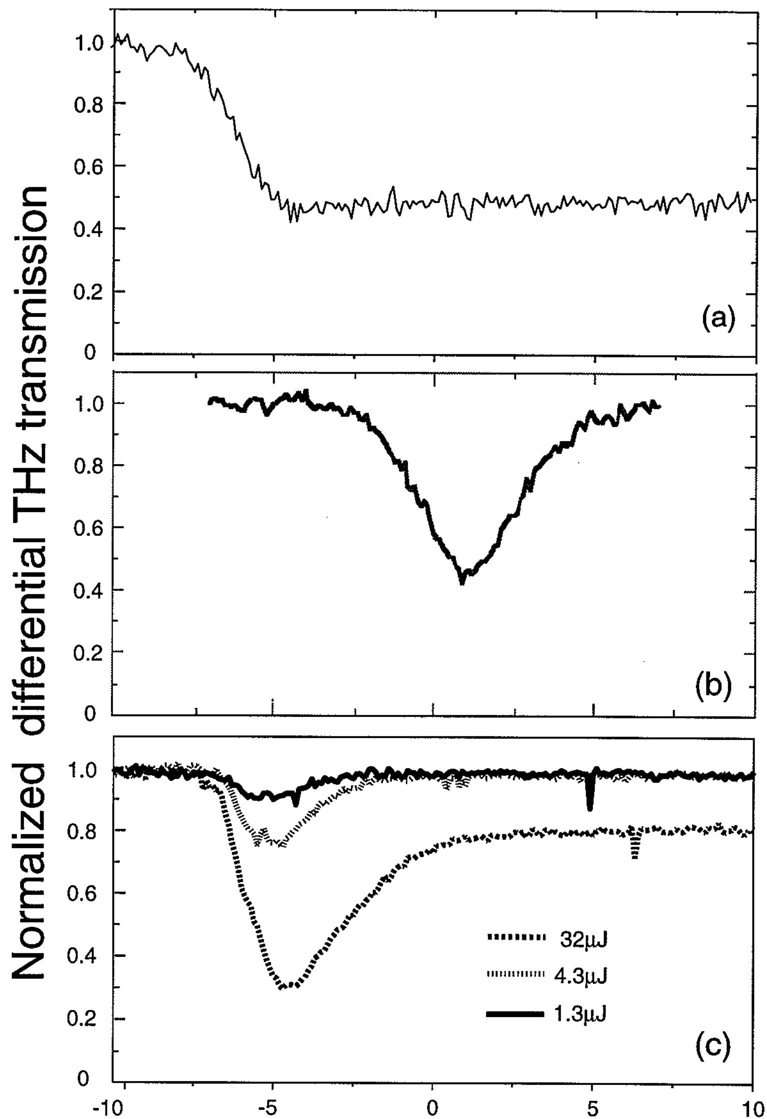

Fig. 4.11. Optical pump / THz probe experiments on several LT-GaAs samples. (a) 1 μm thick LT-GaAs with substrate (15μJ pump energy) (b) 1 μm thick LT-GaAs with substrate removed (70μJ pump energy) (c) 2.8 μm thick LT-GaAs with substrate with pump energy indicated in the figure.

experiment were obtained by subtracting the reference THz waveform from the calculated two-pulse excited waveform. Since we measured only the peak THz amplitude in the actual experiment, only peak THz value which corresponds to the position of the second pulse was recorded while the delay between the two pulses scanned. Fig. 4.12 shows the result of the simulation. For this simulation, electron mobility of LT-GaAs and SI-GaAs were assumed to be 1500 $cm^2/V{\cdot}s$ and 3000 $cm^2/V{\cdot}s$, respectively. The carrier lifetime was 0.7 ps for LT-GaAs layer and 100 ps for SI-GaAs layer. We observe a qualitative agreement between the corresponding curves in Fig. 4.10 and Fig. 4.12. We observe that combined response from the LT-GaAs layer and the SI-GaAs substrate is slowed down when excited by very high fluence and the signal does not recover to its original value after long time. This again confirms the importance of the role of the substrate absorption when we design LT-GaAs emitters for very high optical excitation fluence operation.

4.5.4 Narrow-band THz generation using multiple-pulse excitation

Fig. 4.13 shows the representative THz waveforms from emitters on LT-GaAs annealed at 600°C [(a),(b)] and SI-GaAs [(c),(d)] for excitation by 8-pulse sequence. Fig. 4.13 (a),(c) are the case of 2 μJ integrated optical excitation fluence and Fig. 4.13 (b),(d) are of 70 μJ integrated fluence. The small peaks which appear at around 15, 19, 22 ps are from reflections. The corresponding calculated waveforms are plotted in dotted lines in Fig. 4.13. The same parameters were used as before. As observed in Fig. 4.13 (a), when the optical excitation fluence is low, the THz pulse train from the LT-GaAs is just the linear combination of the THz waveform by single pulse excitation. This is the exactly expected results, when there is no saturation effect. On the other hand, Fig. 4.13 (c) shows that the THz pulse train from SI-GaAs suffers from the saturation even with low fluence excitation which is evidenced by the decreasing magnitude of peaks. Again, the negative features from the SI-GaAs waveforms are not clearly understood. When the excitation fluence is increased to 70 μJ, LT-GaAs emitter shows some sign of the saturation [Fig. 4.13 (b)]. This saturation is, as we discussed before in the Sec. 4.5.3, from the photo-carrier generation in the SI-GaAs substrate. But even in this case, the last pulse in the train retains more than 60% of the peak amplitude of the first one.

Fig. 4.14 shows power spectrum of the THz waveforms from the LT-GaAs [(a),(b)] and the SI-GaAs [(c),(d)] excited by either single or 8 pulse sequence. Figs. 4.14 (a) and (c) are for 2 μJ integrated fluence while (b) and (d) are for 70 μJ integrated

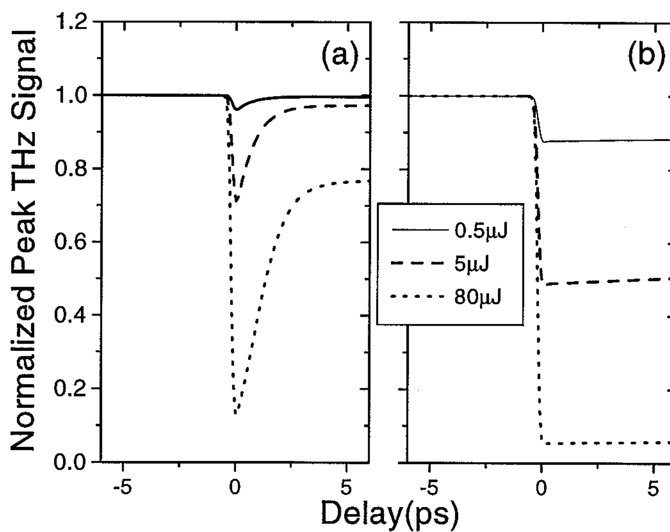

Fig. 4.12. Simulated results of two-pulse THz emission experiment where the peak amplitude of the second emitted THz pulse is plotted versus inter-pulse separation for a SI-GaAs emitter and LT-GaAs emitter. (a) LT-GaAs layer on SI-GaAs substrate: $\tau_{r,LT}$=0.7 ps, $\tau_{r,SI}$=100 ps.(b) SI-GaAs: τ_r=100 ps.

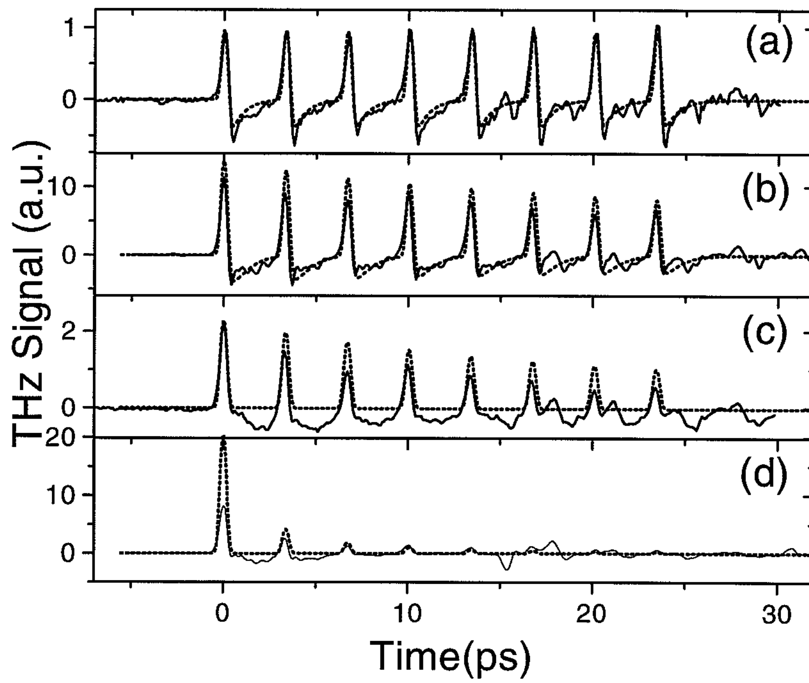

Fig. 4.13. Measured and Calculated THz radiation waveforms from LT- and SI-GaAs emitters excited by 8-pulse sequences. The LT-GaAs was annealed at 600°C. (a),(b): LT-GaAs emitter. (c),(d): SI-GaAs emitter; (a),(c): excitation fluence of 2 μJ, (b),(d): excitation fluence of 70 μJ.

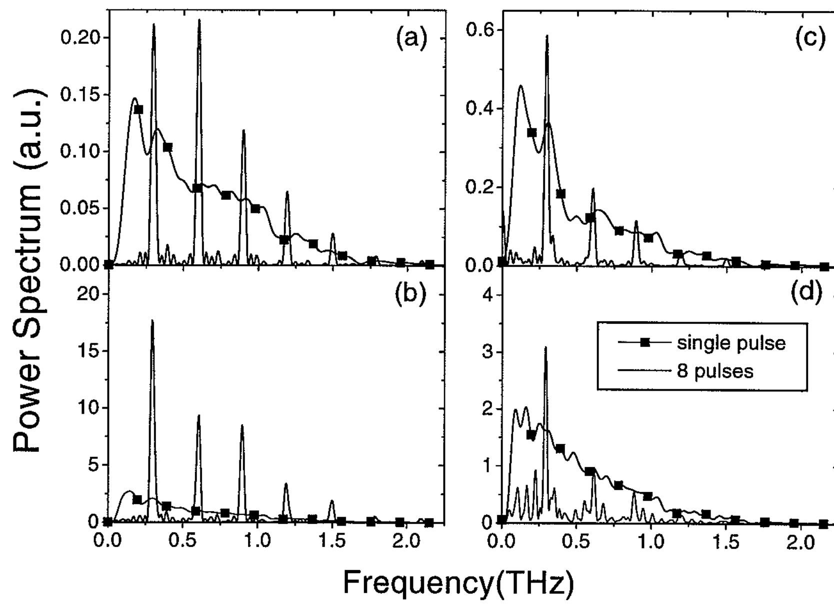

Fig. 4.14. Power spectral density of THz radiation excited by a single pulse and 8-pulse sequence. (a),(b): LT-GaAs emitter (annealed at 600°C) (c),(d): SI-GaAs emitter; (a),(c): Low integrated excitation fluence ($2\,\mu$J) (b),(d): high integrated excitation fluence ($70\,\mu$J).

fluence. The $2\,\mu$J integrated fluence was the lowest fluence where we have both single pulse and 8-pulse excitation data. We can see that at $2\,\mu$J excitation, the emitters are already in a slight saturation in single pulse excitation case, from the fact that the peaks of the 8 pulse excited THz spectrum go higher than the spectral density obtained from the single pulse excitation waveforms. In Fig. 4.14 (c), we can clearly observe very high power narrow-band THz radiation achieved by using multiple-pulse sequence.

In Fig. 4.15, the power spectral density at the fundamental frequency ($f = 1/T =$ 300 GHz) of the THz waveforms from (a) SI-GaAs and (b) LT-GaAs emitters excited by single or multiple pulses are shown. The LT-GaAs was annealed at 600°C. It should be noted again that in the 8-pulse excitation case, the term 'fluence' means integrated pulse energy over all pulses in the pulse train. The dashed line is for the guide of the eye and it represents the quadratic fluence dependence of the power spectral density on the excitation fluence. When the emitter is not in saturation mode, the peak power spectral density is expected to follow this dependence, because the THz amplitude should be proportional to the current density which is again proportional to the optical excitation fluence through photo-generated carrier density. Judging from the slope of the curve in Fig. 4.15 (a), the SI-GaAs emitter seems to be in slight saturation even in the lowest excitation fluence we used. This is in agreement with the time domain data shown in Fig. 4.13. When the fluence is increased, we observe very strong saturation of the THz power for all single- or multiple-pulse excitation cases with the SI-GaAs emitter. The spectral power density data for LT-GaAs emitter shows different features. In the lowest excitation region, the slope of the curve is almost exactly two. This is again in agreement with the time domain data which showed the linear operation of the emitter. And when we increased the excitation fluence, multiple-pulse excitation case gives stronger THz radiation than the single pulse excitation. The enhancement obtained by using 8 pulse excitation compared to the single pulse excitation is 7.5 when measured for $70\,\mu$J excitations.

Fig. 4.16 shows the calculated version of Fig. 4.15. The same set parameters as in Sec. 4.5.3 was used for this calculation which corresponds to the emitters on SI-GaAs and LT-GaAs annealed at 600°C. ($\mu_{LT} = 1500\text{cm}^2/V \cdot sec$, $\mu_{SI} = 3000\text{cm}^2/V \cdot sec$, $\tau_{r,LT} = 0.7\,\text{ps}$ and $\tau_{r,SI} = 100\,\text{ps}$) Fig. 4.16 (a) shows that for SI-GaAs emitter, no enhancement can be obtained by using multiple pulse excitation when the integrated fluence is fixed, while Fig. 4.16 shows large enhancement from LT-GaAs emitter excited by multiple pulse sequence. Interesting thing is that performance of LT-GaAs

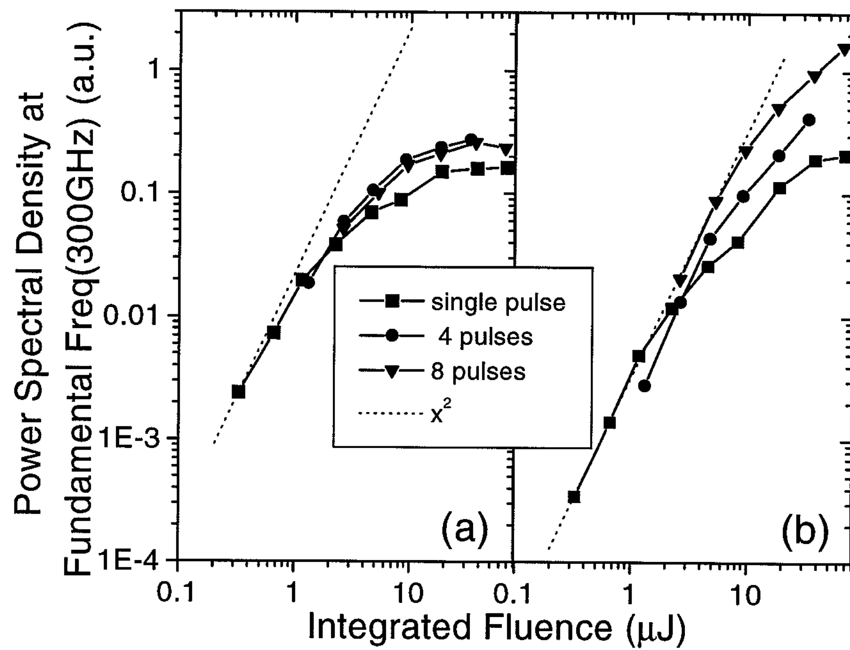

Fig. 4.15. Power spectral density of THz radiation at the fundamental frequency of 0.3 THz versus optical fluence. (a) SI-GaAs emitter (b) LT-GaAs emitter (600°C annealed)

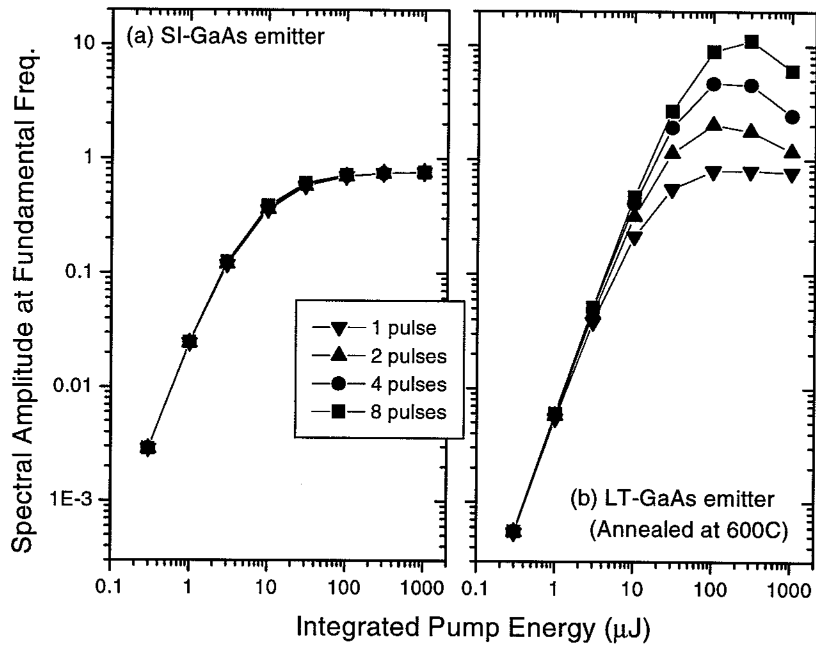

Fig. 4.16. Calculated power spectral density of THz radiation at the fundamental frequency of 0.3 THz versus optical fluence. (a) SI-GaAs emitter (b) LT-GaAs emitter (0.7 ps carrier lifetime)

emitter becomes poorer above $300\mu J$ excitation energy. This comes from the fact that at very high fluence level the carriers generated in the substrate dominate the THz generation process. Therefore, at the high fluence limit, the performance of the LT-GaAs emitter converges to that of SI-GaAs. This gives the upper bound of excitation energy which can be used to extract more THz energy. From the calculation, we estimate this energy for our LT-GaAs emitter to be between $100\,\mu J$ and 1 mJ.

In Fig. 4.17, power spectral density at the fundamental frequency of the THz waveforms from SI-GaAs and LT-GaAs emitter excited by (a) single-pulse or (b) 8 pulses is shown. The dashed lines are again for the guide of eye. When the emitter is excited by a single pulse of low fluence, the THz amplitude is proportional to the mobility and bias electric field. When we look at the low fluence excitation part of Fig. 4.17, we observe that SI-GaAs emitter generates strongest radiation and LT-GaAs emitter annealed at 575°C generates weakest radiation. This is expected because of reduced mobility of LT-GaAs, especially the ones annealed at lower temperatures. From the observed factor of 12 difference in measured THz power, we can estimate the difference in mobility. Since the current is proportional to the mobility, the factor of 12 difference in THz power translates into factor of $\sqrt{12} \simeq 3.5$ difference in mobility between the SI-GaAs and the LT-GaAs annealed at 575°C. This is in rough agreement with the mobility of LT-GaAs [117]. With high fluence excitation all THz radiation power density converge into a single value determined by bias. Here, we observe that the high electron mobility of the SI-GaAs photoconductor does not contribute to high THz amplitude when it is limited by the saturation. In Fig. 4.17 (b), we find again that at low excitation fluence, the high mobility of the SI-GaAs layer has the advantage in generating more THz energy even with 8 pulse excitation. But, when the excitation fluence is increased, this order is reversed and at the highest fluence used in the experiments, SI-GaAs emitter generated the least THz power. When comparing LT-GaAs emitters, the LT-GaAs emitter annealed at 600°C has the best performance. The reason that 600°C annealed LT-GaAs has better performance than the one annealed at 575°C is the higher mobility of 600°C sample. But, it should be noted that none of them are in complete saturation in the fluence range used in our experiments as can be seen from the slopes of the curves. Therefore, it is possible that when we increase the fluence range more, the 575°C annealed sample have the best performance.

In Sec. 4.2, it was shown that when an emitter is in complete saturation, the enhancement in peak power spectral density which can be obtained by using N-pulse

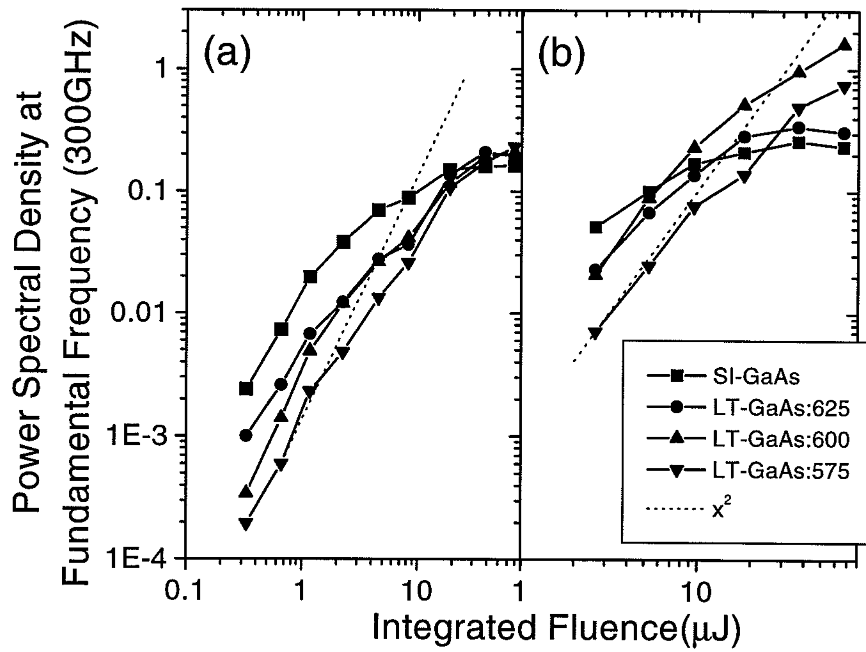

Fig. 4.17. Power spectral density of THz radiation at the fundamental frequency of 0.3 THz versus optical fluence. (a) single pulse excitation (b) 8-pulse sequence excitation

sequence is a factor of N^2. In this case of 8-pulse excitation, this predicts a factor of 64 enhancement. The reason that we have only factor of 7.5 enhancement is twofold. Firstly, when the excitation fluence is very high, the saturation effect from the photo-generated carriers in the substrate plays important role. Therefore, the assumption of complete recovery between the pulses in the pulse-train which was assumed in the theory does not hold. Secondly, in the theory, we assumed that the emitter is in complete saturation such that the individual pulses in the train can generate the THz radiation of the same strength as the single pulse which has same integrated fluence as the whole pulse train. But in this experiment, it is not the case. In Fig. 4.17 (a), we observe that the THz power density from 600°C annealed LT-GaAs emitter by a single pulse excitation of $70\,\mu$J and $9\,\mu$J are different by factor of $\sim$5. The fluence of $9\,\mu$J is approximately the same fluence which the individual pulse in $70\,\mu$J integrated fluence 8-pulse sequence. Therefore, we know that the individual pulses in that pulse train do not drive the emitter into saturation. If we carefully observe the slope of for 600°C annealed LT-GaAs in Fig. 4.17, we can find that even $70\,\mu$J single pulse cannot drive the system into complete saturation. Therefore, to observe the predicted maximum enhancement of 64, the integrated fluence of the 8-pulse sequence should be larger than $70 \times 8 = 560\mu$J.

4.6 Conclusion

In this chapter, we developed a scheme to generate high-power narrow-band THz radiation using multiple-pulse excitation on the PC-emitters. By using multiple-pulse excitation in combination with short carrier lifetime of photoconductors, we could avoid the saturation of the THz radiation from PC-emitters when they are excited by high fluence optical pulses. We performed experiments with dipole antenna with unamplified excitation pulses and could get good improvement in the peak power spectral density. Then we extended this technique to the case where we used large-aperture emitters with amplified high fluence pulses. We have investigated the saturation properties of the biased, large-aperture photoconductors excited by trains of amplified femtosecond optical pulses. A direct comparison was made of the saturation properties of SI-GaAs and LT-GaAs emitters with different carrier lifetimes in view of the multiple-pulse excitation. Both numerical calculations based on the radiation screening theory of large-aperture antenna and the experimental results showed that a large enhancement of the narrow-band THz output under multiple-pulse excitation

is possible when the carrier lifetime of the photoconductor is less than the inter-pulse spacing. When the carrier lifetime was longer than the inter-pulse spacing, the radiation screening effect from the long-lived current made the enhancement reduced, if any. This confirms the near-field nature of the saturation from radiation screening. We also found that the thickness of the short carrier lifetime photoconductor is a very important parameter. If the photoconductor is not thick enough, substantial population of carriers is generated in the long carrier lifetime substrate when the emitter is excited by high fluence pulses, and it leads to the degradation of the device. We can use these results to design high power narrow-band THz emitters.

5. CONCLUSION

5.1 Summary

In these research, I have studied various aspects of THz radiation such as generation, manipulation, and detection.

For the first time, I quantitatively compared the THz waveforms measured by E-O and PC detection. I used relatively thin ZnTe E-O sensor to obtain true incoming electric-field waveforms which were used as a reference in the comparison. The difference between the E-O and PC measured THz waveforms could be explained in terms of the PC-antenna response and the photoconductive material response.

The flat frequency response of dipole PC-antennas were experimentally demonstrated and theoretically explained. The $\sim j\omega$ frequency of dipole PC-antennas attached to hyper-hemispherical silicon substrate lens was also observed and explained in terms of the frequency dependent spot size of the THz electric field at the PC-antenna which is specific for our system.

The near-field effect and the transition from the near-field to the far-field region were observed for the wide-band THz radiation. When the aperture sizes of the detector and the emitter were small as in the case of E-O detection or PC-detection without a silicon lens along with 1 mm emitter aperture, the near-field effect was not noticeable. But when the detector size was large as in the case of PC-detection with a silicon lens, the near-field to far-field transition was clearly observed.

I synthesized the shape of the THz radiation by using a femtosecond optical pulseshaper. By shaping the excitation pulse to the photoconductive emitter, I could generate a number of THz waveforms including binary bit streams, phase modulated radiation, and tunable narrow-band radiation. Also the measured THz waveforms closely match the waveforms calculated from linear response theory. A discussion was made on the new THz pulse-shaping scheme which uses difference frequency mixing in electro-optic crystals. Using this technique, we expect to generate polarization controlled THz waveforms.

Finally, I demonstrated the generation of the high-power narrow-band THz radiation avoiding the saturation of the photoconductive antenna with high fluence excitation. With multiple-pulse train excitation we could reduce the peak intensity of the excitation pulses. Therefore, when we used short-carrier lifetime LT-GaAs which has shorter carrier lifetime than the inter-pulse spacing, we could reduce the effect of the saturation. First, I demonstrated the concept of saturation avoidance using a small dipole emitter and unamplified excitation pulses. Then I extended this technology to real higher power where we used large-aperture antenna and high fluence amplified excitation. Here, we achieved more than factor of 7 enhancement in the peak power spectral density and more enhancement is promising.

5.2 Future works

In Chap. 2, the transition of the broadband terahertz radiation from near-field to far-field was observed only in PC-detector with silicon lens. In the E-O sampling it was not possible to observe the transition because the presence of the pellicle beam splitter determined the minimum separation between the emitter and detector. However, if we use a emitter with larger size (i.e. 1 cm), it is expected to observe the transition with small aperture size detection such as E-O sampling and PC-sampling without silicon lens.

In Chap. 3, THz pulse-shaping using difference frequency mixing (DFM) has been proposed. I had to stop in the middle of the project because of the time constraints. Advantage of this scheme to the intensity driven system was already described. Currently only one shaper is planned. But obviously, this can be extended to full fledged system with two shaper. Some theoretical work is in due concerning the tolerance of the THz generation process to the relative phase error of the two beams.

In Chap. 4, we used the strength of the THz radiation from large-aperture PC-emitters fabricated on SI-GaAs and LT-GaAs photoconductors to roughly determine the relative carrier mobilities of the materials. We can pursue this more to decide the relative mobility of the photoconductors more precisely. It would require more thorough understanding of the THz generation dynamics and carrier dynamics in the semiconductor photoconductors.

LIST OF REFERENCES

[1] D. H. Auston, K. P. Cheung, and P. R. Smith, "Picosecond photoconducting Hertzian dipoles," *Appl. Phys. Lett.*, vol. 45, pp. 284–286, 1984.

[2] P. R. Smith, D. H. Auston, and M. C. Nuss, "Subpicosecond photoconducting dipole antennas," *IEEE J. Quantum Electron.*, vol. QE-24, pp. 255–260, 1988.

[3] X.-C. Zhang, B. B. Hu, J. T. Darrow, and D. H. Auston, "Generation of femtosecond electromagnetic pulses from semiconductor surfaces," *Appl. Phys. Lett.*, vol. 56, pp. 1011–1013, 1990.

[4] N. M. Froberg, B. B. Hu, X.-C. Zhang, and D. H. Auston, "Terahertz radiation from a photoconducting antenna arrays," *IEEE J. Quantum Electron.*, vol. 28, pp. 2291–2301, 1992.

[5] B. B. Hu, A. S. Weling, D. H. Auston, A. V. Kuznetsov, and C. J. Stanton, "dc-electric-field dependence of THz radiation induced by femtosecond optical excitation of bulk GaAs," *Phys. Rev. B*, vol. 49, pp. 2234–2237, 1994.

[6] M. van Exter, C. Fattinger, and D. Grischkowsky, "High-brightness terahertz beams characterized with an ultrafast detector," *Appl. Phys. Lett.*, vol. 55, pp. 337–339, 1989.

[7] D. R. Grischkowsky, M. B. Ketchen, C.-C. Chi, I. I. N. Duling, N. J. Halas, J.-M. Halbout, and P. G. May, "Capacitance free generation and detection of subpicosecond electrical pulses on coplanar transmission lines," *IEEE J. Quantum Electron.*, vol. 24, pp. 221–225, 1988.

[8] C. Fattinger and D. R. Grischkowsky, "A Cherenkov source for freely-propagating terahertz beams," *IEEE J. Quantum Electron.*, vol. 25, pp. 2608–2610, 1989.

[9] C. Fattinger and D. Grischkowsky, "Point source terahertz optics," *Appl. Phys. Lett.*, vol. 53, pp. 1480–1482, 1988.

[10] C. Fattinger and D. Grischkowsky, "Terahertz beams," *Appl. Phys. Lett.*, vol. 54, p. 490, 1989.

[11] C. Fattinger and D. R. Grischkowsky, "Beams of terahertz electromagnetic pulses," in *OSA proceedings on picosecond electronics and optoelectronics*, pp. 225–231, 1989.

[12] M. van Exter and D. Grischkowsky, "Characterization of an optoelectronic terahertz beam system," *IEEE Tran. Microwave Theory and Tech.*, vol. 38, pp. 1684–1691, 1990.

[13] G. Mourou, C. V. Stancampiano, and D. Blumenthal, "Picosecond microwave pulse generation," *Appl. Phys. Lett.*, vol. 38, pp. 470–472, 1981.

[14] X.-C. Zhang, Y. Jin, and X. F. Ma, "Coherent measurement of THz optical rectificationfrom electro-optic crystals," *Appl. Phys. Lett.*, vol. 61, pp. 2764–2766, 1992.

[15] A. Rice, Y. Jin, X. F. Ma, X.-C. Zhang, D. Bliss, J. Larkin, and M. Alexander, "Terahertz optical rectification from <110> zinc-blende crystals," *Appl. Phys. Lett.*, vol. 64, pp. 1324–1326, 1994.

[16] Q. Wu and X.-C. Zhang, "7 terahertz broadband gap electro-optic sensor," *Appl. Phys. Lett.*, vol. 70, pp. 1784–1786, 1997.

[17] Q. Wu and X.-C. Zhang, "Ultrafast electro-optic field sensors," *Appl. Phys. Lett*, vol. 68, pp. 1604–1606, 1996.

[18] Q. Wu, M. Litz, and X.-C. Zhang, "Broadband detection capability of ZnTe electro-optic field detectors," *Appl. Phys. Lett*, vol. 68, pp. 2924–2926, 1996.

[19] Q. Wu, F. G. Sun, P. Campbell, and X.-C. Zhang, "Dynamic range of an electro-optic field sensor and its imaging applications," *Appl. Phys. Lett*, vol. 68, pp. 3224–3226, 1996.

[20] Q. Wu, T. D. Hewitt, and X.-C. Zhang, "Two-dimensional electro-optic imaging of THz beams," *Appl. Phys. Lett*, vol. 69, pp. 1026–1028, 1996.

[21] Q. Wu and X.-C. Zhang, "Design and characterization of traveling-wave electrooptic terahertz sensors," *J. Select. Topics in Quantum Electron.*, vol. 2, pp. 693–700, 1996.

[22] M. van Exter, C. Fattinger, and D. Grischkowsky, "Terahertz time-domain spectrocopy of water vapor," *Opt. Lett.*, vol. 14, pp. 1128–1130, 1989.

[23] M. van Exter and D. Grischkowsky, "Carrier dynamics of electrons and holes in moderately doped silicon," *Phys. Rev. B*, vol. 41, pp. 12140–12149, 1990.

[24] M. van Exter and D. Grischkowsky, "Optical and electronic properties of doped silicon from 0.1 to 2 THz," *Appl. Phys. Lett.*, vol. 56, pp. 1694–1696, 1990.

[25] D. Grischkowsky, S. Keiding, M. van Exter, and C. Fattinger, "Far-infrared time-domain spectroscopy with terahertz beams of dielectrics and semiconductors," *J. Opt. Soc. Am. B*, vol. 7, pp. 2006–2015, 1990.

[26] N. Katzenellenbogen and D. Grischkowsky, "Electrical characterization to 4 THz of n- and p-type gaas using THz time-domain spectroscopy," *Appl. Phys. Lett.*, vol. 61, pp. 840–842, 1992.

[27] R. A. Cheville and D. Grischkowsky, "Time domain terahertz impulse ranging studies," *Appl. Phys. Lett.*, vol. 67, pp. 1960–1962, 1995.

[28] H. Harde, R. A. Cheville, and D. Grischkowsky, "Terahertz studies of collision-broadened rotational lines," *Phys. Chem. A*, vol. 101, pp. 3646–3660, 1997.

[29] T.-I. Jeon and D. Grischkowsky, "Nature of conduction in doped silicon," *Phys. Rev. Lett.*, vol. 78, pp. 1106–1109, 1997.

[30] T.-I. Jeon and D. Grischkowsky, "Observation of a Cole-Davidson type complex conductivity in the limit of very low carrier densities in doped silicon," *Appl. Phys. Lett.*, vol. 72, pp. 2259–2261, 1998.

[31] R. A. Cheville and D. Grischkowsky, "Observation of pure rotational absorption spectra in the ν_2 band of hot H_2O in flames," *Opt. Lett.*, vol. 23, pp. 531–533, 1998.

[32] M. C. Nuss, P. M. Mankiewich, M. L. O'Malley, and E. H. Westerwick, "Dynamic conductivity and Coherence peak in $YBa_2Cu_3O_7$ superconductors," *Phys. Rev. Lett.*, vol. 66, pp. 3305–3308, 1991.

[33] M. C. Nuss, K. W. Goossen, J. P. Gordon, P. M. Mankiewich, M. L. O'Malley, and M. Bhushan, "Terahertz time-domain measurement of the conductivity and superconducting band gap in niobium," *J. Appl. Phys.*, vol. 70, pp. 2238–2241, 1991.

[34] M. C. Nuss, K. W. Goossen, P. M. Mankiewich, and M. L. O'Malley, "Terafertz surface impedance of thin $YBa_2Cu_3O_7$ superconducting films," *Appl. Phys. Lett.*, vol. 58, pp. 2561–2563, 1991.

[35] J. O. White, R. Buhleier, S. D. Bronson, I. E. Trofimov, H.-U. Habermeier, and J. Kuhl, "Complex conductivity of $Y_{1-x}Pr_xBa_2Cu_3O_7$ thin films measured by coherent terahertz spectroscopy.," *Physica C*, vol. 235-240, pp. 2025–2026, 1994.

[36] S. S. Prabhu, S. E. Ralph, M. R. Melloch, and E. S. Harmon, "Carrier dynamics of low-temperature-grown gaas observed via thz spectroscopy," *Appl. Phys. Lett.*, vol. 70, pp. 2419–2421, 1997.

[37] B. B. Hu and M. C. Nuss, "Imaging with terahertz waves," *Opt. Lett.*, vol. 20, pp. 1716–1718, 1995.

[38] D. M. Mittleman, R. H. Jacobsen, and M. C. Nuss, "T-ray imaging," *J. Select. Topics in Quantum Electron.*, vol. 2, pp. 679–692, 1996.

[39] R. A. Cheville, R. W. McGowan, and D. R. Grsichkowsky, "Late-time target response measured with terahertz impulse ranging," *IEEE Tran. Ant. Prop.*, vol. 45, pp. 1518–1524, 1997.

[40] I. Brener, D. Dykaar, A. Frommer, L. N. Pfeiffer, J.Lopata, J. Wynn, K. West, and M. C. Nuss, "Terahertz emission from electric field sigularities in biased semiconductors," *Opt. Lett.*, vol. 21, pp. 1924–1926, 1996.

[41] B. B. Hu, E. A. de Souza, W. H. Knox, J. E. Cunningham, and M. C. Nuss, "Identifying the distinct phases of carrier transport in semiconductor with 10 fs resolution," *Phys. Rev. Lett.*, vol. 74, pp. 1689–1691, 1995.

[42] J. A. Valdmanis, G. Mourou, and C. W. Gabel, "Picosecond electo-optic sampling system," *Appl. Phys. Lett.*, vol. 41, pp. 211–212, 1982.

[43] Q. Wu and X.-C. Zhang, "Free-space electro-optic sampling of terahertz beams," *Appl. Phys. Lett.*, vol. 67, pp. 3523–3525, 1995.

[44] A. Nahata, D. H. Auston, T. F. Heinz, and C. Wu, "Coherent detection of freely propagating terahertz radiation by electro-optic sampling," *Appl. Phys. Lett.*, vol. 68, pp. 150–152, 1996.

[45] A. Nahata, A. S. Weling, and T. F. Heinz, "A wideband coherent terahertz spectroscopy system using optical recitification and electro-optic sampling," *Appl. Phys. Lett.*, vol. 69, pp. 2321–2323, 1996.

[46] S.-G. Park, M. R. Melloch, and A. M. Weiner, "Comparison of terahertz waveforms measured by electro-optic and photoconductive sampling," *Appl. Phys. Lett.*, accepted for publication.

[47] S.-G. Park, M. R. Melloch, and A. M. Weiner, "Analysis of terahertz waveforms measured by electro-optic and photoconductive sampling," submitted.

[48] Y. Cai, I. Brener, J. Lopata, J. Wynn, L. Pfeiffer, J. B. Stark, Q. Wu, X.-C. Zhang, and J. Federici, "Coherent terahertz radiation detection: direct comparison between free space electro-optic sampling and antenna detection," *Appl. Phys. Lett.*, vol. 50, pp. 444–446, 1998.

[49] A. Yariv, *Quantum Electronics.* New York: John Wiley & Sons, 1989.

[50] H. J. Bakker, G. C. Cho, H. Kurz, Q. Wu, and X.-C. Zhang, "Distortion of terahertz pulses in electro-optic sampling," *J. of Opt. Soc. Am. B*, vol. 15, pp. 1795–1801, 1998.

[51] P. R. Smith, D. H. Auston, A. M. Johnson, and W. M. Augustyniak, "Picosecond photoconductivity in radiation-damaged silicon-on-sapphire films," *Appl. Phys. Lett.*, vol. 38, pp. 47–50, 1981.

[52] S. Gupta, Y. Frankel, J. A. Valdmanis, J. F. Whitaker, G. A. Mourou, F. W. Smith, and A. R. Calawa, "Subpicosecond carrier lifetime in gaas grown by molecular beam epitaxy at low temperatures," *Appl. Phys. Lett.*, vol. 59, pp. 3276–3278, 1991.

[53] A. C. Warren, N. Katznellenbogen, D. Grischkowsky, J. M. Woodall, M. R. Melloch, and N. Otsuka, "Subpicosecond, freely propagating electromagnetic pulse generation and detectionusing GaAs:As epilayers," *Appl. Phys. Lett.*, vol. 58, pp. 1512–1514, 1991.

[54] M. R. Melloch, D. D. Nolte, J. M. Woodall, J. C. P. Chang, D. B. Janes, and E. S. Harmon, "Molecular beam epitaxy of nonstoichiometric semiconductors and multiphase material systems," *Crit. Rev. in Solid State and Mater. Sci.*, vol. 21, pp. 189–263, 1996.

[55] D. Grischkowsky, "Nonlinear generation of subpicosecond pulses of THz electromagnetic radiation by optoelectronics— application to time-domain spectroscopy," in *Frontiers in Nonlinear Optics* (H. Walther, N. Koroteev, and M. O. scully, eds.), pp. 196–228, Philadelphia, PA: Inst. of Physics, 1993.

[56] S. Ramo, J. R. Whinnery, and T. van Duzer, *Fields and waves in communication electronics.* New York, NY: John Wiley & Sons, 1984.

[57] C. A. Balanis, *Antenna theory.* New York: John Wiley & Sons, 1982.

[58] G. D. Monteath, *Applications of the electromagnetic reciprocity principle.* Oxford, UK: Pergamon Press, 1973.

[59] R. C. Hansen, "Fundamental limitations in antennas," *Proc. IEEE*, vol. 69, pp. 170–182, 1931.

[60] E. S. Harmon, M. R. Melloch, J. M. Woodall, D. D. Nolte, N. Otsuka, and C. L. Chang, "Carrier lifetime versus anneal in low temperature growth GaAs," *Appl. Phys. Lett.*, vol. 63, pp. 2248–2250, 1993.

[61] U. Keller, K. J. Weingarten, F. X. Kärtner, D. Kopf, B. Braun, I. D. Jung, R. Fluck, C. Hönninger, and J. A. der Au, "Semiconductor saturable absorber mirrors (sesams) for femtosecond to nanosecond pulse generation in solid-state lasers," *IEEE J. Select. Topics in Quantum Electron.*, vol. 2, pp. 435–453, 1996.

[62] P. Grenier and J. F. Whittaker, "Subband gap carrier dynamics in low-temperature-grown gaas," *Appl. Phys. Lett.*, vol. 70, pp. 1998–2000, 1997.

[63] S. D. Benjamin, H. S. Loka, A. Othonos, and P. W. E. Smith, "Ultrafast dynamics of nonlinear absorption in low-temperature-grown gaas," *Appl. Phys. Lett.*, vol. 68, pp. 2544–2546, 1996.

[64] U. Siegner, R. Fluck, G. Zhang, and U. Keller, "Ultrafast high-intensity nonlinear absorption dynamics in low-temperature grown gallium arsenide," *Appl. Phys. Lett.*, vol. 69, pp. 2566–2568, 1996.

[65] A. J. Lochtefeld, M. R. Melloch, J. C. P. Chang, and E. S. Harmon, "The role of point defects and arsenic precipitates in carrier trapping and recombination in low-temperature grown gaas," *Appl. Phys. Lett.*, vol. 69, pp. 1465–1467, 1996.

[66] Z. Q. Zhou, H. M. van Driel, W. W. Rühle, Z. Gogolak, and K. Ploog, "Femtosecond carrier kinetics in low-temperature-grown GaAs," *Appl. Phys. Lett.*, vol. 61, pp. 3020–3022, 1992.

[67] T. S. Sosnowski, T. B. Norris, H. H. Wang, P. Grenier, J. F. Whitaker, and C. Y. Sung, "High-carrier-density electron dynamics in low-temperature-grown GaAs," *Appl. Phys. Lett.*, vol. 70, pp. 3245–3247, 1997.

[68] J. Shah, "Photoexcited hot carriers: from cw to 6 fs in 20 years," *Solid-State Electron.*, vol. 32, pp. 1051–1056, 1989.

[69] M. B. Ketchen, D. Grischkowsky, T. C. Chen, C.-C. Chi, I. I. N. Duling, J. J. Halas, J. Halbout, J. A. Hash, and G. P. Li, "Generation of subpicosecond electrical pulses on coplanar transmission lines," *Appl. Phys.Lett.*, vol. 48, pp. 751–753, 1986.

[70] P. U. Jepsen, R. H. Jacobsen, and S. R. Keiding, "Generation and detection of terahertz pulses from biased semiconductor antennas," *J. Opt. Soc. Am. B*, vol. 13, pp. 2424–2436, 1996.

[71] A. M. Weiner, J. P. Heritage, and E. M. Kirschner, "High-resolution femtosecond pulse shaping," *J. Opt. Soc. Am. B*, vol. 5, pp. 1563–1572, 1988.

[72] A. M. Weiner, D. E. Leaird, J. S. Patel, and J. R. Wullert, "Programmable femtosecond pulse shaping by use of a multielement liquid-crystal phase modulator," *Opt. Lett.*, vol. 15, pp. 326–328, 1990.

[73] M. M. Wefers and K. A. Nelson, "Generation of high-fidelity programmable ultrafast optical waveforms," *Opt. Lett.*, vol. 20, pp. 1047–1049, 1995.

[74] E. Budiarto, N. W. Pu, S. Jeong, and J. Bokor, "Near-field propagation of terahertz pulses from a large-aperture antenna," *Opt. Lett.*, vol. 23, pp. 213–215, 1998.

[75] A. M. Weiner, "Femtosecond optical pulse shaping and processing," *Progress in Quantum Electron.*, vol. 19, pp. 161–238, 1995.

[76] K. A. Nelson, *"Ultrafast Phenomena IX"*, ch. Coherent control: Optics, molecules, and materials, pp. 47–49. Berlin, Germany: Springer-Verlag, 1994.

[77] S. H. Shi and H. Rabitz, "Optimal control of selective vibrational excitation of harmonic molecules: Analytic solution and restricted forms for the optimal fields," *J. Chem. Phys.*, vol. 92, pp. 2927–2937, 1990.

[78] J. Bromage, S. Radic, G. P. Agrawal, C. R. Stroud, P. M. Fauchet, and R. Sobolewski, "Spatiotemporal shaping of terahertz pulses," *Opt. Lett.*, vol. 22, pp. 627–629, 1997.

[79] N. M. Froberg, B. B. Hu, X.-C. Zhang, and D. H. Auston, "Time-division multiplexing by a photoconducting antenna array," *Appl. Phys. Lett.*, vol. Vol. 59, pp. 3207–3209, 1991.

[80] A. S. Weling, B. B. Hu, N. M. Froberg, and D. H. Auston, "Generation of tunable narrow-band THz radiation from large aperture photoconducting antennas," *Appl. Phys. Lett.*, vol. 64, pp. 137–139, 1994.

[81] A. S. Weling and D. H. Auston, "Novel sources and detectors for coherent tunable narrow-band terahertz radiation in free space," *J. Opt. Soc. Am. B*, vol. 13, pp. 2783–2791, 1996.

[82] P. C. M. Planken, I. Brener, M. C. Nuss, M. S. C. Luo, and S. L. Chuang, "Coherent control of terahertz charge oscillations in a coupled quantum well using phase-locked optical pulses," *Phys. Rev. B*, vol. 48, pp. 4903–4906, 1993.

[83] I. Brener, P. C. M. Planken, M. C. Nuss, D. E. Leaird, and A. M. Weiner, "Repetitive excitation of charge oscillations in semiconductor heterostructures," *Appl. Phys. Lett.*, vol. 63, pp. 2213–2215, 1993.

[84] I. Brener, P. C. M. Planken, M. C. Nuss, S. C. Luo, S. L. Chuang, L. Pfeiffer, D. E. Leaird, and A. M. Weiner, "Coherent control of terahertz emission and carrier populations in semiconductor heterostructures," *J. Opt. Soc. Am. B*, vol. 11, pp. 2457–2469, 1994.

[85] A. M. Weiner, D. E. Leaird, J. S. Patel, and J. R. Wullert, "Programmable shaping of femtosecond optical pulses by use of 128-element liquid crystal phase modulator," *IEEE J. Quantum Electon.*, vol. 28, pp. 908–920, 1992.

[86] A. M. Weiner, D. E. Leaird, G. P. Wiederrecht, and K. A. Nelson, "Femtosecond pulse sequences used for optical manipulation of molecular motion," *Science*, vol. 247, pp. 1317–1319, 90.

[87] A. M. Weiner and D. E. Leaird, "Generation of terahertz-rate trains of femtosecond pulses by phase-only filtering," *Opt. Lett.*, vol. 15, pp. 51–53, 1990.

[88] A. M. Weiner, D. E. Leaird, G. P. Wiederrecht, and K. A. Nelson, "Femtosecond multiple-pulse impulsive stimulated Raman scattering spectroscopy," *J. Opt. Soc. Am. B*, vol. 8, pp. 1264–1275, 1991.

[89] M. M. Wefers and K. A. Nelson, "Programmable phase and amplitude femtosecond pulse shaping," *Opt. Lett.*, vol. 18, pp. 2032–2034, 1993.

[90] C. W. Hillegas, J. X. Tull, D. Goswami, D. Strickland, and W. S. Warren, "Femtosecond laser pulse shaping by use of microsecond radio-frequency pulses," *Opt. Lett.*, vol. 19, pp. 737–739, 1994.

[91] Y. Liu, S.-G. Park, and A. M. Weiner, "Terahertz waveform synthesis via optical pulse shaping," *J. Select. Topics in Quantum Electron.*, vol. 2, pp. 709–719, 1996.

[92] R. N. Thurston, J. P. Heritage, A. M. Weiner, and W. J. Tomlinson, "Analysis of picosecond pulse shape synthesis by spectral masking in a grating pulse compressor," *IEEE J. Quantum Electron.*, vol. QE-22, pp. 682–696, 1986.

[93] A. M. Weiner, S. Oudin, D. E. Leaird, and D. H. Reitze, "Shaping of femtosecond pulses using phase-only filters designed by simulated annealing," *J. Opt. Soc. Am. A*, vol. 10, pp. 1112–1120, 1993.

[94] M. R. Schroeder, *Number Theory in Science and Communication.* Berlin: Springer-Verlag, 1986.

[95] R. W. Boyd, *Nonliear optics.* New York: Academic Press, 1992.

[96] K. H. Yang, P. L. Richards, and Y. R. Shen, "Generation of far-infrared radiation by picosecond light pulses in $LiNbO_3$," *Appl. Phys. Lett.*, vol. 19, pp. 320–323, 1971.

[97] L. Xu, X.-C. Zhang, and D. H. Auston, "Terahertz beam generation by femtosecond optical pulses in electro-optic materials," *Appl. Phys. Lett.*, vol. 61, pp. 1784–1786, 1992.

[98] A. Bonvalet, M. Joffre, J. L. Martin, and A. Migus, "Generation of ultrabroadband femtosecond pulses in the mid-infrared by optical recitification of 15fs light pulses at 100MHz repetition rate," *Appl. Phys. Lett.*, vol. 67, pp. 2907–2909, 1995.

[99] Heberle, J. J. Baumberg, and K. Köhler, "Ultrafast coherent control and destuction of excitons in quantum wells," *Phys. Rev. Lett.*, vol. 75, pp. 2598–2601, 1995.

[100] J. T. Darrow, X.-C. Zhang, D. H. Auston, and J. D. Morse, "Saturation properties of large-aperture photoconducting antennas," *IEEE J. Quantum Electron.*, vol. 28, pp. 1607–1616, 1992.

[101] D. You, R. R. Jones, P. H. Bucksbaum, and D. R. Dykaar, "Generation of high-power sub-single-cycle 500-fs electromagnetic pulses," *Opt. Lett.*, vol. 18, pp. 290–292, 1993.

[102] E. Budiarto, J. Margolies, S. Jeong, J. Son, and J. Bokor, "High-intensity terahertz pulses at 1-kHz repetition rate," *IEEE J. Quantum Electron.*, vol. 32, pp. 1839–1846, 1996.

[103] J. T. Darrow, X.-C. Zhang, and D. H. Auston, "Power scaling of large-aperture photoconducting antennas," *Appl. Phys. Lett.*, vol. 58, pp. 25–27, 1991.

[104] J. E. Pedersen, V. G. Lyssenko, J. M. Hvam, P. U. Jepsen, S. R. Keiding, C. B. Sørensen, and P. E. Lindelof, "Ultrafast local field dynamics in photoconductive THz antennas," *Appl. Phys. Lett.*, vol. 62, pp. 1265–1267, 1993.

[105] A. J. Taylor, P. K. Benicewicz, and S. M. Young, "Modeling of femtosecond electromagnetic pulses from large-aperture photoconductors," *Opt. Lett.*, vol. 18, pp. 1340–1342, 1993.

[106] P. K. Benicewicz and A. J. Taylor, "Scaling of terahertz radiation from large-aperture biased inp photoconductors," *Opt. Lett.*, vol. 18, pp. 1332–1334, 1993.

[107] A. J. Taylor, G. Rodriguez, and D. Some, "Ultrafast field dynamics in large-aperture photoconductors," *Opt. Lett.*, vol. 22, pp. 715–717, 1997.

[108] Y. Liu, S.-G. Park, and A. M. Weiner, "Enhancement of narrow-band terahertz radiation from photoconducting antennas by optical pulse shaping," *Opt. Lett.*, vol. 21, pp. 1762–1764, 1996.

[109] C. W. Siders, J. L. W. Siders, A. J. Taylor, S.-G. Park, M. R. Melloch, and A. M. Weiner, "Generation and characterization of terahertz pulse trains from biased, large-aperture photoconductors," *Opt. Lett.*, accepted for publication.

[110] W. Sha, J.-K. Rhee, T. B. Norris, and W. J. Schaff, "Transient carrier and field dynamics in quantum-well parallel transport: from the ballistic to the quasi-equilibrium regime," *IEEE J. Quantum Electron.*, vol. 28, pp. 2445–2455, 1992.

[111] P. K. Benicewicz, J. P. Roberts, and A. J. Taylor, "Scaling of terahertz radiation from large-aperture biased photoconductors," *J. Opt. Soc. Am. B*, vol. 11, pp. 2533–2546, 1994.

[112] G. Rodriguez and A. J. Taylor, "Screening of the bias field in terahertz generation from photoconductors," *Opt. Lett.*, vol. 21, pp. 1046–1048, 1996.

[113] S. M. Sze, *Physics of semiconductor devices, 2nd ed.* New York, NY: John Wiley & Sons, 1981.

[114] C. W. Siders, J. L. W. Siders, A. J. Taylor, S.-G. Park, and A. M. Weiner, "Efficient high-energy pulse train generation using a 2^n-pulse Michelson interferometer," *Appl. Opt.*, vol. 18, pp. 1340–1342, 1998.

[115] X. Liu, R. Wagner, A. Maksimchuk, E. Goodman, J. Workman, D. Umstadter, and A. Migus, "Nonlinear temporal diffraction and frequency shifts resulting from pulse shaping in chirped-pulse amplification system," *Opt. Lett.*, vol. 20, pp. 1163–1165, 1995.

[116] E. P. Ippen and C. V. Shank, "Techniques for measurement," in *Ultrashort light pulses*, pp. 83–122, Berlin: Springer-Verlag, 1984.

[117] A. Krotkus, S. Marcinkevicius, J. Jasinski, M. Kaminska, H. H. Tan, and C. Jagadish, "Picosecond carrier lifetime in GaAs implanted with high doses of as ions: An alternative material to low-temperature GaAs for optoelectronic applications," *Appl. Phys. Lett.*, vol. 66, pp. 3304–3306, 1995.

APPENDIX

APPENDIX

In this appendix, I present a more general formalism which calculate the temporal profile of sheet carrier concentration in the epitaxial layer and substrate in the large-aperture PC-emitter subject to saturation. Specifically, we incorporate the possibility of optical bleaching of the photoconductive thin film on SI-GaAs substrate. At the very high optical fluence excitation, the effective absorption in the thin film photoconductor is reduced because of the band filling effect. Although this was not directly observed in our case, it can be potentially important. The derived equations which relate the sheet carrier densities in the epitaxial layer and substrate to the intensity profile of optical excitation can be used in place of Eqs. 4.22 and 4.24 in Chap. 4. For the completeness of this Appendix, we repeat some portion of the formalism which was already presented in Chap. 4.

The electron concentration $n(x,t)$ in the epitaxial layer can be calculated from Eq. A.1.

$$\frac{\partial n(x,t)}{\partial t} = -\frac{(1-R)}{h\nu}\frac{\partial I_{opt}(x,t)}{\partial x} - \frac{n(x,t)}{\tau_{r,epi}} \tag{A.1}$$

,where $\tau_{r,epi}$ is the recombination/trap lifetime in the epitaxial layer, $I_{opt}(x,t)$ is the excitation pulse intensity profile, R is the reflection coefficient at the photoconductor surface, x is the distance from the semiconductor surface and $h\nu$ is the excitation photon energy. As in the Chap. 4, the sheet electron concentration in epitaxial layer is defined as

$$n_{epi}(t) \equiv \int_0^l n(x,t)\,dx \tag{A.2}$$

,where l is the thickness of the epitaxial layer. Then, Eq. A.1 can be integrated to yield,

$$\frac{\partial n_{epi}(t)}{\partial t} = \frac{(1-R)}{h\nu}\{I_{opt}(0,t) - I_{opt}(l,t)\} - \frac{n_{epi}(t)}{\tau_{r,epi}} \tag{A.3}$$

On the other hand, we model the nonlinear absorption of light in the semiconductor as

$$\frac{\partial I_{opt}(x,t)}{\partial x} = -\alpha_0(1 - \frac{n(x,t)}{n_{sat}})I_{opt}(x,t) \tag{A.4}$$

,where n_{sat} is a phenomenological constant related to the density of states in the photoconductive material. If we integrate Eq. A.4 in x, we obtain

$$I_{opt}(l,t) = I_{opt}(0,t)\exp[-\alpha_0 l(1-\frac{n_{epi}(t)}{n_{sat}l})] \qquad (A.5)$$

By substituting Eq. A.5 into Eq. A.3, we obtain the equation which relates sheet electron concentration in epitaxial layer to the temporal intensity profile of the optical excitation pulses.

$$\frac{\partial n_{epi}(t)}{\partial t} = \frac{(1-R)}{h\nu} I_{opt}(0,t)\{1-\exp[-\alpha_0 l(1-\frac{n_{epi}(t)}{n_{sat}l})]\} - \frac{n_{epi}(t)}{\tau_{r,epi}} \qquad (A.6)$$

Now, the sheet electron density in the substrate $n_{sub}(t) \equiv \int_l^\infty n(x,t)\,dx$ can be calculated easily as,

$$\frac{\partial n_{sub}(t)}{\partial t} = \frac{(1-R)}{h\nu} I_{opt}(l,t) - \frac{n_{sub}(t)}{\tau_{r,sub}} \qquad (A.7)$$

$$= \frac{(1-R)}{h\nu} I_{opt}(0,t)\exp[-\alpha_0 l(1-\frac{n_{epi}(t)}{n_{sat}l})] \qquad (A.8)$$

,where $\tau_{r,sub}$ is the recombination/trap lifetime of electrons in the substrate. In Eq. A.7, we assumed that all the light reach the substrate will be absorbed inside the substrate and generate electrons and holes.

VITA

Sang-Gyu Park was born in Seoul, Korea, in 1967. He received his B.S. and M.S. degrees in Electronics Engineering from Seoul National University. He was the recipient of the Korean Government Fellowship during 1993~1996 for his study in United States. His research interests are in ultrafast optics, terahertz radiation, and optical fiber communications. After the graduation, he will work at AT&T-Research, Red Bank, NJ.